Title

Laterality of Movement Encoding in the Cortex and Basal Ganglia

Author

Merrick, Christina

Publication Date

2021

Peer reviewed|Thesis/dissertation

Laterality of Movement Encoding in the Cortex and Basal Ganglia

by

Christina M. Merrick

A dissertation submitted in partial satisfaction of the
requirements for the degree of
Doctor of Philosophy

in

Psychology

in the

Graduate Division

of the

University of California, Berkeley

Committee in charge:

Professor Richard B. Ivry, Chair
Professor Robert T. Knight
Professor Jose M. Carmena
Assistant Professor Anne Collins

Summer 2021

Laterality of Movement Encoding in the Cortex and Basal Ganglia

Abstract

Laterality of Movement Encoding in the Cortex and Basal Ganglia

by

Christina M. Merrick

Doctor of Philosophy in Psychology

University of California, Berkeley

Professor Richard B. Ivry, Chair

1. Movements of either the contralateral or ipsilateral arm produce changes in neural activity in sensorimotor cortex as well as subcortical structures. To better understand what information is encoded by the ipsilateral arm, and if this information could be used in more applied settings (i.e., deep brain stimulation), we conducted two experiments utilizing patients who have intracranial recordings for clinical purposes. In the first study we examined patients with intracranial grids implanted in either the left or the right hemisphere. Implementing a cross-validated kinematic encoding model, we found stronger bilateral encoding in the left hemisphere, an effect that was present during preparation and was amplified during execution. Consistent with this asymmetry, we also observed better across-arm generalization in the left hemisphere. The more extensive bilateral encoding in the left hemisphere adds a new perspective to the pervasive neuropsychological finding that the left hemisphere plays a dominant role in praxis. In the second study we examined neural recordings from patients with a deep brain stimulation lead targeting the subthalamic nucleus as well as a cortical strip while they made repetitive hand movements. We fit the continuous EMG to the neural activity using a cross-validated encoding model and found that electrodes in the subthalamic region encode both hands equally well whereas in the sensorimotor cortex we found a strong contralateral bias. In addition, we found that electrodes in the subthalamic region generalize across arms better than the sensorimotor cortex and appear to be more sensitive to context (i.e., whether the other arm is engaged in the task or not). 2. Non-invasive brain stimulation (NIBS) can safely manipulate neural excitability in the human brain, providing neuroscientists with a powerful tool to advance our understanding of brain function and clinicians with novel interventions in the treatment of neurological and psychiatric disorders. We have developed a new NIBS system, kilohertz transcranial magnetic perturbation (kTMP), which can produce subthreshold modulations of neural activity with a cortical E-field of up to 7.6 V/m at 5 kHz. In two experiments we show that kTMP can modulate cortical excitability both with non-modulated waveforms at kilohertz frequencies and with amplitude modulated frequencies which are physiologically relevant for endogenous frequencies.

Acknowledgments

I would like to thank the amazing people I met at Berkeley over my six years, those who lightened my load and made me smile as I made my way through this PhD. I would particularly like to thank all the people in the Ivry lab especially Assaf Breska for the late-night lab chats, Ludovica Labruna for always being an understanding and a great collaborator and Darius Parvin for being a terrific office mate, friend and for making me laugh by experimenting on the squirrels who used to frequent the (old) Tolman roof. I would also like to thank Anwar Nunez-Elizalde for helping me think through several research problems, my research benefited from your expertise and I benefited from your friendship. Sometimes you get lucky and meet people in lab or the PhD program who also become your closest friends. Manon Ironside and Maedbh King you served as my sounding board in good times and bad and your constant and fierce friendship made my time at Berkeley so much more memorable, fun and meaningful. I might have been able to do this without you, but I sure wouldn't have wanted to. I also want to thank Robert Knight who often felt like my second advisor, your faith in my abilities and your advocacy of my work gave me confidence and I will be forever grateful. Last, I want to thank my advisor Rich Ivry who took a gamble on a 27-year-old who couldn't code – hardly the traditional PhD recruit. He bet on me and in doing so gave me an incredible opportunity to learn and study with some of the most amazing people I've ever met. My weekly meetings with Rich have been a constant over the years and I will honestly miss them once I am gone- I feel like whatever problem you may have, one hour sitting with Rich in his office and it will seem less like a problem. I will always be grateful to Rich for allowing me to have the PhD that I wanted, to take time to learn more complicated methods, to focus on the science and less on the outcomes and for giving me autonomy over my research projects. Thank you for being patient with me and for being with me on this journey.

Chapter 1

Left Hemisphere Dominance for Bilateral Kinematic Encoding in the Human Brain

1.1 Abstract

Neurophysiological studies in humans and non-human primates have revealed movement representations in both the contralateral and ipsilateral hemisphere. Inspired by clinical observations, we ask if this bilateral representation differs for the left and right hemispheres. Electrocorticography (ECoG) was recorded in human participants during an instructed-delay reaching task, with movements produced with either the contralateral or ipsilateral arm. Using a cross-validated kinematic encoding model, we found stronger bilateral encoding in the left hemisphere, an effect that was present during preparation and was amplified during execution. Consistent with this asymmetry, we also observed better across-arm generalization in the left hemisphere, indicating similar neural representations for right and left arm movements. Notably, these left hemisphere electrodes were largely located over premotor and parietal regions. The more extensive bilateral encoding in the left hemisphere adds a new perspective to the pervasive neuropsychological finding that the left hemisphere plays a dominant role in praxis.

1.2 Introduction

A primary tenet of neurology is the contralateral organization of movement. The vast majority of the fibers from the corticospinal tract cross to the opposite side of the body (Nyberg-Hansen & Rinvik, 1963) and functionally, hemiparesis resulting from cortical stroke is manifest on the contralateral side of the body (Bourbonnais, & Noven, 1989). Although direct control of arm movements is primarily mediated through contralateral projections, unimanual arm movements elicit bilateral activity in the primary motor cortex (M1, Babiloni et al., 1999; Ghacibeh et al., 2007), indicating that neural activity in the ipsilateral hemisphere contains information relevant to ongoing movement. Correspondingly, kinematic and movement parameters of the ipsilateral limb can be decoded from ipsilateral hemisphere intracortical recordings in monkeys (Ganguly et al., 2009; Ames & Churchland, 2019) and from electrocorticography (ECoG) in humans (Bundy, Szrama, Pahwa & Leuthardt, 2018; Ganguly et al., 2009, Wisneski et al., 2008). Ipsilateral signals represent an intriguing source of neural activity, both for understanding how activity across the two hemispheres results in coordinated movement and because this information might be exploited for rehabilitative purposes.

While it is established that information about unimanual movements is contained within the ipsilateral hemisphere, there remains considerable debate about what this signal represents. Previous studies have centered on the question of whether ipsilateral representations overlap or are independent of contralateral representations, leading to mixed results. Consistent with the

overlap hypothesis, neural activity for the contralateral and ipsilateral limb movements show several similarities, including shared target tuning preferences and the ability to cross predict kinematic features from a model trained on the opposite arm (Bundy, Szrama, Pahwa & Leuthardt, 2018; Cisek, Crammond & Kalaska, 2003; Steinberg et al., 2002, Willett et al., 2020). Consistent with the independence hypothesis, intracortical recordings in monkeys have revealed that the lower dimensional representations of the two arms lie in orthogonal subspaces (Ames, Churchland, 2019; Heming, Cross, Takei, Cook & Scott, 2019). These hypotheses are not mutually exclusive: For example, the degree of overlap or independence may depend on the gesture type (e.g., overlapping representations for grasping but not arm movement, Downey et a., 2020), or brain region (e.g., premotor cortex displays stronger preservation of tuning preferences across the two arms than primary motor cortex, Cisek, Crammond & Kalaska, 2003).

One factor that has received little attention in this literature is the recording hemisphere. This is surprising given the marked asymmetries between the two hemispheres in terms of praxis (Corballis, Badzakova-Trajkov & Häberling, 2012; Rothi, Ochipa & Heilman, 1997). Tracing back to the early 20th century, marked hemispheric asymmetries have been defined by the behavioral deficits observed following unilateral brain injury (Schaefer, Haaland & Sainburg, 2007; Liepmann 1908, cited in Renzi, & Lucchelli, 1988). Apraxia, an impairment in the production of coordinated, meaningful movement in the absence of muscle recruitment deficits, is much more common after left compared to right hemisphere insult (Haaland, Harrington & Knight, 2000; Renzi, & Lucchelli, 1988). Moreover, left hemisphere stroke will frequently result in apraxic symptoms for gestures produced with either hand, as well as impairments in action comprehension (Renzi, & Lucchelli, 1988). Hemispheric asymmetries are also evident in neuroimaging activation patterns in healthy participants, with the left hemisphere having stronger activation during ipsilateral movement than the right hemisphere, especially with increasing task difficulty (Chettouf et al., 2020, Verstynen et al. 2005; Verstynen and Ivry 2011; Schäfer et al, 2007). These patterns raise the possibility that the ipsilateral cortical representation differs between the left and right hemispheres.

In the present study, we use intracranial recordings from the cortical surface (ECoG) to examine the degree of cortical overlap for ipsilateral and contralateral upper limb movement in the left and the right hemisphere. The data were collected from six patients, three with left hemisphere implants and three with right hemisphere implants, while they engaged in an instructed-delay reaching task. We focus on predicting the temporal dynamics of high frequency activity (HFA; 70-200Hz), a surrogate for infragranular single-unit activity and supragranular dendritic potentials, (Leszczynski et al., 2020) which tracks local activation of the cortex (Muthukumaraswamy, 2010). Going beyond previous studies that use decoding models which combine multiple neural features from multiple electrodes to predict kinematics, we employed an encoding model which uses kinematic features to predict neural activity for each electrode, allowing us to retain the high spatial and temporal resolution of the ECoG signal. This approach allows us to create high-resolution topographic maps depicting encoding strength on the surface of the cortex for movements produced with the contralateral and ipsilateral arm. This is preferable to projecting the weights obtained from decoding models since these models have difficulty disambiguating between informative and uninformative electrodes (Kriegeskorte & Douglas, 2019). Moreover, our approach provides a way to map kinematics to neural activity in a time-resolved manner (rather

than as single weights), allowing us to identify time ranges of representational overlap and divergence across the two arms for each electrode.

1.3 Method

Participants. Intracranial recordings were obtained from six patients (2 female; 5 right-handed) implanted with subdural grids as part of their treatment for intractable epilepsy. Data were recorded at three hospitals: University of California, Irvine (UCI) Medical Center (n = 2), University of California, San Francisco (UCSF) Medical Center (n = 2) and California Pacific Medical Center (CPMC), San Francisco (n = 2). Electrode placement was solely determined based on clinical considerations and all procedures were approved by the institutional review boards at the hospitals, as well as the University of California, Berkeley. All patients provided informed consent prior to participating in the study.

Behavioral task. Patients performed an instructed-delay reaching task while sitting upright in their hospital bed. The patient rested their arms on a horizontal platform (71 cm x 20 cm) that was placed over a standard hospital overbed table. The platform contained two custom-made buttons, each connected to a microswitch. At the far end of the platform (13 cm from the buttons, approximately 55 cm from the patient's eyes), a touchscreen monitor was attached, oriented vertically. Visual targets could appear at one of six locations, four for each arm (Figure 1.1a). The two central locations were used as targets for reaches with either arm; the two eccentric targets varied depending on the arm used. Stimulus presentation was controlled with Matlab 2016a. A photodiode sensor was placed on the monitor to precisely track target presentation times. The analog signals from the photodiode and the two microswitches were fed into the ECoG recording system and were digitized into the same data file as the ECoG data with identical sampling frequency.

Testing of the contralateral and ipsilateral arms (relative to the ECoG electrodes) was conducted in separate experimental blocks that were counterbalanced. To start each trial, the patient placed their left and right index fingers on two custom buttons to depress the microswitches (this indicated they were in the correct position and ready to start the trial). If both microswitches remained depressed for 500 ms, a fixation stimulus was presented in the middle of the screen for 750 ms, followed by the target, a circle (1.25 cm diameter) which appeared in one of the four locations. Another hold period of 900 ms followed in which the participant was instructed to prepare the required movement while the target remained on the screen. If the microswitch was actuated during this hold period, an error message appeared on the screen and the program would advance to the next trial. If the start position was maintained, a compound imperative stimulus was presented at the end of the hold period. This consisted of an auditory tone and an increase in the size of the target (2.5 cm diameter). The participant was instructed that this was the signal to initiate and complete a continuous out-and-back movement, attempting to touch the screen at the target location before returning back to the platform. The target disappeared when the touchscreen was contacted. The imperative was withheld on 5% of the trials ('catch' trials) to ensure that the participant only responded after the onset of the imperative.

Once back at the home position, the screen displayed the word 'HIT' or 'MISS' for 750 ms to indicate if the touch had occurred within the target zone. The target zone included the 2.5 diameter circle as well as a 1cm buffer around the target. After the feedback interval, the screen was blank for 250 ms before the reappearance of the fixation stimulus, signaling the start of the next trial. The patients were informed to release either of the buttons at any time they wished to take a break.

Each block consisted of 40 trials (10/target), all performed with a single limb. Blocks alternated between contra- and ipsilateral arms (relative to the ECoG electrodes), with the order counterbalanced across patients. Each block took approximately 5-6 minutes to complete. All patients completed at least two blocks with each per arm (Table 1).

Movement analysis and trajectory reconstruction. We used two methods to analyze the movements. For the first method, we recorded key events defined by the release of the microswitch at the start position, time and location of contact with the touchscreen, and return time to the home position, defined by the time at which they depressed the home position microswitch. For the second method, we used the Leap Motion 3-d movement analysis system (Weichert, et al., 2013) to record continuous hand position and the full movement trajectory (sampling rate = 60 Hz). Although the Leap system is a lightweight video-based tracking device that is highly mobile, the unpredictable environment of the ICU led to erratic recordings from the Leap system. For example, patients frequently had intravenous lines in one or both hands which obstructed the visibility of the hand and interfered with the ability of the Leap system to track the hand using their built-in hand model. This resulted in lost samples and therefore satisfactory kinematic data was obtained from only a subset of conditions collected from patients using the Leap system.

Given the limitations with the Leap data, we opted to use a simple algorithm to reconstruct the time-resolved hand trajectory in each trial, estimating it from the event-based data obtained with the first method. We used a beta distribution to estimate the velocity profile of the forward and return reach based on reach times and the travel distance (sampling rate = 100 Hz). We opted to use a beta distribution because this best matched the velocity profiles of the data obtained with the Leap system.

For conditions that had clean kinematic traces (no lost samples) from the Leap system, we compared the estimated kinematic profiles with those obtained with the Leap system. There was a high correlation between the two data sets ($r = .98$ for position in the Z dimension; $r = .93$ for velocity in the Z dimension). We note that our method of estimating the trajectories results in a smoothed version of the movement, one lacking any secondary or corrective movements that are sometimes observed when reaching to a visual target (Suway & Schwartz, 2019). We believe this is still a reasonable estimation given the high correlation with the continuous Leap data, and the fact that participants had ample time to prepare the movements and were instructed and observed to make ballistic movements by the experimenter who was present for all recording sessions (CMM).

Electrode Localization. Grid and strip electrode spacing was 1 cm in four patients and 4 mm in the two other patients. The electrode locations were visualized on a three-dimensional reconstruction of the patient's cortical surface using a custom script that takes the post-operative computer tomography (CT) scan and co-registers it to the pre-operative structural magnetic resonance (MR) scan (Stolk et al., 2018).

Neural data acquisition and preprocessing. Intracranial EEG data and peripheral data (photodiode and microswitch traces) were acquired using a Nihon Kohden recording system at UCI (128 channel, 5000 Hz digitization) and CPMC (128 channel, 1000 Hz digitization rate), and two Tucker Davis Technologies recording systems at UCSF (128 channel, 3052 Hz digitization rate).

Offline preprocessing included the following steps. First, if the patient's data was not sampled at 1000 Hz (UCI and UCSF recording sites), the signal from each electrode was low-pass filtered at 500 Hz using a Butterworth filter as an anti-aliasing measure before down-sampling to 1000 Hz. Electrodes were referenced using a common average reference. Each electrode was notch-filtered at 60, 120 and 180 Hz to remove line noise. The signals were then visually inspected and electrodes with sustained excessive noise were excluded from further analyses. The signals were also inspected by a neurologist (RTK) for epileptic activity and other artifacts. Electrodes that had pathological seizure activity were also excluded from the main analyses. Out of 752 electrodes, 82 were removed due to excessive noise and 5 were removed due to epileptic activity, resulting in a final data set of 665 electrodes. Catch trials and unsuccessful reaches were not included in the analyses.

From the cleaned data set, we extracted the HFA instantaneous amplitude using a Hilbert transform. To account for the 1/f power drop in the spectrum, we divided the broadband signal into five narrower bands that logarithmically increased from 70 to 200 Hz (i.e., 70-86, 86-107, 107-131, 131-162, 162-200 Hz), and applied a band-pass filter within each of these ranges. We then took the absolute value of the Hilbert transform within each band-pass, performed a z-score transformation, and averaged the five values. Z-scoring was performed after concatenating all the blocks for each patient, ensuring that we did not obscure possible amplitude differences across the two arms. As a final step, the data were down-sampled to 100 Hz to reduce computational load (e.g., number of parameters in the encoding model, see below). HFA amplitude fluctuations (envelope; are evident at lower frequencies (Canolty et al., 2006; Pei et al., 2011).

Feature selection. Four estimated kinematic features were used to predict HFA (Figure 1B left). The first two features were position and speed in the Z dimension. This dimension captures variability related to movement that is relatively independent of target location (i.e., along the axis between the patient and touchscreen). The second pair of features were spherical angles that define the specific target locations (Figure 1A right). Features were selected to reduce collinearity and redundancy in the encoding model. Because we include time lags for each kinematic feature, derivatives can emerge from the linear model (e.g., velocity and acceleration

can be created from position); thus, velocity and acceleration were not included as additional features. Speed is a non-linear transformation of position and is added as a separate feature.

Kinematic encoding model. The estimated kinematic features were used to predict the HFA for each electrode (Fig 1.1F). We created a 4 x 400 feature matrix by generating a time series for each feature by time-lagging the values of the selected feature relative to the neural data, with lags extending from 2 s before movement onset to 2 s after movement onset (sampling rate at 100 Hz). This wide range of lags serves two purposes. First, it provides a way to compensate for the anticipated asynchrony between neural data and movement kinematics. Second, it allowed us to evaluate HFA activity during the instructed delay (beginning ~1.5 s before movement onset) period as well as during movement. HFA at each time point [HFA(t)] was modeled as a weighted linear combination of the kinematic features at different time-lags, resulting in a set of beta weights, b1 …, b400 per kinematic feature. To make the beta weights scale-free, the kinematic features and neural HFA were z-scored before being fit by the model.

Model fitting. Regularized (ridge) regression (Hoerl and Kennard, 1970) was used to estimate the weights that map each kinematic feature (X) to the HFA signal (y) for each electrode, with being the regularization hyperparameter:

$$\hat{\beta} = \left(X^T X + \lambda I\right)^{-1} X^T Y$$

For within-arm model fitting, the total dataset consisted of all clean, successful trials performed with either the ipsilateral or contralateral arm (each arm was fit separately). Nested five-fold cross-validation was used to select the regularization hyperparameter on inner test sets (validation sets) and assess prediction performance on separate, outer test sets. At the outer level, the data was partitioned into five mutually exclusive estimation and test sets. For each test set, the remaining data served as the estimation set. For each outer fold, we further partitioned our estimation set into five mutually exclusive inner folds to train the model (80% of estimation set) and predict neural responses across a range of regularization values on the validation set (20% of estimation set). For each inner fold, the regularization parameter value was selected that produced the best prediction as measured by the linear correlation of the predicted and actual HFA. The average of the selected regularization parameters across the five inner folds was computed and used to calculate the prediction of the HFA on the outer test set. This procedure was done at the outer level five times. Our primary measure is held-out prediction performance (R^2), which we quantified as the squared linear correlation between the model prediction and the actual HFA time series, averaged across the five mutually exclusive test sets.

To be considered as predictive, we established a criterion that an electrode must account for at least 5% of the variability in the HFA signal ($R^2 > .05$) for either ipsilateral or contralateral reaches (Downey et a., 2020). Electrodes not meeting this criterion were not included in subsequent analyses.

For across-arm model fitting, the same procedure was used except the test set was partitioned from the total dataset of the other arm. We partitioned the data in this manner (80% estimation,

20% test) to make the fitting procedure for the across-arm model comparable to that employed in the within-arm model.

Tuning modulation and similarity across arms. Modulation depth of target tuning was calculated as the standard deviation of the mean HFA predictions for each of the four target locations:

$$\mathrm{MD} = \sum_{i=1}^{n} \frac{(x_i - \bar{x}_i)^2}{n}$$

To assess similarity in tuning across the two arms, we computed, for each electrode, the SSE (sum of squared errors) for average HFA predictions to the same target between the contralateral and ipsilateral arms.

$$\mathrm{SSE_e} = \sum_{i=1}^{n} (\{\mathrm{contra_i} - \mathrm{ipsi_i})\}^2$$

This metric was only calculated for the two central targets, the targets common to both arms (the two eccentric target locations varied depending on the arm used). These values were scaled from 0 to 1 based on the minimum and maximum values of SSE across all electrodes. SSE represents a metric of dissimilarity; To calculate a similarity index (SI), we converted this to a measure of similarity by subtracting the scaled SSE values from 1:

$$SI = 1 - \frac{\mathrm{SSE_e} - \min(\mathrm{SSE_e})}{\max(\mathrm{SSE_e}) - (\mathrm{SSE_e})}$$

Thus, higher SI represents more similar average predictions.

Separating instruction and movement phases. The encoding model was run to predict the full HFA time course. To compare model prediction performance during different phases of the task, the data were epoched into instruction and movement phases, using event markers recorded in the analog channel (i.e., cue onset and movement onset). Epochs of the same task phase were concatenated together, and prediction performance was operationalized as the square of the Pearson correlation between the predicted and actual HFA for each task phase.

Permutation testing. A permutation-based analysis-of-variance (pbANOVA) was used to assess differences in distributions for the different experimental conditions. pbANOVA is preferable for experimental designs that involve orthogonal manipulation of fixed factors in which the measured variable does not conform to the distributional assumptions necessary for traditional parametric ANOVA (Anderson & Braak, 2003). In this analysis, null distributions for the main effect of each factor and interaction are created using 10000 surrogate datasets, in each of which the data of a random subset of participants is permuted. In each iteration, the surrogate data is analyzed using a standard ANOVA and the F value of the relevant effect is registered. The effect in the original data is considered significant only if the F value of a standard ANOVA of this effect is larger than 95% of the values in the null distribution. For main effects, the permutations are conducted such that the raw values of the factor of interest are permuted within the levels of the other factor ('restricted' permuting). For the interaction effect, the permutations are not

conducted on the raw data but on a dataset that is generated by subtracting the contribution of the main effects from the raw data (see, Anderson & Braak, 2003). The resulting dataset ('reduced' dataset) includes only the interaction terms and their random errors. On this reduced dataset the permutations are conducted without being limited to levels of specific factors ('unrestricted' permutations).

Calculating distance from dorsal central sulcus. For each patient, 30 discrete (x, y) coordinates were manually demarcated along the central sulcus on individual MRI scans. The 30 points were then interpolated to create a line traversing the central sulcus for each individual. The dorsal aspect of the central sulcus was defined as all points dorsal to the midpoint of the central sulcus. We then calculated the absolute distance between each electrode and the closest point on the dorsal aspect of the central sulcus (our interpolated line).

1.4 Results

Behavior. Patients made continuous reaches to and from the touchscreen, producing roughly, bell-shaped velocity profiles for both the outbound and the inbound segments of our estimated kinematics (Fig 1.1C,1.1E). Table 1 summarizes the total number of successful trials, along with the reaction time and movement time data. A trial was considered unsuccessful if the reach was initiated before the go cue or if contact with the touchscreen was outside the boundary of the target. The percentage of unsuccessful trials was low, ranging between 0% to 12.5% across individuals. Outbound reaches (platform to touchscreen) were, on average, faster than inbound reaches (touchscreen to platform) for the majority of patients. Note that the reaction time data are averaged across left and right arm reaches since there was no consistent difference on this measure.

At a more fine-grained level of spatial accuracy, we calculated the distance from the center of each target to the touch location for each trial. On average, the mean distance from the center of the 2.5 cm circle was 0.80 cm (SD = 0.10 cm) for right-handed reaches and 0.90 cm (SD = 0.17 cm) for left-handed reaches (Fig 1.1D). These values did not differ from one another ($t = 1.538$, $p = .222$).

Stronger bilateral encoding in the left hemisphere. We examined the extent to which movement kinematics were encoded for contralateral and ipsilateral reaches in individual electrodes. To do this we fit a kinematic encoding model that maps continuous kinematic features to the HFA signal (Fig 1.1F) for the 665 electrodes meeting our inclusion criteria. This procedure was done separately for contralateral and ipsilateral reaches. We quantified the cross-validated model fit by generating HFA predictions using the kinematic features from held-out trials of the same condition and calculating prediction performance as the square of the linear correlation (R^2) between the predicted and actual HFA signal (Fig 1.2B).

Patient ID	Handedness	RT	Outbound reach	Inbound reach	Total trials
L1	Right	392 (102)	703 (118)	907 (287)	152
L2	Right	1574 (871)	598 (173)	1003 (406)	146
L3	Ambidextrous	771 (345)	946 (183)	1429 (252)	148
R1	Right	518 (194)	940 (211)	1027 (345)	132
R2	Right	335 (55)	602 (94)	590 (120)	145
R3	Right	534 (157)	721 (145)	1017 (318)	145

Table 1.1. Summary of performance measures for each participant.

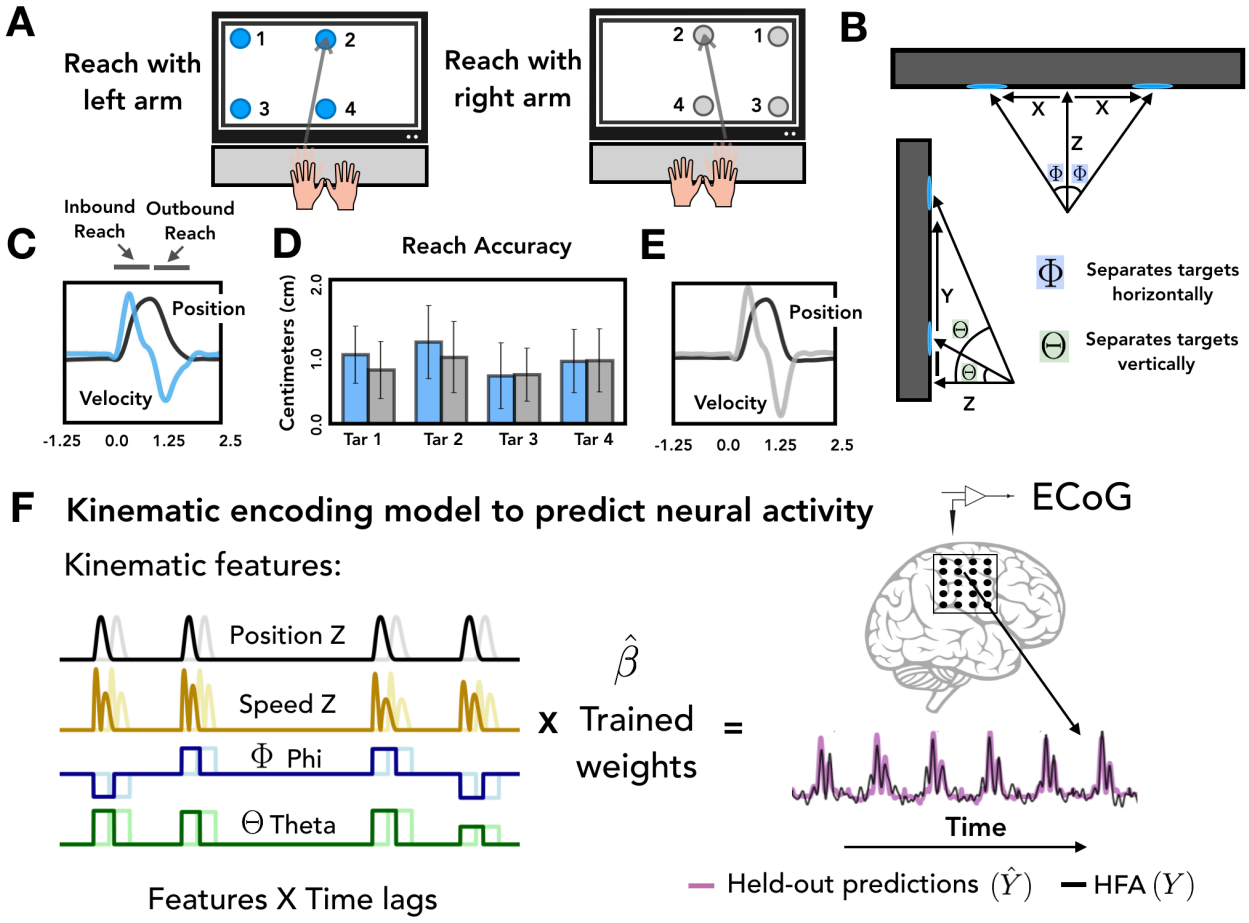

Figure 1.1. Task and model design. A) Task design. Patients performed an instructed-delay reaching task, moving to targets that appeared on a touchscreen monitor with either the left or right arm. B) Task Schematic. Target position with respect to the start position of the reaching

arm can be defined on the basis of three Cartesian coordinates (X, Y, Z) and two spherical angles (Theta and Phi). **C) Reaching profile, left.** Average estimated position and velocity traces for a representative series of trials performed with the left arm. **D) Reach accuracy.** Accuracy was quantified as the absolute distance from the center of each target (target diameter = 2.5cm) to the touch location for all four targets with the left (blue) and right (grey) arm. **E) Reaching profile, right.** Same as C, but with the right arm. **F) Kinematic encoding model**. Time lagged estimated kinematic features were used to the predict high frequency activity (HFA) for each electrode using ridge regression. Four kinematic features were included in the model: Position in the Z dimension, speed in the Z dimension and the two spherical angles Phi and Theta. Kinematic features were trained on a subset of the HFA data and predictions of HFA activity were evaluated with held-out test sets.

Figure 1.2A displays R^2 values for each electrode for the contralateral and ipsilateral condition, presented on the individual patient MRIs. Electrodes with high prediction performance were primarily located in arm areas of sensorimotor cortex. In line with previous research (Downey et a., 2020), a sizeable percentage of the electrodes were able to predict the HFA at or above our criterion of $R^2 > .05$ (examples shown in Figure 2B). This degree of prediction was observed not only when the data were restricted to contralateral movement (31% of electrodes), but also when the data were from ipsilateral movement (25%). A number of electrodes (24%) were predictive in both the contralateral and ipsilateral models. Electrodes that did not meet this criterion for either arm are represented as small dots in figure 1.2A and were excluded from further analysis, leaving a total of 216 predictive electrodes (32%, 141 = left hemisphere, 75 = right hemisphere).

We next asked whether prediction was stronger for contralateral movement, and whether this varied between the two hemispheres. Figure 1.2C compares the predictive performance for each electrode for the contralateral and ipsilateral conditions. Values close to the unity line yield similar predictions for the conditions; values off the unity line indicate that encoding is stronger for one arm compared to the other. To compare prediction performance at the group level, distributions were created by taking the difference between the R^2 values for the contralateral and ipsilateral conditions for each electrode (Figure 1.2C, upper right corner of each scatterplot). As can be seen, there is a pronounced contralateral bias for both hemispheres (one sample t-test against zero: $_{left} = 0.024$, $p_{left} < .001$, $_{right} = 0.115$, $p_{right} < .001$). Importantly, the contralateral bias was attenuated in the left hemisphere compared to the right hemisphere (permutation test, $p < .001$), indicating stronger bilateral encoding in the left hemisphere. In addition to the hemisphere effect, we also found that the contralateral bias becomes weaker the further the electrodes are from putative primary motor cortex in both hemispheres ($r_{left} = -0.48$, $p_{left} < .001$, $r_{right} = -0.45$, $p_{right} < .001$).

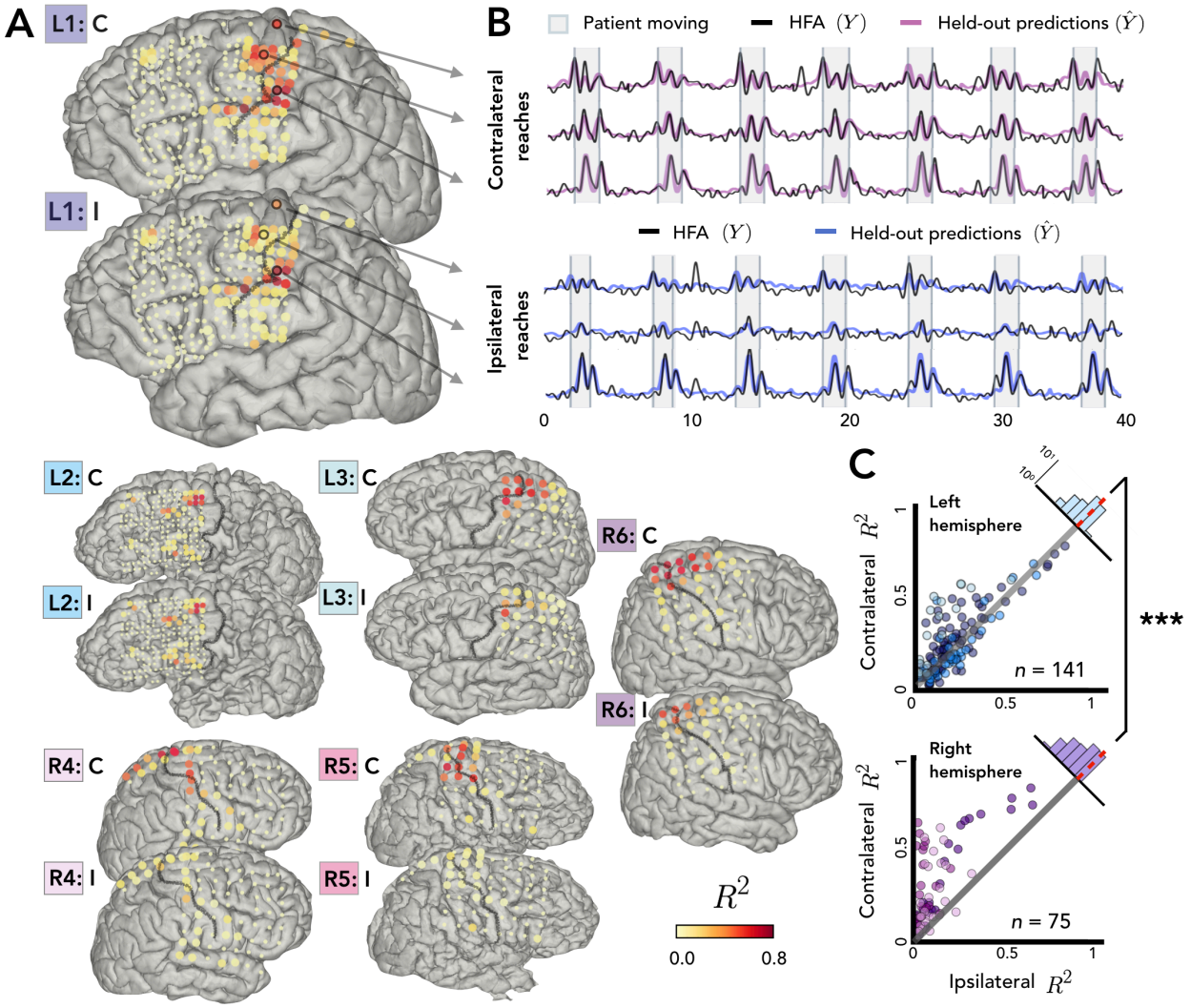

Figure 1.2. Stronger bilateral encoding in left hemisphere. Held-out prediction performance (R^2) was computed for each electrode during contralateral reaches (C) and ipsilateral reaches (I). R^2 was calculated as the squared linear correlation between the actual HFA and the predictions based on the model. **A) Prediction performance maps for individual patients.** Performance of each electrode, shown at the idiosyncratic electrode location for each participant (location based on clinical criteria). Electrodes that did not account for at least .05% of the variance (R^2 <.05) in either the contralateral or ipsilateral condition are shown as smaller dots. **B) Model predictions.** Representative time series of the actual HFA and model-based predictions for three electrodes during contralateral and ipsilateral reaches. **C) Summary across patients.** Scatter plot displaying R^2 values separately for patients with electrodes in either the left (upper) or right (lower) hemisphere. R^2 for contralateral predictions are plotted against R^2 for ipsilateral predictions. Electrodes close to the unity line encode both arms equally whereas electrodes off the unity line indicate stronger encoding of one arm. Points above the unity line indicate stronger encoding of the contralateral arm. These differences are summarized in the frequency histograms in the upper right of each panel. The histogram shows less of a shift in the left hemisphere, a signature consistent with stronger bilateral encoding. *p<0.05, **p<0.01, ***p<0.001, permutation test.

Opposing patterns of kinematic encoding for the left and right hemisphere during planning and execution. As neural activity unfolds from preparation to movement, the underlying computations may change substantially (Elsayed et al., 2016).

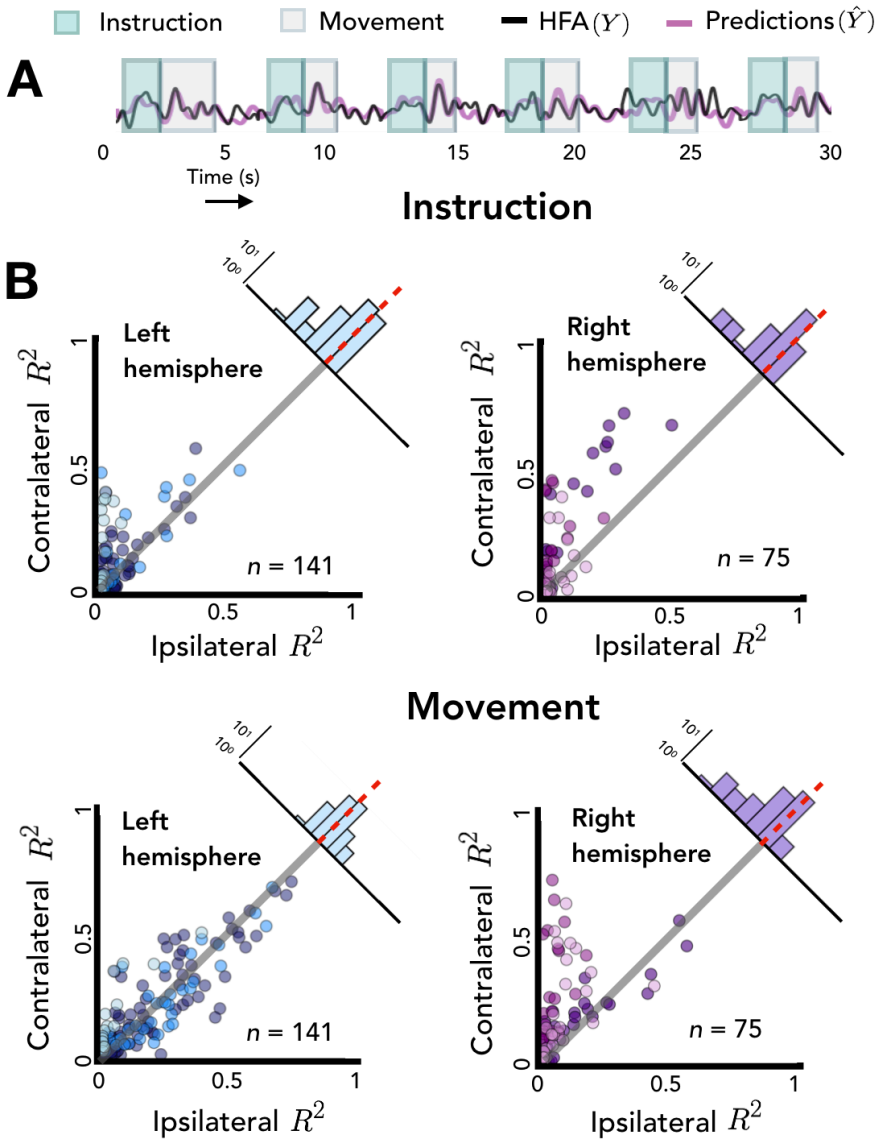

Figure 1.3. Opposing encoding patterns for left and right hemisphere across task phase. For all predictive electrodes the time series was segmented into instruction and movement epochs. R^2 was then calculated separately for each epoch. **A) Example model predictions.** Time series of a representative electrode with boxes surrounding the instruction (teal) and movement epochs (grey). **B) Prediction performance during movement and instruction.** Comparison of R^2 values for contralateral and ipsilateral predictions during the instruction epoch (top) and the movement epoch (bottom) for patients with electrodes in the left hemisphere (left) or right (right) hemisphere. Bilateral encoding was stronger in the left hemisphere, an effect that was especially pronounced during the movement phase.

To examine if hemispheric asymmetries in encoding depend on task state, we repeated the analysis described in the previous section, but now separated the data to test the held-out predictions during the instruction and movement phases (Fig 1.3A). We used a mixed design permutation test to examine the effect of hemisphere and task phase on our measure of contralateral bias (Fig 1.3B).

As in the previous analysis, the effect of hemisphere was significant, with stronger bilateral encoding (i.e., smaller difference score) in the left hemisphere compared to the right hemisphere ($p < .001$). The effect of task phase was not significant, but there was a significant interaction between hemisphere and task phase ($p < .005$): There was a larger difference between the two hemispheres during the movement phase compared to the instruction phase. Analyzing simple effects within each hemisphere, we found that encoding in the left hemisphere was more bilateral during movement compared to instruction ($\Delta R^2_{left\_move} = 0.006$, $\Delta R^2_{left\_instruction} = 0.042$, $p < .001$). In contrast, the opposite pattern was observed in the right hemisphere, with encoding being more bilateral during the instruction phase ($\Delta R^2_{right\_move} = 0.127$, $\Delta R^2_{right\_instruction} = 0.103$, $p < .001$). The contralateral bias was most attenuated in the left hemisphere during the movement condition, with a mean difference score that was not statistically different from zero ($p_{left\_move} = .482$). For the left hemisphere instruction phase and both phases for the right hemisphere, the contralateral bias was significant ($p_{left\_instruction} < .001$, $p_{right\_move} < .001$, $p_{right\_instruction} < .001$.

These results suggest that the left and right hemisphere may have different roles in bilateral encoding with regard to task phase. In particular, the contralateral bias disappears in the left hemisphere during movement indicating that prediction.

Across arm generalization: More overlap between arms in the left hemisphere. The preceding analyses focused on an encoding analysis for within-arm prediction. We next evaluate the overlap between the neural representations for contralateral and ipsilateral movement. To this end, we examined across-arm prediction performance by training the kinematic encoding model with the data from movements produced with one arm and testing prediction performance using the data from movements produced with the other arm.

Figure 1.4A shows the traces for two representative electrodes, one that shows good generalization across the two arms and the other that shows poor generalization. For the electrode that shows good generalization (E1), prediction performance for held-out contralateral reaches is comparable when the model is trained on data from either the contralateral or ipsilateral arm. This suggests that there is overlap between the neural representations for reaches performed with either upper limb for this electrode. In contrast, the electrode showing poor generalization (E2) showed good prediction for contralateral reaches when trained with contralateral data, but poor prediction when trained with ipsilateral data. Here the neural representations for the arms do not overlap. Note that E2 showed relatively strong within-arm ipsilateral encoding ($R^2 = .25$); thus, the inability of this electrode to generalize across arms is not a result of poor encoding of the ipsilateral arm. Rather, E2 encodes movement produced by either arm, but the manner in which they are encoded differs.

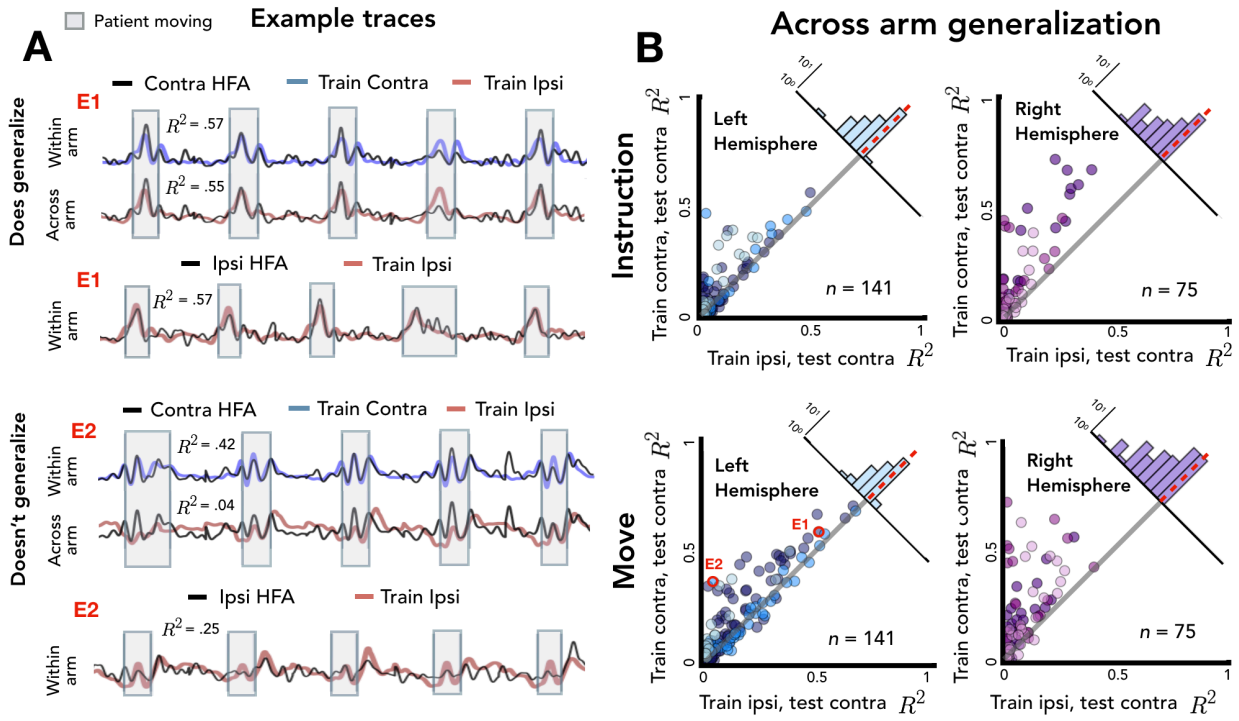

Figure 1.4. Stronger across-arm generalization in the left hemisphere. Across-arm predictions were created by training the model on ipsilateral reaches and using the trained weights to predict HFA during contralateral reaches. (Within-arm predictions generated the same as in Figs 1.2 and 1.3.) Electrodes close to the unity line have overlapping neural representations across the two arms whereas electrodes off the unity line indicate that the two arms are being encoding differentially. **A) Model Predictions.** Predicted and actual HFA for two electrodes selected from the distribution of left-hemisphere electrodes during movement, one that generalizes well across arms (E1) and one that fails to generalize (E2). Bottom row shows within-arm performance for ipsilateral trials, demonstrating that the failure to generalize across arms does not necessarily indicate poor ipsilateral performance. **B) Across-arm generalization across patients.** R^2 for within-arm predictions plotted against R^2 for across-arm predictions, with the analysis performed separately for the instruction and movement phases. Left hemisphere electrodes showed better generalization than right hemisphere electrodes, an effect that was magnified in the movement phase.

Figure 1.4B summarizes the comparison of within-arm prediction (y axis) against across-arm prediction (x axis), with the data separated for the instruction and movement phases. In this depiction, electrodes close to the unity line have overlapping neural representations during contra- and ipsilateral movement, whereas electrodes off the unity line encode the two arms differentially. We again used a mixed design permutation test, now applied to the difference between within-arm R^2 and across-arm R^2 for each electrode (Figure 1.4B, upper right corner of each scatterplot). Overall, the left hemisphere showed stronger between-arm generalization than the right hemisphere (main effect of hemisphere: $\Delta R^2_{left} = 0.041$, $\Delta R^2_{right} = 0.108$; $p < .001$). This indicates that the left hemisphere not only has stronger bilateral encoding (Figure 3B) but

also has more similar neural representations across the two upper limbs. We also found a main effect of task phase, with better across-arm generalization occurring during instruction compared to movement (main effect of task phase: $\Delta R^2_{instruction} = 0.050$, $\Delta R^2_{movement} = 0.079$; $p < .001$).

In addition to these main effects, there was also a significant interaction between task phase and hemisphere ($p < .05$). Analyzing simple effects within each task phase, the left hemisphere had better across-arm generalization for both the instruction and movement phase (simple effect analysis: $p_{instruct} < .001$, $p_{move} < .001$). In addition, better across-arm generalization was found during the instruction phase in both the left and the right hemispheres (simple effect analysis: $p_{left} < .001$, $p_{right} < .001$). The significant interaction indicates that while the neural representations across arms became more distinct in both hemispheres with the transition from instruction to movement, this difference was more pronounced in the right hemisphere. In sum, electrodes in the left hemisphere generalize across-arms better during instruction and movement compared to the right hemisphere and electrodes in the left hemisphere also change less during the transition from instruction to movement compared to the right hemisphere.

As can be seen in Figure 1.5B, electrodes that generalize well were predominantly found in the left hemisphere (white circles). In contrast, electrodes showing poor generalization are observed in both hemispheres (magenta circles). Moreover, in both hemispheres, electrodes showing poor generalization were clustered near the dorsal portion of the central sulcus, a region corresponding to the arm area of motor cortex. Electrodes showing strong generalization (mostly limited to the left hemisphere) tended to be in dorsal and ventral premotor cortices, along with a few in dorsal parietal lobe. This pattern was also observed when we analyzed all electrodes, rather than restrict the analysis to those showing extreme values. Here we used continuous measures, correlating the amount of across-arm generalization with the distance (absolute value) from the dorsal aspect of the central sulcus. The correlation was significant in the left hemisphere ($r_{left} = 0.463$, $p_{left} < .001$) but did not reach significance in the right hemisphere, although the trend was in the same direction ($r_{right} = 0.224$, $p_{right} = .068$).

To examine the dynamics of representational overlap and divergence, we averaged the time-resolved HFA amplitude across electrodes, restricted to those included in the categorical analysis. Figure 1.5C displays the average time series for contralateral (solid line) and ipsilateral (dashed line) predictions for electrodes that generalize well (white) or poorly (magenta). The temporal profile of HFA activity is similar for electrodes that generalize well, showing a single peak in the movement phase. A cluster-based permutation test identified two periods where the HFA amplitude differed for contralateral and ipsilateral reaches, one during instruction and one well into the movement period. In contrast, the temporal profiles are radically different for those that generalize poorly, primarily because of the weak modulation during ipsilateral reaches. Interestingly, these electrodes also showed a double-peaked temporal profile during contralateral reaches. Similar multi-phasic activity has been observed in single unit activity in M1 during reaching (Churchland et al., 2012).

It is possible that similarity in temporal structure is obscured in the preceding analysis by the differences in HFA amplitude for the electrodes that showed poor generalization. To control for

this, we standardized the time series data by dividing each sample by the overall standard deviation (Insets: Fig 1.5C). Using the standardized traces, we calculated the linear correlation coefficient between the contralateral and ipsilateral traces, separately for instruction and movement. As expected, electrodes that generalized well across arms showed strong across-arm correlations for both task phases (Inset Fig 1.5C, left). In contrast, for electrodes that generalize poorly across arms, the correlation between arms was negative during instruction and then rose to a moderate positive correlation during movement (Inset Fig 1.5C, right). Thus, the poor generalization of these electrodes is generally due to the temporal divergence of the two arms during instruction, where the ipsilateral trace becomes inhibited compared to the contralateral trace. Interestingly, although the ipsilateral trace remains inhibited during movement, the temporal structure between the two arms re-emerges.

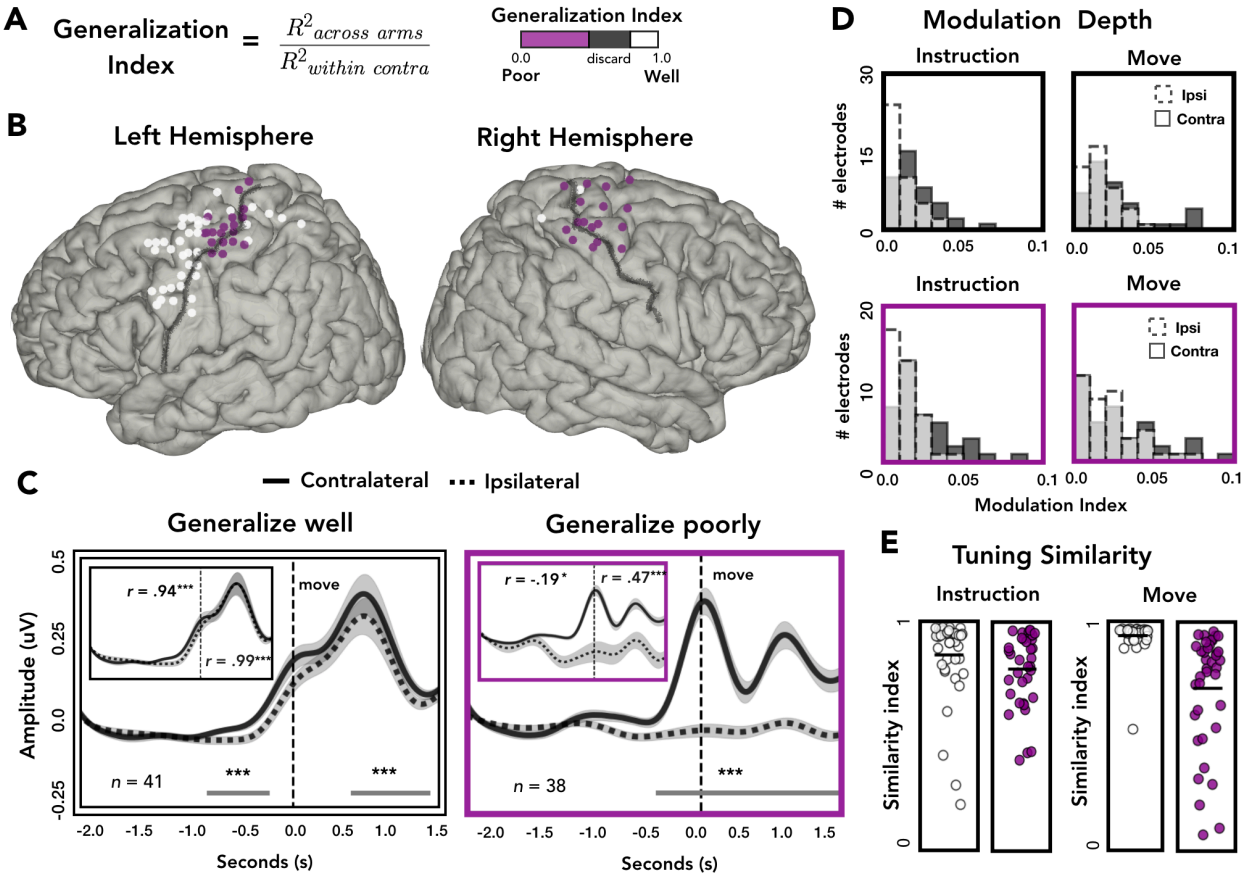

Figure 1.5. Spatial and temporal relationship of across-arm generalization. A) Generalization index. Electrodes were classified as showing good across-arm generalization (white, generalization index > .80) or poor across arm generalization (magenta; generalization index < .50). **B) Spatial distribution of across-arm generalization.** Electrodes that generalize well across arms (white) were primarily located in dorsal and ventral premotor regions of the left hemisphere. Electrodes that generalize poorly (magenta) were clustered around the putative arm area of the central sulcus in both the left and right hemispheres. **C) Amplitude differences**

across arms. Average contralateral (solid line) and ipsilateral (dashed line) predictions for electrodes that generalize well across arms (left) or generalize poorly (right). Significant clusters are represented with a gray line. Inset: Same data but standardized to highlight shape of the timeseries independent of absolute amplitude. D) Modulation depth. Depth of tuning was calculated during instruction or movement with either the ipsilateral or contralateral hand. Greater modulation was found during contralateral reaches and during movement. E) Tuning similarity. Across arms tuning similarity was calculated for electrodes that generalize well (white) or poorly (magenta). Electrodes that generalize well across arms had significantly more tuning similarity than electrodes that did not generalize. *p<0.05, **p<0.01, ***p<0.001, cluster permutation test, Pearson's correlation.

Temporal and spatial topography of across-arm generalization. To examine how generalization varied across the cortex, we categorized each electrode as showing either good across-arm generalization (decrease of up to 20% relative to within-arm performance) or poor across-arm generalization (decrease of more than 50%; Fig 5A). We focused on the extremes of the generalization distribution based on the assumption that these electrodes were more likely to share similar underlying neural profiles. This also allowed us to have similar numbers of electrodes in each group.

Target modulation and tuning similarity across arms. To examine the extent of target modulation for the contralateral and ipsilateral arm, we calculated the modulation depth of each electrode during the instruction and movement phases. The modulation index reflects the amount of variability in the signal captured by target tuning (or target specificity): A modulation index of .1 means 10% of the variance is captured by the difference between the response to the four target locations. The modulation values overall were relatively low (Fig 5D). However, it should be noted that the reaches were all within the fronto-parallel plane which comprise a considerably smaller range of movement compared to studies that use a center-out reaching task. For both electrode types (showing good or poor across arm generalization), there was a main effect of arm, with ipsilateral modulation lower than contralateral modulation ($p_{Generalize\_well} < .001$; $p_{Generalize\_poorly} < .005$). Both subgroups of electrodes also displayed a main effect of task phase, with the depth of modulation greater during the movement phase compared to the instruction phase ($p_{Generalize\_well} < .001$; $p_{Generalize\_poorly} < .005$). No significant interactions were found for either group.

We also examined the representational overlap between the two arms in terms of their tuning profiles. We computed a tuning similarity index, defined as the sum of squared errors for average HFA predictions to the same target between the contralateral and ipsilateral arms. A similarity index of 1 would correspond to identical tuning preferences for the arms whereas a similarity index of 0 would indicate completely disparate tuning preferences. The similarity data were analyzed with a mixed design permutation test, including the factors task phase and electrode type (good vs. poor generalizers). Electrodes that generalize well across the two arms (predominately found in the left hemisphere) showed more overlap of tuning preferences compared to electrodes that generalized poorly (main effect of generalizability: $p < .001$). While there was no effect of phase ($p = .758$), the interaction was significant ($p < .005$), with electrode

types showing more comparable tuning similarity during instruction and tuning similarity diverging during movement. Simple effects analysis revealed that for electrodes that generalize poorly, tuning similarity was higher during the instruction phase compared to the movement phase ($p < .001$). In contrast, for electrodes that generalize well, tuning similarity was higher during movement compared to instruction ($p < .001$). These analyses demonstrate that a number of electrodes in the left hemisphere strongly encode kinematic variables for both arms, including similar tuning preferences across the two arms, which was especially pronounced during the movement phase.

1.5 Discussion

Although the most prominent feature of cortical motor pathways is their contralateral organization, unimanual movements are well represented in the ipsilateral hemisphere. Single-unit activity and local field potentials obtained from motor cortex in non-human primates (Ganguly et al., 2009; Ames & Churchland, 2019), as well as ECoG activity in humans (Bundy, Szrama, Pahwa & Leuthardt, 2018; Ganguly et al., 2009, Wisneski et al., 2008) can be decoded to predict complex kinematic variables and EMG activity during arm movements of the ipsilateral arm. Here we extend this work by building a kinematic encoding model to examine how these features are represented in each hemisphere. We opted to build an electrode-wise encoding model which opened up new avenues for analysis. Electrode-wise encoding models allow prediction of the full time series for each electrode thus retaining the high spatial and temporal resolution of the intracranial signal. From these metrics we could compare kinematic encoding and across-arm generalization between the two hemispheres as well as the spatial distribution of the information-carrying electrodes within each hemisphere. We observed a marked hemispheric asymmetry: While contralateral movements were encoded similarly across the two hemispheres, ipsilateral encoding was much stronger in the left hemisphere, an effect that was especially pronounced during movement execution. In addition, there was greater overlap between the representation of contra- and ipsilateral movement in the left hemisphere compared to the right hemisphere.

Hemispheric asymmetry in movement encoding. We observed a striking asymmetry between the two hemispheres for ipsilateral movement encoding, with stronger bilateral encoding of the upper limbs in the left hemisphere compared to the right hemisphere. The effect size is quite substantial ($d = 1.34$), which exceeds Cohen's (1988) convention for a large effect ($d = .80$). We studied three patients per hemisphere, with each patient having at least 17 predictive electrodes, totaling 141 electrodes in the left hemisphere and 75 in the right hemisphere.

Given the size of the hemispheric asymmetry effect, it is surprising that this asymmetry has not be described in previous reports. This may in part reflect the smaller sample size in these studies. For example, in Bundy et al. (2018), three of the four patients had left hemisphere grids, leaving a hemisphere analysis dependent on the data from a single right hemisphere patient. Studies with non-human primates tend to ignore hemispheric differences, perhaps because these animals do not show consistent patterns of hand-dominance across individuals. One exception

here is a study by Cisek, Crammond and Kalaska (2003) who reported no hemispheric differences in neural recordings obtained from M1 and PMd during ipsilateral and contralateral arm reaches.

In addition to examining hemispheric differences in the encoding of unimanual movement, we also asked if kinematic features were encoded differently for contra- and ipsilateral movements by testing across-arm generalization. We categorized electrodes as showing either good across-arm generalization (decrease of up to 20% relative to within-arm performance) or poor across-arm generalization (decrease of more than 50%). This categorization scheme revealed a striking anatomical division, with electrodes showing good across-arm generalization clustering in the left premotor and parietal cortices and electrodes that generalized poorly clustering in left and right M1. Using the same categorization, we further examined the spatial tuning of the electrodes. Target tuning in the HFA band was found for both contralateral and ipsilateral movement, although ipsilateral tuning was significantly shallower. Interestingly, electrodes that generalized well across-arms had similar target tuning for each arm. This suggests that for these electrodes, ipsilateral signals are not just encoding generic movement, but encoding movement direction in a similar manner to contralateral signals. A similar overlap in tuning has been observed in single unit recordings from PMd (Cisek, Crammond & Kalaska, 2003) and can be inferred from the across-arm generalization decoding results reported by Bundy et al., (2018). In contrast, electrodes that failed to generalize, located primarily in M1 in either left or right hemisphere, exhibited disparate tuning for contra- and ipsilateral reaches.

One limitation of our study is that, because two of the left hemisphere patients had high density grid implants, there were fewer right hemisphere electrodes compared to the left hemisphere electrodes. However, all three right hemisphere patients had coverage over dorsal and ventral premotor cortices, making it unlikely that the poor across-arm generalization for right hemisphere electrodes is due to insufficient coverage.

Functional implications of hemispheric asymmetries in movement encoding. By using a delayed response task, we were able to segregate activity into an instruction phase during which the patient was presented with the target location for the forthcoming movement and a movement phase, defined at the onset of the reach. With this design, we found that the encoding model could predict neural activity during the instruction phase based on the kinematics of the forthcoming reach, evidence that the patients were indeed planning the upcoming movement.

This task phase analysis also revealed robust asymmetries between the two hemispheres. There was a main effect of hemisphere, with the left hemisphere displaying stronger bilateral encoding overall compared to the right hemisphere. However, there was also an interaction: In the left hemisphere bilateral encoding was stronger during the movement phase whereas in the right hemisphere bilateral encoding was stronger during the instruction phase. Surprisingly, in the left hemisphere the contralateral bias completely disappeared during the movement phase, with both the contra- and ipsilateral arms being encoded to the same extent. Stronger bilateral encoding during movement (compared to instruction) is surprising given the spatial distribution of electrodes that encode ipsilateral movement were primarily outside of M1, regions typically associated more with planning than execution (e.g., premotor cortices, parietal cortex).

The asymmetry observed here is in accord with the long-standing recognition of hemispheric asymmetries in praxis. Starting with the classic observations of Liepmann at the turn of the 20th century on the association of the left hemisphere and apraxia (Liepmann 1908, cited in Renzi, & Lucchelli, 1988; see also Schaefer et al., 2007) and continuing with functional imaging studies in neurotypical populations, a large body of evidence points to a dominant role for the left hemisphere in skilled movement often engaging bi-manual movements (Corballis, Badzakova-Trajkov & Häberling, 2012; Przybylski & Króliczak, 2017). This asymmetry is most pronounced in tasks involving functional object use (Buxbaum et al., 2006), symbolic gestures (Xu, Gannon, Emmorey, Smith & Bruan, 2009) and intransitive pantomimes (Bohlhalter et al., 2009). Apraxia, following left-hemisphere damage can be manifest in movements produced with either limb (Renzi, & Lucchelli, 1988), and are usually associated with lesions that encompass premotor and parietal cortices (Haaland, Harrington & Knight, 2000). While this asymmetry may be linked to hand dominance (Ochipa, Rothi & Heilman, 1989), functional imagining studies with relatively large sample sizes have shown that handedness only influences the strength of the left hemisphere bias for skilled movement but does not produce a reversal in left handers (Vingerhoets et al., 2012; Verstynen et al., 2005, Chettouf et al., 2020, Vingerhoets et al., 2013). Of the six patients tested in the current study, five are right-handed and the remaining patient reported being ambidextrous with a slight preference for using the left hand. We note that the results from this patient (L3) did not qualitatively differ from the other two left hemisphere patients.

Ipsilateral encoding was most prominent in the premotor and parietal cortex of the left hemisphere, overlapping with the neural regions implicated in praxis. However, two features of our results do not map on readily to an interpretation that focuses on hemispheric asymmetries in praxis. First, our task involved simple reaching movements, whereas praxis generally encompasses more complex learned movements associated with tool use or symbolic gestures. Second, ipsilateral encoding became more pronounced during movement execution; a priori, one might have expected this asymmetry to be more related to gestural intent and thus be more prevalent during movement planning.

An alternative hypothesis is that the ipsilateral activation is reflective of a prominent role of the left hemisphere in bimanual coordination. The encoding of ipsilateral arm movement might be a form of state representation, a means to keep track of the state of the ipsilateral arm given that many actions require the coordinated activity of the two limbs. This hypothesis, derived from the current data, is consistent with the increased ipsilateral encoding during the movement phase. The need to monitor the state of the other limb should hold for unimanual gestures performed with either limb. There is evidence in the neuropsychological literature pointing to a role of the left hemisphere in bimanual coordination in neuroimaging (Jäncke et al., 2000; Toyokura, Muro, Komiya & Obara, 1999; Maki, Wong, Sugiura, Ozaki & Sadato, 2008) and electrophysiological studies (Serrien, Cassidy & Brown, 2003). For example, Schaffer et al., (2020) observed greater impairments in bimanual coordination following left hemisphere stroke compared to right hemisphere stroke. Interestingly, the impairment was manifest prior to peak velocity, a finding interpreted as a disruption in predictive control. It may be that the left hemisphere makes an

asymmetric contribution to inter-limb coordination by tracking or predicting where both limbs are in space.

An important question for future work is to examine how ipsilateral representations in the left hemisphere are affected during more complex movements, including those that involve both limbs. Using fMRI, Diedrichsen, Wiestler and Krakauer (2013) compared ipsilateral movement representations during unimanual and bimanual movements. Within the primary motor cortex, ipsilateral representations could only be discerned during unimanual movement. However, caudal premotor and anterior parietal regions retained similar ipsilateral representation during uni- and bimanual movement. If the left hemisphere tracks both limbs to facilitate bimanual coordination, we would predict that ipsilateral representations in premotor cortex are retained more strongly in the left hemisphere compared to the right hemisphere when both arms are engaged in the task.

Using a kinematic encoding model, we observed a striking hemispheric asymmetry, with the left hemisphere more strongly encoding the ipsilateral arm than the right hemisphere, a finding that was apparent during preparation and amplified during movement. This asymmetry was primarily driven by electrodes positioned over premotor and parietal cortices, with strong contralateral encoding for electrodes positioned over sensorimotor cortex. One possible interpretation of our results is that these networks monitor the state of each arm, a prerequisite for most skilled actions.

Chapter 2

Stronger Ipsilateral Encoding in the Subthalamic Region Compared to Sensorimotor Cortex

2.1 Abstract

Movements of either the contralateral or ipsilateral arm produce changes in neural activity in the sensorimotor cortex as well as the subthalamic region in the basal ganglia. We analyze neural recordings from patients with a deep brain stimulation lead targeting the subthalamic nucleus as well as a cortical strip while they made repetitive hand opening and closing movements with one hand (contralateral or ipsilateral) or both hands. We fit the continuous EMG recorded during the task to the neural activity using a cross-validated encoding model. We find that during both unimanual and bimanual movements electrodes in the subthalamic region encode both hands equally well whereas in the sensorimotor cortex there was a strong contralateral bias. In addition, we found that electrodes in the subthalamic region generalize across arms better than the sensorimotor cortex and appear to be more sensitive to context (i.e., whether the other arm is engaged in the task or not).

2.2 Introduction

In concert with the thalamus, the basal ganglia and frontal lobe control voluntary limb movement (DeLong, 1979; Alexander, DeLong & Strick, 1986). Somatomotor regions in the basal ganglia receive inputs from several areas of the cerebral cortex including primary motor cortex (M1), supplementary motor area (SMA), and premotor cortex (PM; Alexander & Crutcher, 1990). After the information is processed in the basal ganglia it returns back to the aforementioned motor cortices via the thalamus (Parent & Hazrati 1995; Middleton & Strick, 2000). In patients with Parkinson's disease (PD) cell death in the substantia nigra (inferior portion of the basal ganglia) results in disruptions of this cortio-basal ganglia motor loop leading to motor symptoms such as tremor, rigidity and bradykinesia (Dauer & Przedborski, 2003). Deep brain stimulation (DBS) of the subthalamic nucleus (STN) or globus pallidus (GP) has revolutionized treatment for patients with PD and provided a tool for scientists to further understand PD and basic motor control (Kumar et al., 1998).

Movement difficulties are accompanied by exaggerated beta (15-30 Hz) oscillations in the STN (Kühn et al., 2005, Little & Brown 2014). Overly synchronized beta oscillations are thought to be a result of chronic dopamine depletion, as these oscillations and motor symptoms are reduced by dopaminergic therapies (Weinberger et al., 2006) and in animal models dopamine loss leads to excessively synchronized beta oscillations (Mallet et al., 2008). More recently, network

dynamics have been considered between the STN and the cortex. In the primary motor cortex of PD patients, the amplitude of high frequency activity couples with the phase of the beta rhythm in the STN, and this coupling becomes more exaggerated as Parkinsonian motor symptoms increase and can be alleviated with DBS (De Hemptinne, 2015).

The basal ganglia have been primarily implicated in inhibiting or changing motor plans (Mink, 1996), but more recent studies suggest it may also contribute to the control of on-going movements (Yttri & Dudman, 2016). In PD patients, neuronal activity in the STN is associated with upper limb movements (Abosch, Hutchison, Saint-Cyr, Dostrovsky & Lozano, 2002; Rodriguez-Oroz et al., 2001) and neural activity and local field potentials (LFP) in the STN have been used to decode grip force (Patil, Carmena, Nicolelis & Turner, 2004; Tan et al., 2016). Although these studies focus primarily on the contralateral arm relative to the DBS lead, bilateral changes in the oscillatory activity in the STN are observed during unimanual movements of either hand (Alegre et al., 2005). In addition, phase coherence between the left and right STN increases in the alpha range during unimanual movements, suggesting that although there is no direct anatomical connections between bilateral STN there are physiological connections (Darvas & Hebb, 2014). In accord with these findings, after unilateral implantation of STN DBS, improvement on the Unified Parkinson's Disease Rating Scale (UPDRS) was observed for both contralateral and ipsilateral movements, although as expected, the contralateral benefit was larger (Walker, Watts, Guthrie, Wang & Guthrie, 2009).

In the present study, we examine how continuous contralateral and ipsilateral movements are encoded in the STN and sensorimotor cortex from data obtained intraoperatively during DBS surgery. The data were collected from 13 patients, each with a directional DBS lead and a ECoG strip over sensorimotor cortex while they produced repetitive voluntary hand movements with either the hand contralateral or ipsilateral to the implanted electrodes or both hands simultaneously. In order to retain the high spatial and temporal resolution of the neural signals, we opted to use an encoding model which uses EMG activity during the task to predict neural activity for each electrode. For our electrode-wise encoding model we focus on predicting the local motor potential, which has been shown previously to correlate with hand movements (Schalk et al., 2007; Flint, Eric, Jordan, Miller & Slutzky 2013). We utilize this approach to better understand differences in encoding between the sensorimotor cortex and STN region during unimanual and bimanual movements. In addition, we examine representational overlap in encoding across hands and across unimanual and bimanual movements by training the model on one condition and attempting to predict neural activity in another condition.

2.3 Method

Patients. Intracranial recordings were collected from 13 patients (4 women; 59.27 years old). Patients were recruited from University of Alabama at Birmingham (UAB) medical center as part of two different studies. The study was comprised of a randomized, double-blind crossover study of directional versus circular STN DSB for moderately advanced Parkinson's disease. Consensus inclusion/exclusion criteria for recruitment, screening, enrollment, and DBS surgery was strictly

followed. All procedures were approved by the institutional review boards at UAB, and all patients provided informed consent prior to participating in the study.

ECoG strip and lead location. Before DBS surgery the pre-op 3T PRISMA brain MR images are co-registered with the intra-op O-arm 2 CT images and standard frame-based stereotaxy is used to target the STN. A temporary 6 contact Ad-Tech ECoG strip is passed over the "hand knob" of ipsilateral sensorimotor cortex, in the manner pioneered by Starr (De Hemptinne et al., 2013; De Hemptinne et al., 2015; Crowell et al., 2012). We then use frame-based stereotaxy, multipass single unit microelectrode recordings, macrostimulation, and intraoperative O-arm 2 CT imaging to select an appropriate trajectory for the permanent location of the DBS lead. We placed the Boston Scientific lead at a defined electrophysiological depth, such that the two middle rows (with the directional contacts) are equidistant from the dorsal STN border, based upon the single unit recording profile within that trajectory. For the DBS probe, the upper directional row (contacts 5, 6, and 7) is just dorsal to STN in zona incerta / anterior thalamus, and the lower directional row (contacts 2, 3, and 4) are within the dorsolateral sensorimotor STN (Figure 2.2A).

Behavioral Task. A motor behavior battery was collected intraoperatively, measuring simple, repetitive voluntary movements from the Unified Parkinson's Disease Rating scale (UPDRS) in a blocked design. Along with contralateral hand (relative to implanted electrodes) opening-closing which is part of the UPDRS, two additional movements were collected 1) ipsilateral hand opening-closing and 2) bimanual hand opening-closing. The primary motion during this movement is at the metacarpophalangeal and proximal interphalangeal joints. All patients completed at least 2 blocks consisting of 10 seconds of continuous movement for each condition. Participants received verbal instructions for each task just prior to execution, and they performed movements repeatedly in a block following the verbal commands "ready, set, go" for 10 seconds until they hear the word "stop." Surface electromyography (EMG) from the bilateral hands or arms [either the first dorsal interosseous (FDI) muscle, flexor carpi radialis (FCR) muscle, or both] was recorded during the movements.

Data acquisition and preprocessing. DBS surgeries were conducted awake and "off" dopaminergic medications. Electrophysiological signals were recorded from a BrainVision ActiChamps acquisition system, sampled at 25 kHz without digital filters. We simultaneously recorded (1) LFPs from the DBS probe; (2) LFPs from the 6 ECoG contacts over primary sensorimotor cortex; and (3) surface EMG from the hand/arm.

Digital preprocessing included the following steps. First, all neural data were low-pass filtered at 500 Hz with a fourth-order Butterworth filter as an anti-aliasing measure before downsampling to 1000 Hz. Next, neural data were high-pass filtered at 0.5 Hz with a third-order Butterworth filter to remove slow drifts in the data. We then re-referenced the signal from each electrode using a common average reference montage within each neural area (sensorimotor cortex and STN region) separately. Electrodes were then notch-filtered at 60, 120 and 180 Hz to remove line noise from electronic devices powered by outlets in the operating room. Lastly, the neural signals were low-pass filtered at 10 Hz to extract the local motor potential (LMP) which has been

shown to correlate with hand movements and hold substantial information about movement direction (Schalk et al., 2007; Flint, Eric, Jordan, Miller & Slutzky 2013).

Similar to the neural data, all EMG signals were first low-pass filtered at 500 Hz as an anti-aliasing measure before downsampling to 1000 Hz. Next, each EMG channel was z-scored, high-pass filtered at 50 Hz, and full-wave rectified (Flint, Ethier, Oby, Miller & Slutzky, 2012). Last, EMG data were low-pass filtered at 10 Hz to obtain an envelope of the movements. All filters were fourth-order, non-causal Butterworth filters. The EMG data were then visually inspected and portions with excessive noise were excluded from further analyses. For unimanual conditions, if the other hand was moving, we did not include the block in the encoding model.

Encoding model. The processed EMG signal of a single arm was used as the sole feature in the model used to predict the LMP for each electrode. This feature is time-lagged with lags extending from 500 ms before movement onset to 500 ms after movement onset (sampling rate at 1000 Hz). This wide range of lags provides a way to compensate for the anticipated asynchrony between neural data and movement. LMP at each time point [LMP(t)] was modeled as a weighted linear combination of the hand EMG at different time-lags, resulting in a set of beta weights, b1 …, b1000. To make the beta weights scale-free, the EMG features are z-scored and neural LMPs are normalized using the common average reference of their respective brain regions before being fit by the model.

Model fitting. Regularized (ridge) regression (Hoerl and Kennard, 1970) was used to estimate the weights that map EMG to the corresponding LMP signal for each electrode.

$$\hat{\beta} = \left(X^T X + \lambda I\right)^{-1} X^T Y$$

For within-arm model fitting, the total dataset consisted of all clean, successful movements performed with either the ipsilateral arm, contralateral arm or both (each condition was fit separately). Nested five-fold cross-validation was used to select the regularization hyperparameter on inner test sets (validation sets) and assess prediction performance on separate, outer test sets. At the outer level, the data was partitioned into five mutually exclusive estimation and test sets. For each test set, the rest of the data acted as the estimation set. For each outer fold, we further partitioned our estimation set into five mutually exclusive inner folds to train the model (80% of estimation set) and predict neural responses across a range of regularization values on the validation set (20% of estimation set). For each inner fold, the regularization parameter value was selected that produced the best prediction as measured by the linear correlation of the predicted and actual LMP. The average of the selected regularization parameters across the five inner folds was computed and used to calculate the prediction of the LMP on the outer test set. This procedure was done at the outer level five times. Our primary measure is held-out prediction performance (R^2), which we quantified as the squared linear correlation between the model prediction and the actual LMP time series, averaged across the five mutually exclusive test sets.

To be considered as predictive, we established a criterion that an electrode must account for at least 1% of the variability in the LMP signal ($R^2 > .01$) for either ipsilateral or contralateral reaches (previous papers report electrodes with $R^2 > .005$ as predictive; Downey et a., 2020). Electrodes not meeting this criterion were not included in subsequent analyses.

For across-arm model fitting, the same procedure was used except the test set was partitioned from the total dataset of the other arm. For across-condition model fitting, the same procedure was used except the test set was partitioned from the total dataset of the bimanual condition of the same arm. We partitioned the data in this manner (80% estimation, 20% test) to make the fitting procedure for the across-arm and across-condition models comparable to that employed in the within-arm model.

2.4 Results

Comparing predictive electrodes across brain regions. We examined the extent that muscle activity was encoded for contralateral and ipsilateral hand movements in individual electrodes over sensorimotor cortex (SMC) and within the STN region (STN). To do this we fit an encoding model that maps continuous electromyographic activity to the LMP signal for 182 electrodes (SMC = 78, STN = 104). This procedure was done separately for contralateral and ipsilateral movements using either the contralateral EMG or the ipsilateral EMG as features in the model. We quantified the cross-validated model fit by generating LMP predictions using the EMG signal from held-out trials of the same condition and calculating prediction performance as the square of the linear correlation (R^2) between the predicted and actual LMP signal. Electrodes were considered predictive (i.e., encoding muscle activity) if they could account for at least 1% of the neural variance ($r > .10$; $R^2 > .01$) in held-out test sets during contralateral or ipsilateral movements. Because significance depends on sample size and we are predicting the time series across tens of thousands of samples we can observe significance at very low correlations, hence we decided to use a criterion based on effect size (R^2) which is less affected by the length of the held-out test set. This means that although we may see significant correlations below a R^2 of .01, we choose to only consider electrodes predictive if they can predict at least 1% of the neural variance.

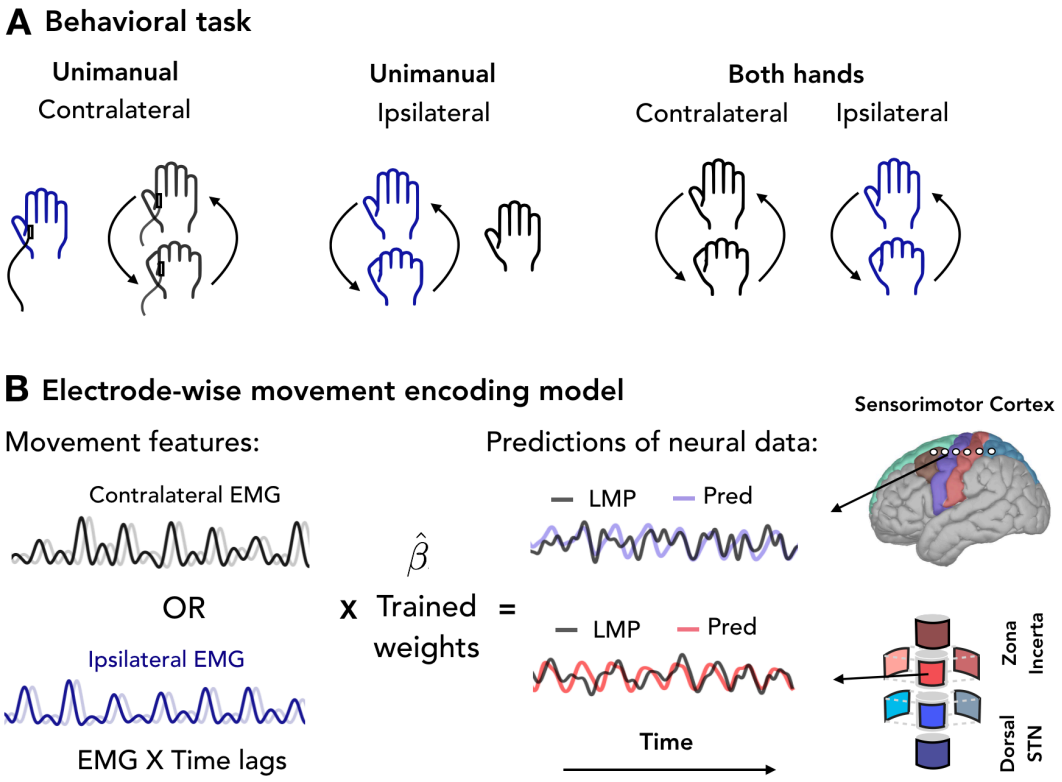

Figure 2.1. A. Behavioral task. Patient's engaged in hand opening and closing with either the hand contralateral, ipsilateral or with both hands. B. Electrode-wise encoding model. A cross-validated encoding model was used to predict the local motor potential (LMP) for each electrode over sensorimotor cortex and in the STN region from EMG of either the contralateral or ipsilateral hand.

Figure 2.2 summarizes the percentage of predictive electrodes across the SMC and STN areas for the unimanual and bimanual task conditions. Electrodes were categorized as being predictive of 'Both' hands if the threshold was met for both models using either the contralateral or ipsilateral EMG as features, as predictive of 'Contra only' if the electrode was predictive using contralateral EMG as features but not ipsilateral EMG, as predictive of 'Ipsi only' if the electrode was predictive using the ipsilateral EMG as features but not the contralateral EMG and was predictive of 'None' if it was not predictive for either model. Contrasting brain areas (SMC and STN) across unimanual movements we see a larger percentage of electrodes solely encoding contralateral compared to ipsilateral movements in the SMC, whereas in the STN the number of electrodes solely encoding either hand is more balanced. Although there are differences across areas and task conditions, we find a substantial percentage of electrodes encode ipsilateral movements across all four combinations of brain region and task condition as the percentage of electrodes that encode 'Both' hands never drops below 27% and the percentage of electrodes that encode 'Ipsi only' never drops below 7% totaling 34% of the electrodes that encode ipsilateral movement to at least some extent. Similarly, that percentage never drops below 47% for

contralateral movements across the four combinations. Contrasting unimanual and bimanual movements across brain region we see that moving from the unimanual to the bimanual condition the percentage of electrodes that encode both hands increases. Interestingly, the increase in electrodes that encode 'Both' seems to primarily come from the category 'Contra only' in the SMC case, but to come primarily from 'Ipsi only' category in the STN case. Currently, these categories only describe whether there is some level of encoding, but not the extent to that encoding, we delve into the extent of encoding in the following sections.

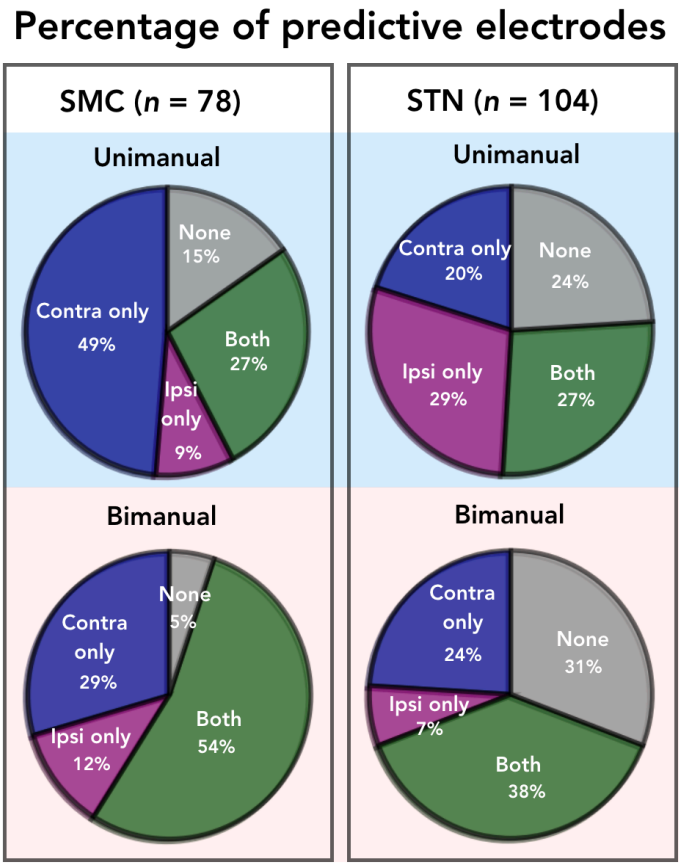

Figure 2.2. Predictive electrodes across conditions and brain regions. Electrodes were categorized as being predictive of neural activity ($R^2 > .01$) using only the contralateral EMG (Contra only), only the ipsilateral EMG (Ipsi only), both the contralateral or the ipsilateral EMG (Both) or neither EMGs across the unimanual and bimanual conditions in the SMC and the STN.

Stronger ipsilateral encoding in the STN region compared to sensorimotor cortex.
We next focus on predictive electrodes (excluding electrodes that were categorized as 'None' in the prior analysis) and examine the extend of encoding across electrodes

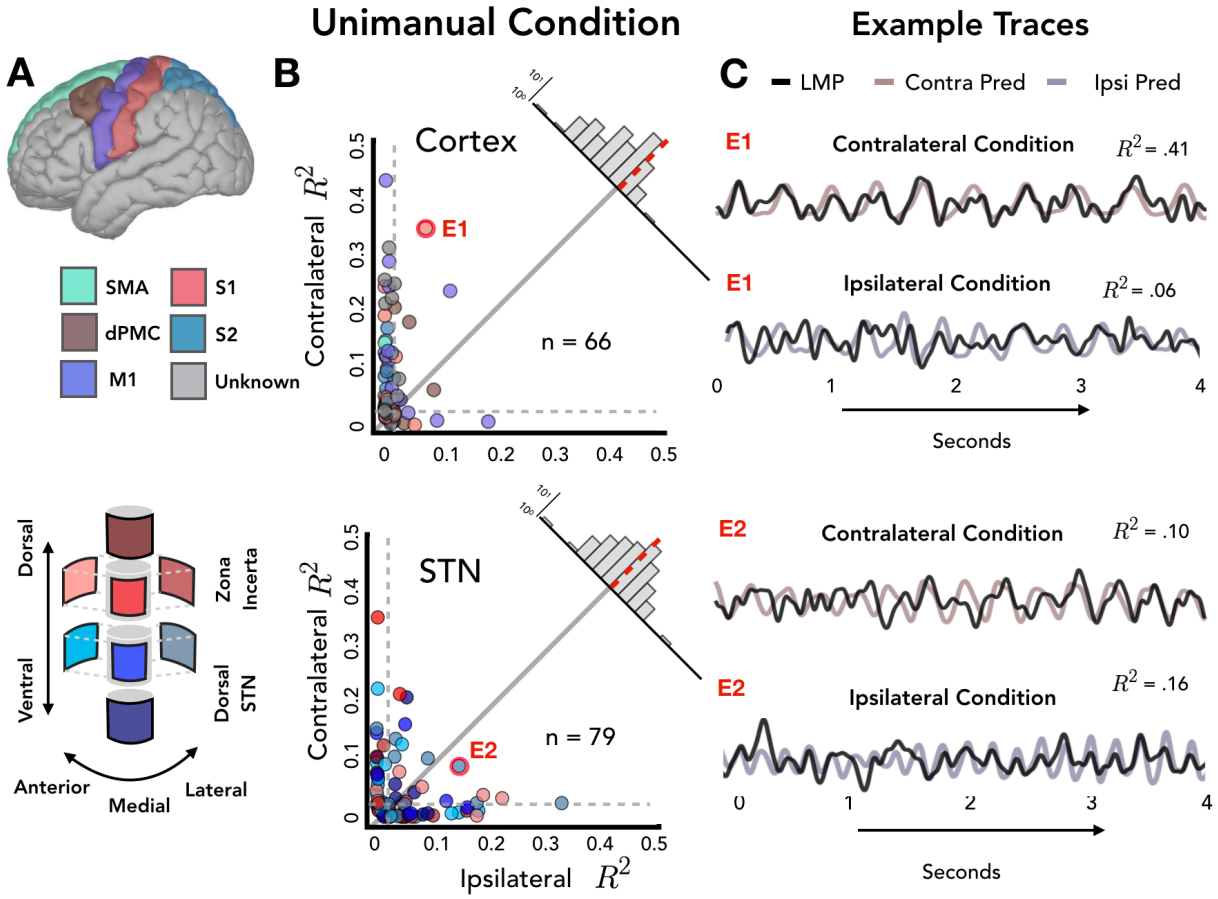

Figure 2.3. A. Electrode locations. Color corresponds to the location of the electrode either on the surface of the cortex or the deep directional probe in the STN region. **B. Stronger ipsilateral encoding in the STN region during unimanual movements.** Performance of all predictive electrodes, measured as the square of the Pearson correlation (R^2), using EMG from either the contralateral (Y-axis) or ipsilateral (X-axis) hand during unimanual movements. Overall performance did not vary between the two brain regions, but a significant interaction was found with electrodes in the STN region performing equally well across hands whereas a strong contralateral bias was found in SMC. C. Example traces. Held-out predictions of the LMP time series based on EMG recorded from the moving contralateral or ipsilateral hand for one exemplar electrode over S1 and one electrode in the dorsal STN.

during unimanual movements within the SMC and STN. Figure 2.3A provides a color map depicting the cortical parcellations SMC electrodes were located in and electrode type and location of the STN probe. Figure 2.3B compares the predictive performance of each electrode for the contralateral (Y-axis) and ipsilateral (X-axis) conditions for electrodes residing on SMC or in the STN region. Values close to the unity line yield a similar level of prediction performance for the two hands; values off the unity line indicate that encoding is stronger for one hand compared to the other. A mixed effects permutation test with fixed factors of Hand, Brain Region and a random effect of Patient revealed a significant main effect of Hand (μ_{contra} = .070, μ_{ipsi} =

.036, χ^2 = 16.960, p < .001) but no effect of Brain Region ($\mu_{\mathbf{cortex}}$ = .056, $\mu_{\mathbf{STN}}$ = .050, χ^2 = .517, p > .60). Most importantly, a significant interaction between Hand and Brain Region was also found (χ^2 = 27.221, p < .001), which indicates that although there was a strong contralateral bias in the electrodes over sensorimotor cortex ($\mu_{\mathbf{contra}}$ = .096, $\mu_{\mathbf{ipsi}}$ = .017, χ^2 = 37.559, p < .001), this bias was not found for electrodes in the STN region ($\mu_{\mathbf{contra}}$ = .048, $\mu_{\mathbf{ipsi}}$ = .052, χ^2 = 0.139 p > .70).

This suggests that unimanual movements of either hand are encoded to a similar extent in the STN whereas contralateral movements are being encoded more strongly in SMC. In line with this result, we see no difference in average prediction performance across the two regions (e.g., SMC and STN), which may seem surprising since neurons in the STN have only recently been suggested to contribute to ongoing movements. When we examine this effect further, we see that for contralateral movements the SMC performs significantly better than STN ($\mu_{\mathbf{SMC}}$ = .096, $\mu_{\mathbf{STN}}$ = .048, χ^2 = 15.133 p < .001), but for ipsilateral movements the opposite is true, STN performs significantly better than SMC ($\mu_{\mathbf{SMC}}$ = .017, $\mu_{\mathbf{STN}}$ = .052, χ^2 = 20.751 p < .001). Last, we computed the difference distributions for SMC and STN (Figure 2b, upper right corner) in order to compare the shape of the distributions. We found that the difference distribution for SMC was moderately skewed ($\mathbf{skewness}_{\mathbf{SMC}}$ = 0.849) whereas the difference distribution of the STN region approximated a normal distribution ($\mathbf{skewness}_{\mathbf{STN}}$= 0.287), which follows the SMC being more lateralized compared to STN.

The previous results focus on unimanual movement, it is of interest if contralateral and ipsilateral encoding changes when both hands are moving. We first compare contralateral and ipsilateral encoding in the SMC and STN within the bimanual condition and next examine the factors Hand and Brain Region across Task. Figure 2.3A provides the same color maps as 2.2A with regard to electrode location in SMC and STN. Figure 2.3B compares the predictive performance of each electrode when either the contralateral (Y-axis) or the ipsilateral (X-axis) EMG were fit as features during the condition when both hands were moving. Values close to the unity line yield a similar level of prediction performance when the EMG of either hand is used in the model; values off the unity line indicate that encoding is stronger for one hand compared to the other. Similar to the unimanual condition, we fit a mixed effects permutation model with fixed factors of Hand, Brain Region and a random effect of Patient. In line with our unimanual results we again found a significant main effect of Hand ($\mu_{\mathbf{contra}}$ = .077, $\mu_{\mathbf{ipsi}}$ = .041, χ^2 = 13.356, p < .001) but this time we also found a significant effect of Brain Region ($\mu_{\mathbf{cortex}}$ = .075, $\mu_{\mathbf{STN}}$ = .046, χ^2 = 7.781, p < .05). Most importantly, we also found a significant interaction between Hand and Brain Region (χ^2 = 8.899, p < .01) following a similar pattern we saw in the unimanual condition, with a strong contralateral bias in the electrodes over sensorimotor cortex ($\mu_{\mathbf{contra}}$ = .108, $\mu_{\mathbf{ipsi}}$ = .042, χ^2 = 21.359, p < .001) and similar encoding for electrodes in the STN region ($\mu_{\mathbf{contra}}$ = .051, $\mu_{\mathbf{ipsi}}$ = .040, χ^2 = 1.103 p > .30). This suggests that the different

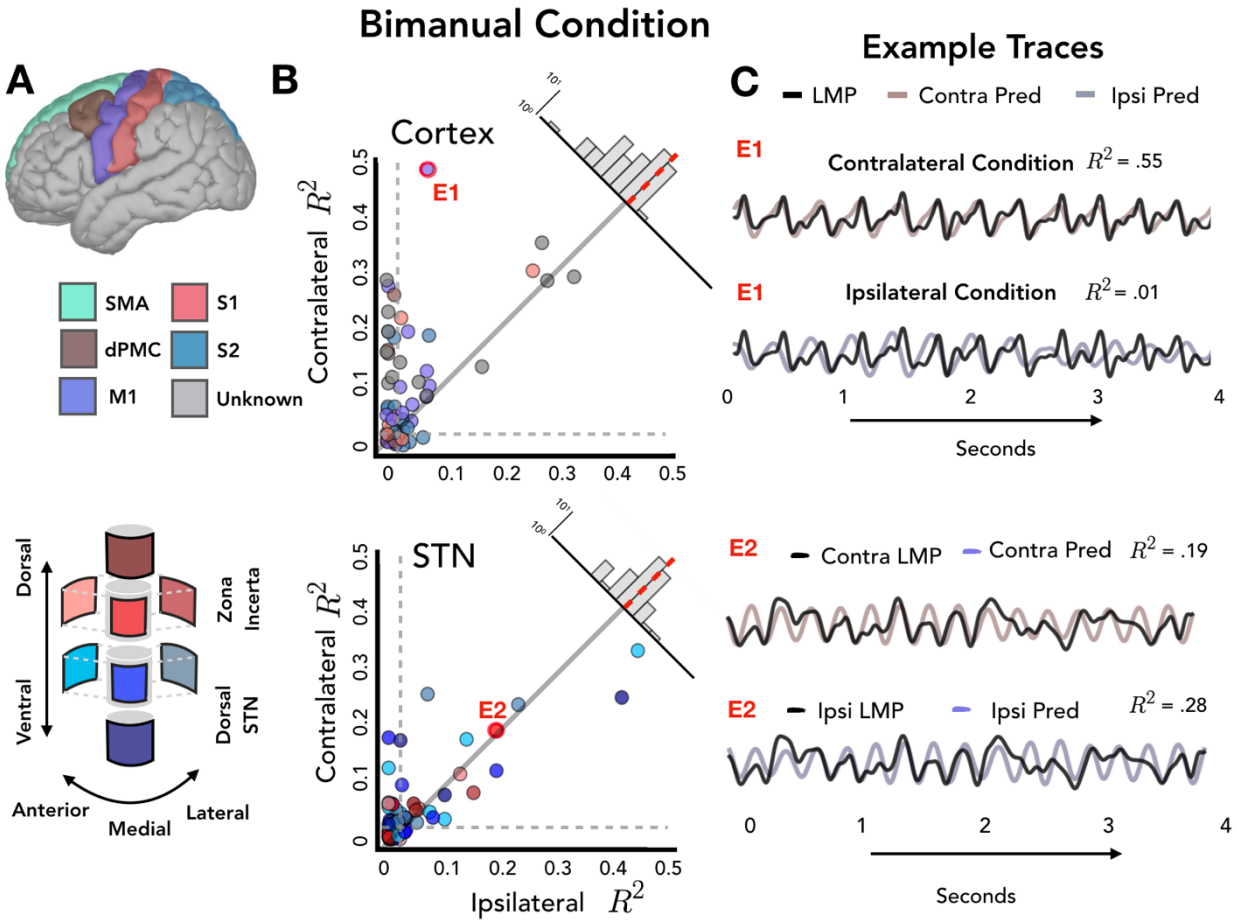

Figure 2.4. A. Electrode locations. Color corresponds to the location of the electrode either on the surface of the cortex or the deep directional probe in the STN region. **B. Stronger ipsilateral encoding in the STN region during bimanual movements.** Performance of all predictive electrodes, measured as the square of the Pearson correlation (R^2), using EMG from either the contralateral (Y-axis) or ipsilateral (X-axis) hand during bimanual movements. Again, a significant interaction was found between hand and brain region with electrodes in the STN region performing equally well across hands whereas a strong contralateral bias was found in SMC. C. Example traces. Held-out predictions of the LMP time series based on EMG recorded from the moving contralateral or ipsilateral hand during bimanual movements for one exemplar electrode over M1 and one electrode in Zora Incerta.

patterns of encoding for the contralateral and ipsilateral hands we see in the SMC and STN remains even when both hands are moving. One difference we do see across the unimanual and bimanual condition is that in the unimanual condition we did not see a difference in Brain Region and in the bimanual condition we do see a difference. To properly assess how the factor of Task (e.g., unimanual vs. bimanual) affects encoding across Hand and Brain Region we fit another mixed effects model with these three factors and a random effect of Patient. We did not find an interaction between Task and Hand (χ^2 = 0.012 p > .90), but we did find a trending interaction between Task and Brain Region (χ^2 = 3.162 p < .10) which can be explained through a significant

three way interaction between Task, Hand and Brain Region (χ^2 = 36.470 p < .001). Analyzing simple effects we find that the three way interaction is driven by ipsilateral encoding becoming stronger from the unimanual to the bimanual condition in SMC (μ_{uni} = .017, μ_{bi} = .042, χ^2 = 8.526 p < .001), but remaining approximately the same in the STN (μ_{uni} = .051, μ_{bi} = .041, χ^2 = 0.518 p > .40). Contralateral encoding did not change across task condition in either the SMC or STN (all χ^2's < 0.751 p > .40). This suggests that although ipsilateral encoding is weaker in the SMC compared to the STN, only in the SMC did ipsilateral encoding increase in the bimanual condition. This result is also in line with our analysis categorizing predictive electrodes, in the SMC 9% of electrodes were solely encoding ipsilateral movements and this slightly increased to 12% during the bimanual condition, whereas the percentage of electrodes solely encoding ipsilateral signals in the STN went down from 29% to 7%.

The preceding analyses focused on an encoding analysis for within-hand prediction, we next evaluate the overlap between the neural representations for contralateral and ipsilateral movement. To this end, we examined across-hand prediction performance by training the encoding model with the data from movements produced with one hand and testing prediction performance using the data from movements produced with the other hand. Figure 2.5A again depicts the color maps with regard to electrode location in SMC and STN. Figure 2.5B compares the predictive performance of each electrode when either the model was trained and tested within the same hand (train contralateral, test contralateral; Y-axis) or across hands (train contralateral, test ipsilateral; X-axis). Values close to the unity line have more overlapping neural representations during contra- and ipsilateral movement, whereas electrodes off the unity line encode the two hands differentially. We fit a mixed effects permutation model with fixed factors of Hand Generalization, Brain Region and a random effect of Patient. We found a main effect of Hand Generalization, with within arm predictions outperforming across arm predictions (μ_{within} = .070, μ_{across} = .009, χ^2 = 72.277 p < .001), and a main effect of Brain Region with SMC outperforming STN (μ_{SMC} = .050, μ_{STN} = .030, χ^2 = 6.45 p < .01). Importantly, we also found a significant interaction between Hand Generalization and Brain Region (χ^2 = 17.226 p < .001) which suggests that although STN had lower encoding overall, STN had relatively better generalization between the two hands compared to STM and thus more similar representations between the two hands.

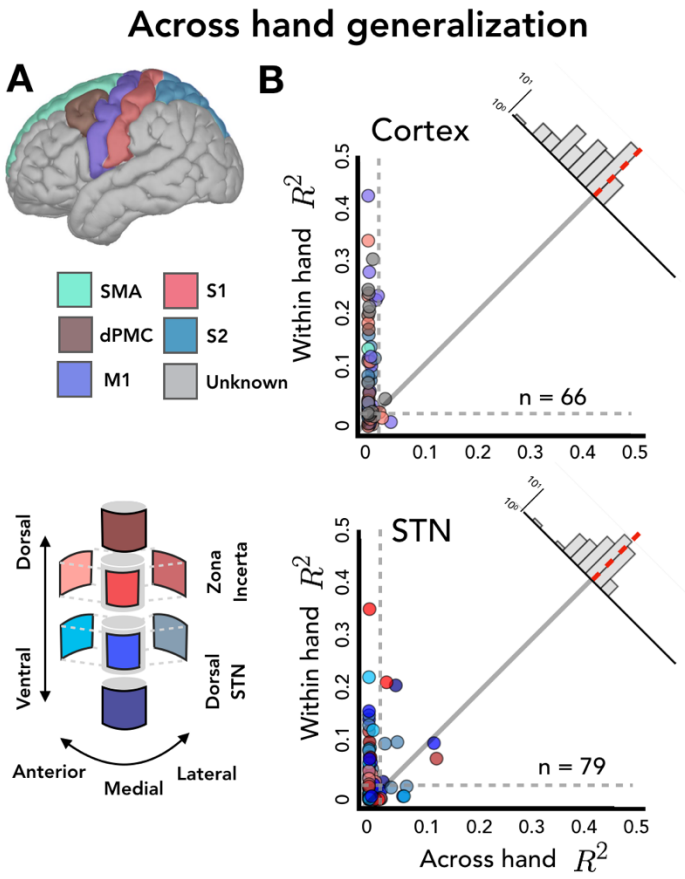

Figure 2.5. A. Electrode locations. Color corresponds to the location of the electrode either on the surface of the cortex or the deep directional probe in the STN region. **B. Stronger across-hand generalization in the STN.** Performance of all predictive electrodes, measured as the square of the Pearson correlation (R^2), using EMG from either the same hand (Y-axis) or training and testing across hands (X-axis) during unimanual movements. Overall electrodes in the STN had lower predictions, but a significant interaction was also found where electrodes were able to generalize across hands better compared to SMC.

We next examine task generalizability, allowing us to examine how contralateral encoding changes from unimanual movements to movements simultaneously produced with both hands. To do this we examined across-task prediction performance by training the encoding model with the data from movements produced with one hand and testing prediction performance when both hands were moving. Figure 2.6A again depicts the color maps with regard to electrode location in SMC and STN. Figure 2.6B compares the predictive performance of each electrode when either the model was trained and tested within the same condition (train unimanual contra, test unimanual contra; Y-axis) or across conditions (train unimanual contra, test bimanual contra; X-axis).

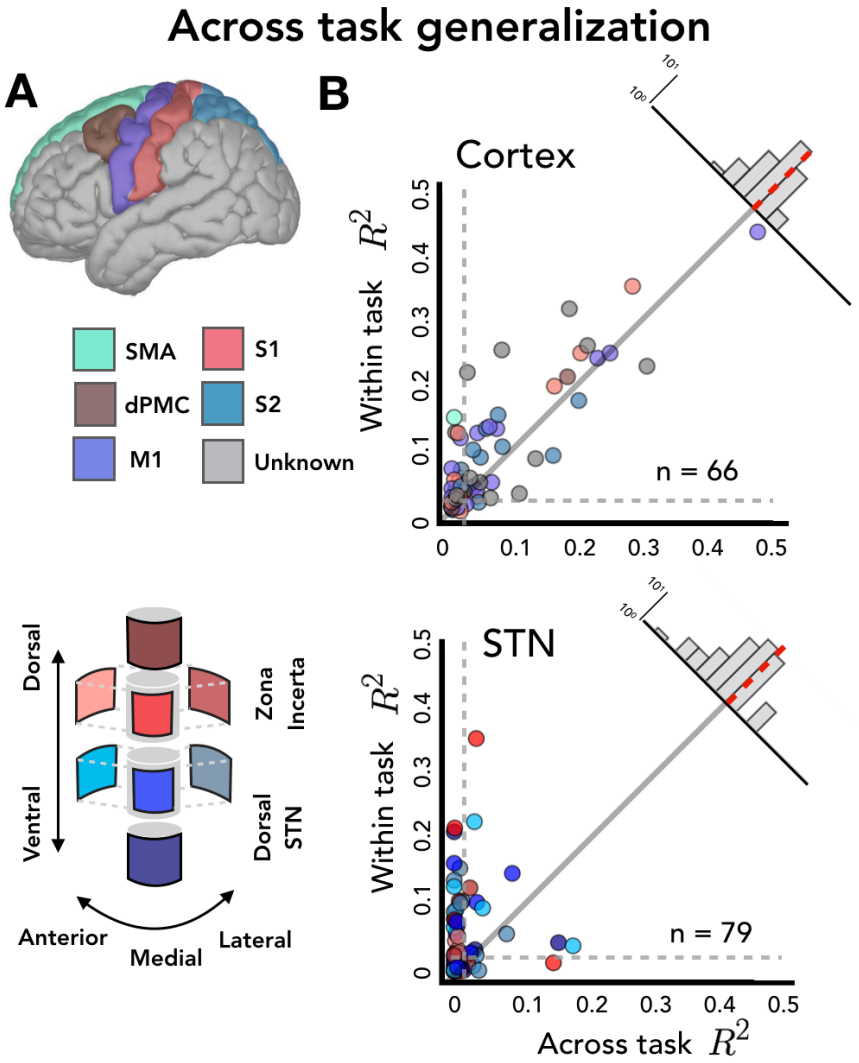

Figure 2.6. A. Electrode locations. Color corresponds to the location of the electrode either on the surface of the cortex or the deep directional probe in the STN region. **B. STN is more context dependent than SMC.** Performance of all predictive electrodes, measured as the square of the Pearson correlation (R^2), using EMG from either the same task (unimanual; Y-axis) or training and testing across tasks (unimanual to bimanual; X-axis). No mean shift was found between the SMC and STN, but the STN difference distribution was more skewed suggesting more electrodes failed to generalize across tasks.

For this analysis, the extra component that is added from the unimanual to the bimanual condition is that the ipsilateral hand is also moving (i.e., in both conditions the contralateral hand is moving), if there is strong generalizability across conditions (i.e., values close to the unity line) this can be interpreted as the neural signal ignoring information about the ipsilateral hand moving. Electrodes off the unity line can be interpreted as being more context dependent - that is the neural signal changes when the ipsilateral hand is also engaged in the task compared to when the contralateral hand is moving in isolation. We fit a mixed effects permutation model

with fixed factors of Task Generalization, Brain Region and a random effect of Patient. We found effect of *Task Generalization,* with within task predictions outperforming across task predictions (μ_{within} = .070, μ_{across} = .040, χ^2 = 14.238 p < .001), and a main effect of *Brain Region* with SMC outperforming STN (μ_{SMC} = .082, μ_{STN} = .032, χ^2 = 33.08 p < .001). We did not find a significant interaction between the two factors (χ^2 = 0.063 p > .70) which suggests that both areas decreased in performance to a similar extent when generalizing across task conditions. Although there was not a mean shift in task generalizability, we also examine the shape of the distributions and find that SMC is moderately skewed ($skewness_{SMC}$ = 0.810) whereas the STN is severally skewed ($skewness_{SMC}$ = 1.210), suggesting there are more electrodes in the STN that fail to generalize across task and hence are more context dependent.

2.5 Discussion

We aimed to compare contralateral and ipsilateral movement encoding during unimanual and bimanual hand opening and closing in the SMC and STN region. During both unimanual and bimanual movements we found a different pattern of encoding across the two brain regions, with the contralateral hand being more strongly encoded than ipsilateral movements in the SMC and both hands being encoded equally in the STN. We also found evidence that the STN is better able to generalize across hands and may be more context dependent than SMC. One benefit of our approach using a movement-based encoding model is that we are using the same features (EMG signal) to simultaneously fit electrodes in the SMC and STN, thus enabling us to limit confounds such as motor variability, noise because these are exactly matched across the two regions.

Overall movement encoding in the SMC and STN. Although the STN has only been implicated in the control of on-going movements more recently (Yttri & Dudman, 2016), we did not find a difference in the overall level of encoding of unimanual hand movements between the SMC and STN. Examining this pattern further we see that electrodes over SMC outperform STN electrodes for contralateral movements, whereas the STN outperforms the SMC for ipsilateral movements. This result matches our categorical analysis, in the SMC 49% of electrodes encode contralateral movements only and only 7% encode ipsilateral movements only, whereas in the STN 20% of electrodes encode contralateral movements only and 29% encode ipsilateral movements only. This suggests that although the overall level of encoding may be similar across the two regions, the STN appears to encode both hands at a moderate level whereas the SMC strongly encodes the contralateral hand and more weakly encodes the ipsilateral hand ($\mu_{\mathrm{STN_{contra}}}$ = .048, $\mu_{\mathrm{STN_{ipsi}}}$ = .052,$\mu_{\mathrm{SMC_{contra}}}$ = .096, $\mu_{\mathrm{SMC_{ipsi}}}$ = .017).

Examining bimanual movements, we found a significant difference between SMC and the STN in the overall level of encoding. We found that this was primarily driven by a three-way interaction between Hand, Brain Region and Task, in which ipsilateral encoding increased from the unimanual to the bimanual condition in the SMC, but in the STN the level of ipsilateral encoding remained approximately the same. A divergence in the level of encoding between the SMC and

STN from unimanual to bimanual movements is also supported by our categorical analysis of predictive electrodes. During unimanual movements the percentage of electrodes that do not encode either hand in the SMC and STN are 15% and 24% respectively. Moving to the bimanual condition, the percentage of electrodes that do not encode either hand shrinks to 5% in the SMC and increases to 31% in the STN. This may point to a diverging role of these two brain regions in terms of unimanual and bimanual movements. More research would be needed, ideally during bimanual movements where the two hands were coordinated, to better understand this phenomenon.

Possible applications for adaptive DBS. Unidirectional DBS has been used as a therapeutic device to treat Parkinson's disease for 30 years, yet the majority of DBS technologies are still based on constant-amplitude neurostimulation (Lozano et al., 2019). Many patients with an implanted DBS device still require medication which means that depending on their medication state, the patient may experience bradykinesia in off medication states (just waking up) or stimulation-induced dyskinesia after taking medication (Lozano et al., 2019). Adaptive stimulation, in which stimulation therapy is adjusted in response to electrophysiological biomarkers, has tremendous therapeutic potential, and has been recently made possible because of technological breakthroughs in the ability of the DBS probe targeting the STN or GPi to be 'bidirectional' which means it can both sense and stimulate (Gilron et al., 2021; Starr 2018). In order to best select which algorithms are best suited for adaptive DBS, it is helpful to understand what information the STN region is encoding. Our results suggest that the STN not only encodes the contralateral hand, but also the ipsilateral hand at a similar level. It will thus be important for future research to determine if the encoding we observe also has clinical relevance. It is possible that optimizing the adaptive DBS device based on symptoms based on both sides of the body could outperform algorithms that focus solely on the contralateral side. The results of a previous study hint that our encoding results may be clinically relevant, they found that unilateral DBS can affect symptoms on the ipsilateral side of the body, although to a lesser extent compared to the contralateral side (Walker, Watts, Guthrie, Wang & Guthrie, 2009). Further studies could examine if the STN also exhibits bilateral encoding of upper arm movements or foot movements in addition to the bilateral encoding we observe in hand movements.

Our result that the STN may be more context dependent than SMC may also be worth consideration for an adaptive device as the biomarkers for inhibited or slow moments for one hand may look different if both hands were engaged with the task. It would be easy to first classify movements as unimanual contralateral, unimanual ipsilateral or bimanual and have the algorithm operate based on particular biomarkers based on those states. We hope that basic research can add to the optimization of adaptive stimulation paradigms to the benefit of patients receiving care.

Chapter 3

kTMP: A New Subthreshold, High E-field, Frequency Specific, Non-Invasive Magnetic Stimulation Device to Modulate Cortical Excitability.

3.1 Abstract

We have developed a new non-invasive brain stimulation system, kilohertz transcranial magnetic perturbation (kTMP). A prototype kTMP device was constructed that can produce subthreshold modulations of neural activity with a cortical E-field magnitude of up to 7.6 V/m at 5 kHz. Amplitude modulation of the kilohertz carrier frequency kTMP waveform (AM-kTMP) can be used to provide stimulation at beat frequencies corresponding to endogenous neural rhythms (e.g., alpha, beta). In preliminary tests, we used TMS protocols to probe changes in corticospinal excitability following 10 min of kTMP stimulation. In Experiment 1, we manipulated the frequency of the non-modulated kTMP E-field, comparing the effects of a 2 V/m kTMP E-field delivered at 2 kHz, 3.5 kHz, and 5.0 kHz versus sham stimulation. Motor evoked potentials were significantly enhanced following kTMP, for at least 25 minutes, with the effect most marked for the 3.5 kHz condition. In Experiment 2, we repeated the sham and 3.5 kHz conditions, and included two AM-kTMP conditions, one in which the modulation was at 20 Hz and the other in which it was at 140 Hz. Again, the targeted E-field was fixed at 2 V/m. We replicated the increase in cortical excitability for the 3.5 kHz non-modulated condition. Most striking, we observed further enhancement of the MEPs in the 20 Hz AM-kTMP condition. Moreover, the only percept associated with kTMP at 2 V/m is a faint acoustic vibration from the amplifier, one that was easily blocked with standard foam earplugs, making kTMP suitable for double-blind experimentation. We conclude that kTMP has the potential to produce neural effects that mimic tES (e.g., continuous stimulation with frequency specificity) but at much higher E-fields in the brain.

3.2 Introduction

Non-invasive brain stimulation (NIBS) is a group of methods which perturb brain function by coupling an applied electric field (E-field) to the tissue of the brain without the need to introduce electrodes into the head or brain. The applied E-field may directly couple to the neuronal transmembrane potential or it may indirectly influence the transmembrane potential through changes to membrane properties. NIBS can safely manipulate neural excitability in the human brain, providing neuroscientists with a powerful tool to advance our understanding of brain function and clinicians with novel interventions in the treatment of neurological and psychiatric disorders. By altering the state of targeted brain areas and networks, NIBS methods can be used to test functional hypotheses, building on the experimental logic that has motivated generations of lesion and invasive stimulation studies in humans and other species. Indeed, NIBS interventions

are commonly used to disrupt behavior and also enhance performance in a broad range of cognitive domains(Cantarero et al., 2015; Conson et al., 2015; Flöel et al., 2008; Galea et al., 2011; Giglia et al., 2014; Heimrath et al., 2015; Javadi et al., 2017; Meinzer et al., 2014; Nevler and Ash, 2015; Reis et al., 2009; Richmond et al., 2014; Roy et al., 2015; Rufener et al., 2016; Wöstmann et al., 2018). Evidence that NIBS can promote brain plasticity has prompted clinicians to pursue NIBS interventions in the treatment of psychiatric (Fitzgerald 2020) and neurologic disorders (reviewed in (Ovadia-Caro et al. 2019; Iglesias 2020; Lefaucheur et al. 2020)).

The E-field induced by NIBS can be categorized as subthreshold or suprathreshold, according to the magnitude of the applied E-field. Suprathreshold fields are of sufficient amplitude to elicit immediate action potentials in targeted neurons. Subthreshold E-fields are insufficient to directly cause action potentials but may alter the state of the targeted neurons (Huang et al. 2017) on time scales ranging from immediate entrainment effects to plasticity effects lasting at least minutes. Whether interactions are enhanced or diminished depends upon the temporal characteristics of the E-field (waveform and duration) and its spatial characteristics such as local amplitude and direction (Peterchev et al. 2012).

The NIBS E-field is generated by a current source external to the head. Two broad categories of NIBS methods exist: Electrical contact methods (EC) and magnetic induction methods (MI). EC methods such as tES (transcranial electric stimulation) establish a cortical E-field via electrodes, driven by a current source, in electrical contact with the scalp. In tES, the current is either constant as in transcranial direct current stimulation (tDCS) or time-varying as in transcranial alternating current stimulation (tACS). MI methods, such as TMS (transcranial magnetic stimulation), establish a cortical E-field via a current-carrying coil that is positioned near the scalp, generating a time-varying magnetic field and consequently an induced cortical E-field.

The E-fields of the EC and MI methods differ in important ways as has been elucidated with the spherical head model(Sheltraw et al. 2021). First, the head E-fields of EC and MI NIBS methods exist in orthogonal subspaces of the space of all possible head E-fields. Even though the vector E-field of the EC and MI methods can never be identical they can, however, be similar with respect to focality on the cortical surface. Second, for spatiotemporally similar cortical E-fields the ratio of EC-to-MI root-mean-square (RMS) scalp E-field increases as the cortical focality increases. This ratio asymptotically reaches a limiting value of approximately 17.8 for typical human head three-shell models (Sheltraw et al. 2021). Third, in the low frequency “physiologic” range (0-200 Hz) the energetic cost for a current source to generate electric fields of appreciable magnitude within the brain region are much higher for MI as compared to EC methods (Sheltraw et al. 2021). In the kHz frequency range, however, MI methods become energetically practical. Fourth, the E-field amplitude of MI methods is linearly proportional to the frequency of the current supplied to the induction coil whereas the E-field of EC methods is independent of the frequency of the current supplied to the electrodes.

Even though the EC- and MI-NIBS methods can have similar focality and amplitude on the cortical surface, the scalp E-field amplitude ultimately places much greater restrictions upon the focality and amplitude of EC cortical E-fields. Recent estimates of the EC cortical E-fields in the physiological frequency range suggest that the maximum for most human participants is 0.5 V/m before scalp sensory stimulation becomes intolerable (Vöröslakos et al., 2018)(Huang et al. 2018). Since the RMS cortical E-field for MI can be as much as 17.8 times greater than that of EC methods with the same RMS scalp E-field, and since increasing cortical focality increases the scalp E-field amplitude for either method (Sheltraw et al. 2021), MI systems are far less burdened by constraints imposed by the scalp E-field amplitude. Practically speaking, this also allows for more focal MI E-fields compared to EC E-fields since increasing cortical focality increases the scalp E-field amplitude (Sheltraw et al. 2021).

In addition to the limitations imposed by the properties of the EC and MI E-fields, there may be limitations due to the electrodes commonly used in extant EC methods (tDCS and tACS) and coils used in extant MI methods (TMS). The electrodes and coils may be limited in number and size and this will have practical consequences for the spatial and temporal characteristics of the E-field so produced. In addition, the respective current sources of extant methods restrict the types and amplitudes of E-field waveforms that can be applied. This is particularly the case for TMS, where pulsed E-fields are used. Pulsed E-fields are also used for extant electroconvulsive therapy (an EC method) but this method is considered invasive in that the patient or human participant is administered general anesthesia and neuromuscular blocking agents as well mechanically ventilated while the EC current is applied. The waveform differences of extant tES and TMS methods are responsible for differences with respect to time-frequency localization of the perturbing E-field. Recall that according to basic Fourier transform properties a waveform which is localized in temporal space must, by mathematical necessity, be non-localized in frequency space and vice versa. Since extant TMS methods generate brief E-field pulses they are therefore broad in frequency space. In contrast, extant tES NIBS methods (this excludes electroconvulsive methods) generate waveforms that are broad in temporal space and are therefore localized in frequency space. As a result, extant tES methods are well suited to probe frequency-specific effects of the applied E-field whereas extant TMS methods are well suited to probe time-specific effects.

We have developed an innovative NIBS method, called Kilohertz Transcranial Magnetic Perturbation, or kTMP. The kTMP method uses magnetic induction to open a new NIBS experimental space characterized by relatively high amplitude cortical E-fields, but with the spatial focality of TMS and the frequency localization associated with tES, albeit in the kilohertz range. kTMP can be delivered in a continuous mode (Non Modulated kTMP) or in a amplitude modulation of the kilohertz carrier frequency (AM-kTMP) can be used to obtain beat frequencies which can potentially mimic perturbation in the physiologic frequency range corresponding to endogenous neural rhythms (e.g., alpha, beta) (SEE FIG X). In summary the greater E-field amplitudes, compared to tES, combined with the capability of kTMP to mimic endogenous frequencies via amplitude-modulated waveforms, put kTMP in a potentially transformative exploration of subthreshold NIBS.

To facilitate efficacy testing, the same TMS coil can be driven sequentially between kTMP and standard suprathreshold TMS operation, thus permitting a convenient suprathreshold probe of the changes in neuronal excitability induced by kTMP. MEPs elicited with TMS in the M1 motor cortex region provide an index of corticospinal excitability and is widely recognized as the gold standard for assessing the effects of NIBS induced changes (Nitsche and Paulus 2000, 2001; Nitsche et al. 2003; Huang et al. 2005).

The effects of narrow-band kHz E-fields on peripheral nerves and the central nervous system of animal models has been studied using EC methods almost exclusively. A particularly good review of the robust results that have been achieved has recently been published (for a review see Neudorfer et al., 2021). Suprathreshold EC methods have been shown to produce robust electrical conduction blocking in peripheral nerves (Bhadra et al. 2018) (Esmaeilpour et al. 2021) and targeted deep stimulation of motor cortex through temporal interference effects in mice (Grossman et al. 2017). Recent converging evidence suggests that subthreshold kHz fields also play an important NIBS role, mainly derived from auditory nerve stimulation studies (for a review see Neudorfer et al., 2021). Moreover, tACS at kHz frequencies can induce changes in neural excitability approximately equal to those seen with standard, low frequency tES (Chaieb et al. 2011, 2014). Low frequency magnetic stimulation (LFMS), mimicking the magnetic field waveforms used in MRI, is another kHz method producing weak E-fields across the entire brain, and has been reported to have mood-altering effects (Rohan et al. 2014; Wang et al. 2018). In addition, kHz E-fields, again applied by MRI gradients, have been shown to alter brain glucose metabolism in a manner that scales with the field amplitude (Volkow et al. 2010).

In two experiments we investigating the effects of subthreshold kTMP cortical E-fields of approximately 2.0 V/m amplitude on the corticospinal excitability of humans. Such amplitudes are a 4-fold increase over that obtainable with extant tES methods. In Experiment 1, non-amplitude modulated kTMP at three different frequencies (2 kHz, 3.5 kHz and 5 kHz) were compared to a sham condition (0.01 V/m, 3.5 kHz). In experiment 2 we set the carrier frequency at 3.5 kHz and used amplitude modulation (AM-kTMP) to create beat frequencies of 20 Hz (Feurra et al. 2011, 2013; Heise et al. 2016) and 140 Hz (Inukai et al. 2016; Dissanayaka et al. 2017). These conditions were compared with two non-modulated kTMP conditions at 3.5 kHz and the other 0.01 V/m (sham). To explore the origin of kTMP modulation in detail, we measured MEPs changes pre-post kTMP using both Single Pulse and Paired Pulse Protocols (Intracortical inhibition and facilitation).

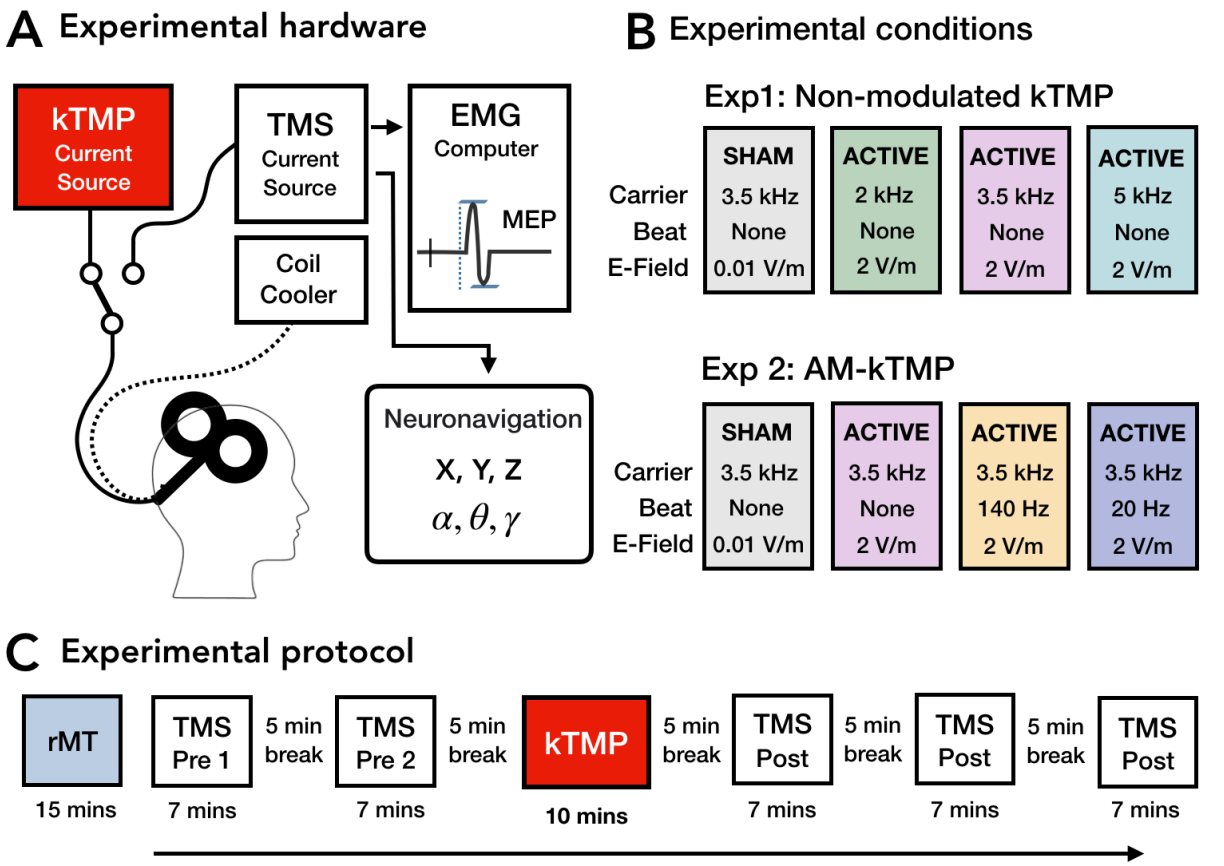

Figure 3.1. Experimental setup and protocol. A. Experimental hardware. The experimental hardware consists of five components: The suprathreshold TMS current source, subthreshold kTMP current source, a figure-eight Coil (Cool-B65), electromyography (EMG) recorder and neuronavigation system (BrainSight). The TMS coil can be driven by either the kTMP unit or a commercially available TMS unit thereby ensuring the identical E-field distribution. Each TMS pulse was registered in real time in both the EMG system and the neuronavigation system allowing us to record MEP amplitude along with the six-dimensional spatial position and orientation of the coil with respect to the hotspot. **B. Experimental conditions.** We tested four kTMP experimental conditions in each experiment. In experiment 1 we varied the carrier frequency and in experiment 2 we varied the beat frequency of the amplitude modulated waveform, holding cortical E-Field constant. Sham and non-modulated kTMP at 3.5 kHz were also included in experiment 2 to serve as comparison. **C. Experimental protocol.** At the beginning of each session the participant's hotspot and rMT was found, followed by two pre-TMS blocks, ten minutes of kTMP stimulation and three post-TMS blocks. Each block consisted of 90 TMS pulses (30 = signal pulse, 30 = SICI, 30 = ICF) separated by a 4 or 5 second inter-pulse interval.

3.3 Method

Experimental Hardware. The experimental hardware consists of five components: The suprathreshold TMS current source, subthreshold kTMP current source, a figure-eight Coil (Cool-B65), electromyography (EMG) recorder and neuronavigation system (Brainsight Rogue Research Inc; Fig. 2A). The TMS coil can be driven by either the kTMP unit or a commercially available TMS unit (MagVenture R30 stimulator) thereby ensuring the identical E-field distribution, up to an amplitude scaling factor, for the TMS and kTMP.

kTMP device. The kTMP device consists of a TMS coil, a high-amplitude current source and a control system. The coil is the same coil as used for the TMS system. This assures that the electric field distributions of the TMS and kTMP stimulus are the same up to a multiplicative amplitude factor. The control system consists of a personal computer (PC), input/output PCI card, and the built-in coil temperature sensor (access to the sensor electronics was modified for our application). The PC controls the PCI card using the MatLab Data Acquisition ToolBox which delivers analog output to the amplifier and receives analog input from the temperature sensor. The coil temperature is monitored to assure participant safety. Automatic shutdown was set to occur if the temperature exceeded 48 degrees Celsius (according to International Electrotechnical Commission standards) however it never rose above 32 degrees Celsius during system operation. The PCI card delivers an analog voltage signal, which specifies the temporal waveform of the E-field, to the input of the amplifier (AE Techron model 7794). The amplifier behaves as a current source which delivers a user-specified current amplitude to the TMS coil. The method of Nieminen (Nieminen et al. 2015) was used to measure the effective E-field amplitude in a spherical phantom as a standard. The current amplitude was selected to achieve a 2.0 V/m E-field amplitude for a given frequency at a distance of 14 mm perpendicular to the coil surface, typical of the skin-to-cortex depth in our participant group(Lu et al. 2019). The relationship between the current amplitude (I), frequency (f) and E-field amplitude (E) at 14 mm was established to be $E = 7.875 \times 10^{-6}$ (Vs/Am) f I (EQ. 1).

The UC Berkeley IRB approved the kTMP system as a non-significant risk device to a maximum E-field to 8 V/m. Given the novelty of the kTMP system, we have worked closely with the IRB and Environment, Health & Safety (EH&S) Committee at UC Berkeley from the early stages of project development.

TMS device and coil. The TMS unit consists of a passively liquid-cooled TMS coil (MagVenture Cool B-65) and capacitive power source (MagVenture MagPro x100 TMS stimulator). The figure eight coil has an inner diameter of 35 mm and an outer diameter of 75 mm. Suprathreshold biphasic pulses are used to titrate the motor threshold pre and post kTMP application.

EMG device. The Bagnoli-8 EMG System (Delsys Inc.) was integrated with the kTMP-TMS system to measure the amplitude of MEPs elicited with single-pulse suprathreshold TMS in assessing the efficacy of kTMP. The TMS device sends a signal to the EMG recorder to mark the time of a suprathreshold stimulus within the continuously acquired EMG data.

Neuronavigation. BrainSight NeuroNavigation system was used to mark the M1 hotspot on each participant's scalp. This allowed the experimenter to return to the same position between TMS blocks during the application of kTMP. In addition, we have developed a system to read and record the six-dimensional spatial and angular position of the coil with respect to the hotspot in real time, allowing us to record this information at the time of each TMS pulse. This information was used to exclude trials in which the coil was distant from the hotspot or the angle had changed from the optimal hotspot orientation.

Participants. 36 colleges student's adults participated in the two experiments (Experiment 1: n =20: 13 female and 7 male; Experiment 2: n = 16: 10 female and 6 male; 7 were run in both experiments). All participants were naive to the purpose of the study and were financially compensated, with written consent obtained before the start of the experiment.

Experimental design and statistical Analysis

Procedure. To evaluate the kTMP system as a new tool to modulate neuronal excitability, we measured the impact of kTMP on corticospinal excitability using suprathreshold TMS stimulation over motor cortex. An overview of the experimental protocol is depicted in Figure 3.1C. Participants started with an introduction session, where the procedure of the experiment was explained and Single Pulse TMS was applied to identify the optimal scalp position over left M1 (hotspot) for eliciting motor evoked potentials (MEP) in the right index finger. The hotspot was registered in three-dimensional space using a neuro-navigation system (Brainsight, Rogue Resolutions Ltd., Cardiff, UK) to ensure consistent coil position throughout and between the different sessions. For ease of experimentation, the TMS coil can be driven by either the kTMP unit or a commercially available TMS unit without altering its position relative to the head.

After the introduction session, participants were tested over four 2-hour sessions, with an interval between sessions of at least of two days. To assay the efficacy of kTMP we measured the change in MEP amplitude before and after the active or sham kTMP stimulation conditions. In experiment 1 participants were unaware of the experimental conditions; In Experiment 2 a double-blind procedure was employed in which neither the participant nor experimenter were aware of the stimulation condition.

Transcranial magnetic stimulation (TMS). Single-pulse TMS was applied over left hemisphere M1 to determine the resting motor threshold (rMT) for the first dorsal interosseous muscle (FDI) in the right hand, the agonist for abduction movement with the index finger. FDI is relatively easy to isolate in all individuals and threshold values are very stable across test sessions (e.g., Carroll et al. 2001; Kamen 2004; Malcolm et al. 2006). The TMS coil was placed tangentially on the scalp with the handle pointing backward and laterally at a 45^0 angle from the midline. The position was adjusted to identify the optimal scalp position over left M1 for eliciting motor evoked potentials (MEP) in the right index finger for each session. MEPs were measured by a surface electrode attached to the hand to record EMG signals from the right FDI, with a reference electrode over right elbow. The EMG signals were amplified and bandpass filtered on-line between 20 and 450 Hz (Delsys Inc.). The signals were digitized at 2000 Hz for off-line analysis. EMG data were collected for 5 seconds on each trial, starting 200 msec before the TMS pulse. The experimenter visually monitored the EMG traces on a separate monitor to ensure that the participant remained relaxed

(i.e., negligible EMG background activity in FDI) and to detect the presence or absence of MEPs in response to the TMS pulses. The coil was positioned on the scalp to identify a location that produced robust MEPs in a consistent manner. Once identified, this location was marked on Brainsight to ensure stability during the threshold procedure and as a reference point for the experimental sessions. For the thresholding procedure, the stimulator intensity was initially set to 30% of maximal stimulator output (MSO). The intensity was adjusted to determine the rMT, defined as the level required to evoke MEPs of at least 50 μV peak-to-peak amplitude in the relaxed FDI, on 5 of 10 consecutive trials.

To assay the efficacy of kTMP we measured changes in motor-evoked potentials (MEPs) before and after kTMP with single and paired-pulse TMS assays. Each assessment block (two TMS pre-kTMP and three TMS post-kTMP) included single pulse TMS (SP), and two paired-pulse protocols: short intracortical inhibition (SICI), and intracortical facilitation (ICF) where a sub-threshold conditioning stimulus (at the 80% of rMT CS) was followed by a testing Stimulus (TS) with an interstimulus interval (ISI) of 1ms and 10ms respectively. All three measures have been widely used in prior studies designed to evaluate the efficacy of tES and rTMS methods in altering neural excitability(Horvath et al. 2015; Chung et al. 2016; Biabani, Aminitehrani, et al. 2018). We collected data from 30 trials for each measure per block to ensure reliable results (Chung et al. 2016; Goldsworthy et al. 2016; Cavaleri et al. 2017; Biabani, Farrell, et al. 2018).

kTMP stimulation.

Experiment 1. Non amplitude Modulated kTMP. Participants were tested over four sessions, three with active kTMP stimulation and one with sham kTMP stimulation (Fig. 3.1B, with the coil always positioned to target primary motor cortex. For the active kTMP sessions, we used three different frequencies, 2 kHz, 3.5 kHz and 5 kHz, changing the intensity of stimulation to produce a 2 V/m E-field at the cortical surface. kTMP E-field amplitude adjustments based on scalp-to-cortex distance were not made in the experiments. For the sham condition, we used a 3.5 kHz signal but induced a 0.01 V/m E-field by setting the intensity to a very low voltage (0.12 V).

Experiment 2. Amplitude Modulation kTMP (AM kTMP). Participants were tested over four sessions, three with active kTMP stimulation and one with sham kTMP stimulation conditions (Fig. 2B). In two of active kTMP conditions we set the carrier frequency at 3.5 kHz and used amplitude modulation to create beat frequencies of 20 Hz and 140 Hz. The 3.5 kHz carrier frequency was chosen since our first pilot showed the largest effect at this frequency; we selected beat frequencies of 20 Hz and 140 Hz, choosing 20 Hz given the relevance of beta to motor function (Feurra et al. 2011, 2013; Heise et al. 2016) and 140 Hz based on literature concerning ripple effects at this frequency (Inukai et al. 2016; Dissanayaka et al. 2017). We also included two non-modulated kTMP conditions with a 3.5 kHz input signal, one set to produce a cortical E-field of 2 V/m (active) and the other 0.01 V/m (sham). These two conditions provide a replication of two of the key conditions in Experiment 1 with non-modulated and serve as a point of comparison for the two AM kTMP conditions. The parameters for the AM conditions were set to produce a 2 V/m E-field at the cortical surface, matched to the non-modulated active condition.

Stimulation Sensation. Participants wore earplugs during the TMS and kTMP experimental sessions. Observations from the research team and the participants in Experiment 1 confirmed that the coil did not produce any perceptible scalp sensations during kTMP stimulation. A low-intensity sound (pure tone at stimulation frequency) emanating from the amplifier could be heard by the researcher during all the active kTMP conditions (although not by the older members of the research team who likely have some mid-frequency hearing loss). In Experiment 2 also the research team wear earplugs to assure double blinding. Moreover, we administered a short survey after the first TMS assessment block (baseline phase) and at the end of the kTMP stimulation to obtain ratings (10-point Likert scale, 1 = not at all; 10 = extremely) on comfort and sound (Meteyard and Holmes 2018).

Data analysis. All EMG measures were analyzed with custom scripts written in Matlab 2018a. Continuous EMG activity was recorded and epoched based on a TTL pulse that was sent from the TMS system at the time of each TMS pulse and recorded in the EMG amplifier as an auxiliary channel. After the data were epoched the following steps were used to clean the data. 1) Mean and standard deviation were calculated for each TMS protocol type (single pulse, ICF, ICI), if a given trial had a peak-to-peak MEP amplitude that was two standard deviations above or below the mean for that protocol the trial was considered an outlier and not included in further data analysis. 2) All trials that had a MEP amplitude below .05 mV were not included in further data analysis. 3) All trials that recorded the coil more than 3mm (Euclidian distance) from the optimal hotspot or had an angular or twist angle 3º from the optimal hotspot were also removed and not included in further analyses. For each TMS protocol we recorded 30 trials per block, after our cleaning procedure we retained at least 20 out of the 30 trials per block per participant.
After the data were cleaned, we found the average peak-to-peak amplitude of MEPs per TMS protocol for each block. We then transformed the data into a measure of percent change by subtracting and then dividing by the average of the pre blocks for each block post kTMP stimulation. This provided us with three time points post kTMP stimulation for each participant for each condition.

3.4 Results

kTMP Stimulation Sensation. A low-intensity sound (pure tone at stimulation frequency) emanating from the amplifier could be heard by most individuals (although not by the older members of the research team who likely have some mid-frequency hearing loss). As such, the participants and experimenter wore earplugs during the experimental sessions. Observations from the research team and the participants in Experiment 1 indicated that the sound was mostly blocked by the earplugs, but as an additional precaution, a recording of the pure tone in the 3.5 kHz condition was played during all kTMP sessions to minimize the likelihood that participants could tell active from sham conditions. The coil did not produce any perceptible scalp sensations during kTMP stimulation.

In experiment 2 we administered a short survey at the end of TMS and the kTMP stimulation to obtain ratings (7-point Likert scale, 1 = not at all; 7 = extremely) on comfort and sound. With just

a few exceptions, the participants' ratings were 1. Two gave a rating of 2 on "comfort", indicating that it became slightly uncomfortable given the long time they were required to remain still. Feedback from the participants confirmed that the coil did not produce any perceptible scalp sensations during kTMP stimulation. Although our method for assessing subjective experience in this pilot study was relatively crude, the results are very promising that kTMP can be easily modified to enable double-blind studies.

Changes in cortical excitability.

Non-Modulated kTMP. To assess the effect of non-modulated kTMP stimulation, peak to peak amplitude of MEPs elicited with TMS were measured pre- and post-kTMP stimulation. Average MEP amplitude for each block post- kTMP was transformed into a measure of percent change based on the average of the first two pre-kTMP blocks. Thus, a value of 0% would indicate no change in MEP amplitude from pre- to post- stimulation, whereas a value of 100% would indicate the MEP amplitude doubled from pre- to post- stimulation. Four conditions were tested including sham (frequency = 3.5 kHz, cortical E-field = .01 V/m), and three active conditions (2 kHz, 3.5 kHz and 5 kHz, cortical E-field = 2.0 V/m; Fig 2B). Three post stimulation blocks were administered, creating three time points post stimulation per participant per condition. Each stimulation block consisted of single pulse TMS, and two paired pulse protocols: short intracortical inhibition (SICI), and intracortical facilitation (ICF), measures that have been used previously to evaluate the efficacy of tES and rTMS (Horvath et al. 2015; Chung et al. 2016; Biabani & Aminitehrani et al. 2018). Each TMS protocol was analyzed separately. Although our design is within subjects, five of the 20 participants only completed three of the four experimental conditions due to technical issues with the Brainsight Neuronavigation system (n = 1) or university closures due to the COVID-19 pandemic (n = 4), creating missing values. To maximize the within subjects design and to account for missing data, we opted to use a mixed-effects model with fixed factors of stimulation frequency and time post stimulation.

Single Pulse: A mixed-effects model revealed a significant effect of stimulation frequency [χ^2 (3) = 10.841, p = 0.013], indicating that non-modulated kTMP affects single pulse MEP amplitude (Fig 3A). There was no effect of time post stimulation [χ^2 (2) = 1.433, p = 0.488] and there was no interaction between the two factors [χ^2 (6) = 8.415, p = 0.209]. Planned comparisons indicate that MEPs increased significantly after 3.5 kHz kTMP stimulation compared to sham [χ^2 (1) = 7.982, p = 0.005] as well as 2 kHz kTMP stimulation compared to sham [χ^2 (1) = 4.107, p = 0.0427; Fig 3A]. In contrast, there was no effect of 5 kHz stimulation compared to sham [χ^2 (1) = 3.186, p = 0.074].

SICI: We first tested if our SICI protocol significantly inhibited MEP amplitude compared to single pulse. We computed the ratio of SICI MEP amplitude to single pulse MEP amplitude and found the average across the first two pre blocks such that each session had one ratio measure. Because we only examined pre blocks, we could incorporate sessions across all four conditions. Using these values, we found that trials with the SICI protocol had significantly reduced MEP amplitude compared to the single pulse protocol [t (70) = -19.571, p < .001; Fig 6A]. We then examined how

the SICI protocol was affected by non-modulated kTMP. This required an extra step such that after computing the ratio for the SICI protocol, we then found the percent change from pre to post kTMP. For the SICI protocol, a mixed-effect model revealed that there was no effect of stimulation frequency [χ^2 (3) = 1.016, p = 0.797], no effect of time post stimulation [χ^2 (2) = 3.824, p = 0.148] and no interaction between the two factors [χ^2 (6) = 1.265 p = 0.974; Fig 6A].

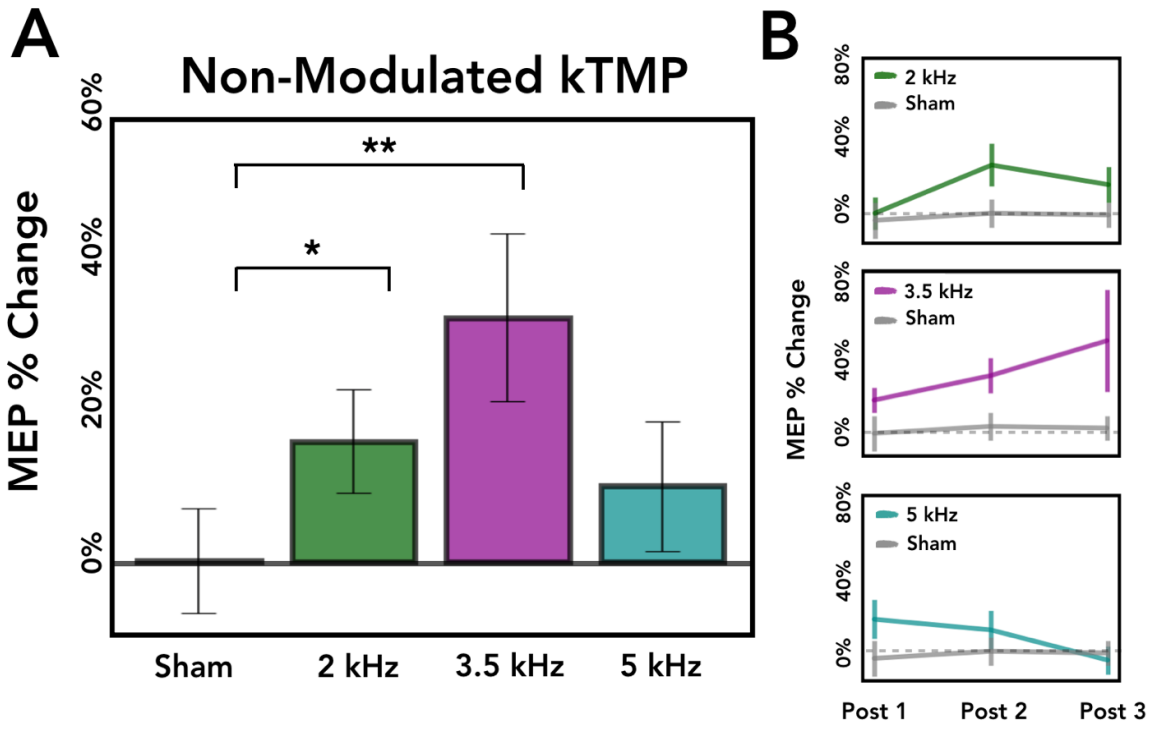

Figure 3.2. Non-Modulated kTMP increases corticospinal excitability. A. Average percent change across conditions. Percent change in MEP amplitude from pre to post kTMP stimulation across the four experimental conditions. Non-modulated kTMP at 2 kHz and 3.5 kHz was significantly different from sham stimulation. **B. Time course post kTMP.** Time course of MEP percent change across the three TMS blocks post stimulation. Time in-between each post TMS block is approximately 12 minutes. No main effect of time post stimulation was found.

ICF: Similar to SICI, we first tested if our ICF protocol significantly increased MEP amplitude compared to single pulse. We found that trials with the ICF protocol had significantly greater MEP amplitude compared to the single pulse protocol [t (70) = 5.141, p < .001; Fig 6B]. We then examined how the ICF protocol was affected by non-modulated kTMP using the same method as SICI. For the ICF protocol, a mixed-effect model revealed that there was no effect of stimulation frequency [χ^2 (3) = 4.473, p = 0.215], no effect of time post stimulation [χ^2 (2) = 1.332, p = 0.514] and no interaction between the two factors [χ^2 (6) = 2.009, p = 0.919; Fig 6B].

Amplitude Modulated kTMP (AM-kTMP): In the next experiment, we aimed to replicate two conditions from experiment 1: sham (frequency = 3.5 kHz, amplitude = .01 V/m) and the active

condition at 3.5 kHz with a 2 V/m E-field at the cortical surface. In addition, we added two new conditions consisting of kTMP with the carrier frequency of 3.5 kHz being amplitude modulated at either 20 Hz or 140 Hz using different intensities of stimulation to produce a 2 V/m E-field at the cortical surface. Similar to experiment 1, the majority of our participants (n = 13/16) completed all 4 conditions with a smaller subset (n = 3/16) only completing three of the four conditions due to technical issues with the Brainsight Neuronavigation system (n = 1) or university closures due to the 2020 pandemic (n = 2). Because of these missing values we again opted to use a mixed-effect model with fixed factors of stimulation frequency and time post stimulation.

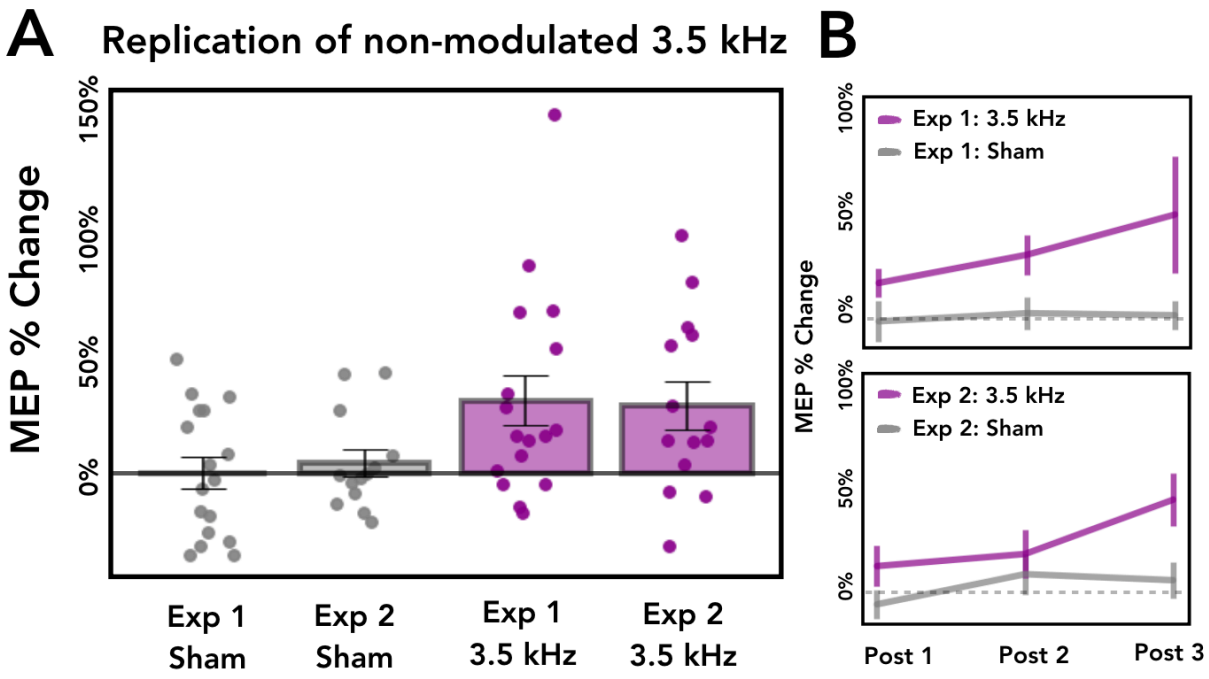

Figure 3.3. Replication of non-modulated 3.5 kHz kTMP. A. Average percent change for sham and 3.5 kHz. In experiment 2 we replicated two experimental conditions from experiment 1, the sham condition and non-modulated kTMP at 3.5 kHz. We show the results from the two studies side by side with each dot representing the average MEP percent change from pre to post for each participant. In both studies the 3.5 kHz condition had significantly larger MEP amplitude change from pre to post compared to sham. **B. Time course post kTMP.** Time course of MEP percent change across the three TMS blocks post stimulation blocks for both sham and 3.5 kHz conditions. No effect of time post stimulation was found in experiment 1 for the 3.5 kHz condition but an effect was found in for 3.5 kHz in experiment 2.

Single Pulse: A mixed-effect model revealed a significant effect of stimulation frequency [χ^2 (3) = 17.211, p < 0.001], a significant effect of time post stimulation [χ^2 (2) = 6.255, p = 0.044], but there was no interaction between the two factors [χ^2 (6) = 2.402, p = 0.879]. Planned comparisons of stimulation frequency indicate that MEPs increased significantly after AM modulated kTMP stimulation at 20 Hz [χ^2 (1) = 13.816, p < 0.001], 140 Hz [χ^2 (1) = 15.412, p < 0.001], and non-modulated 3.5 kHz [χ^2 (1) = 11.032, p < 0.001] compared to sham. This

replicates our finding from Experiment 1 that 3.5 kHz kTMP increases cortical excitability compared to sham (Fig 3.4). We also find that both the AM kTMP conditions increase cortical excitability compared to sham (Fig 3.5A). In fact, MEP amplitude in the 20 Hz AM condition was significantly greater than non-modulated kTMP at 3.5 kHz [χ^2 (1) = 6.503, p = 0.011], suggesting that AM kTMP may have a stronger effect on cortical excitability compared to non-modulated kTMP at some AM frequencies. No other differences were found between the other active conditions [all χ^2's < 2.146, all p's > 0.143].

We also examined the effect of time post stimulation for each condition and found that MEP amplitude increased across time for 3.5 kHz [χ^2 (2) = 16.329, p < .001] and 140 AM [χ^2 (2) = 8.763, p = 0.013] whereas no effect was found for sham [χ^2 (2) = 3.758, p = 0.153] or for 20 AM [χ^2 (2) = 1.679, p = 0.432; Fig 3.5B].

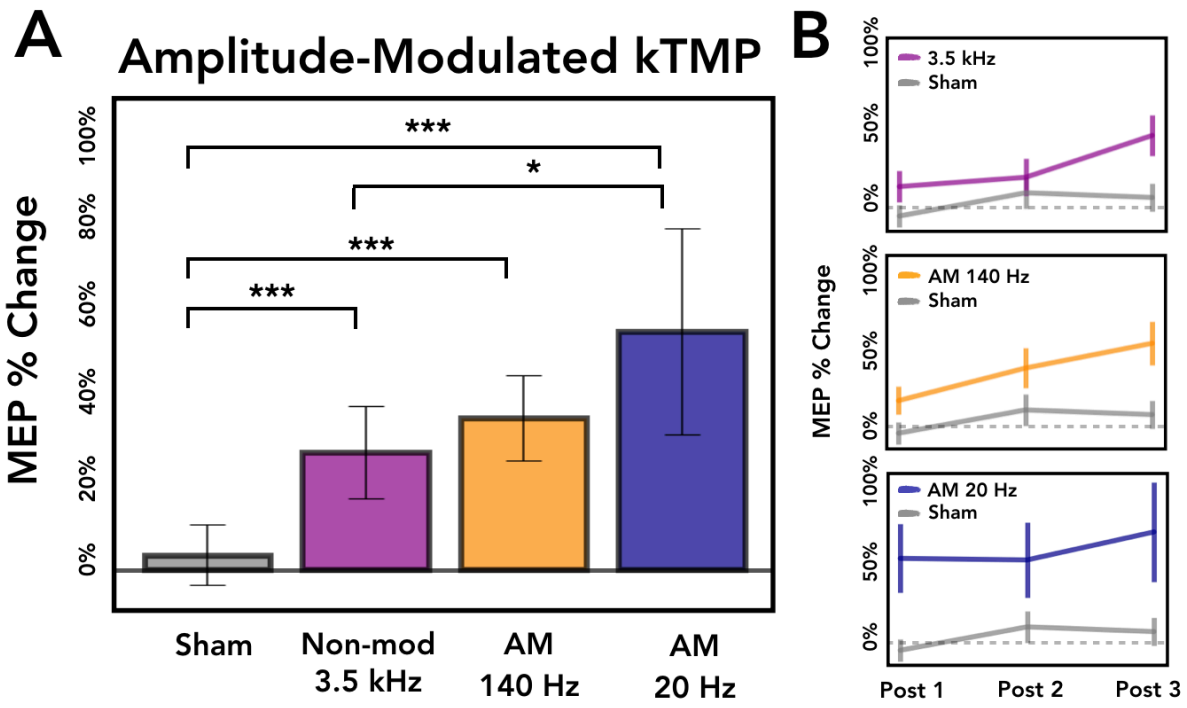

Figure 3.4. Amplitude-Modulated kTMP increases corticospinal excitability. A. Average percent change across conditions. Percent change in MEP amplitude from pre to post kTMP stimulation across the four experimental conditions. An increase in MEP amplitude was found for all three of our experimental conditions compared to sham. In addition, AM-kTMP at 20 Hz increased MEPs significantly above that for non-modulated 3.5 kHz, suggesting AM kTMP stimulation at some AM frequencies may be more effective than non-modulated kTMP. **B. Time course post kTMP.** Time course of MEP percent change across the three TMS blocks post kTMP stimulation. Time in-between each post TMS block is approximately 12 minutes. An effect of time post stimulation was found with non-modulated 3.5 kHz and AM 140 Hz increasing significantly across time; no effect of time was found for sham or AM 20 Hz.

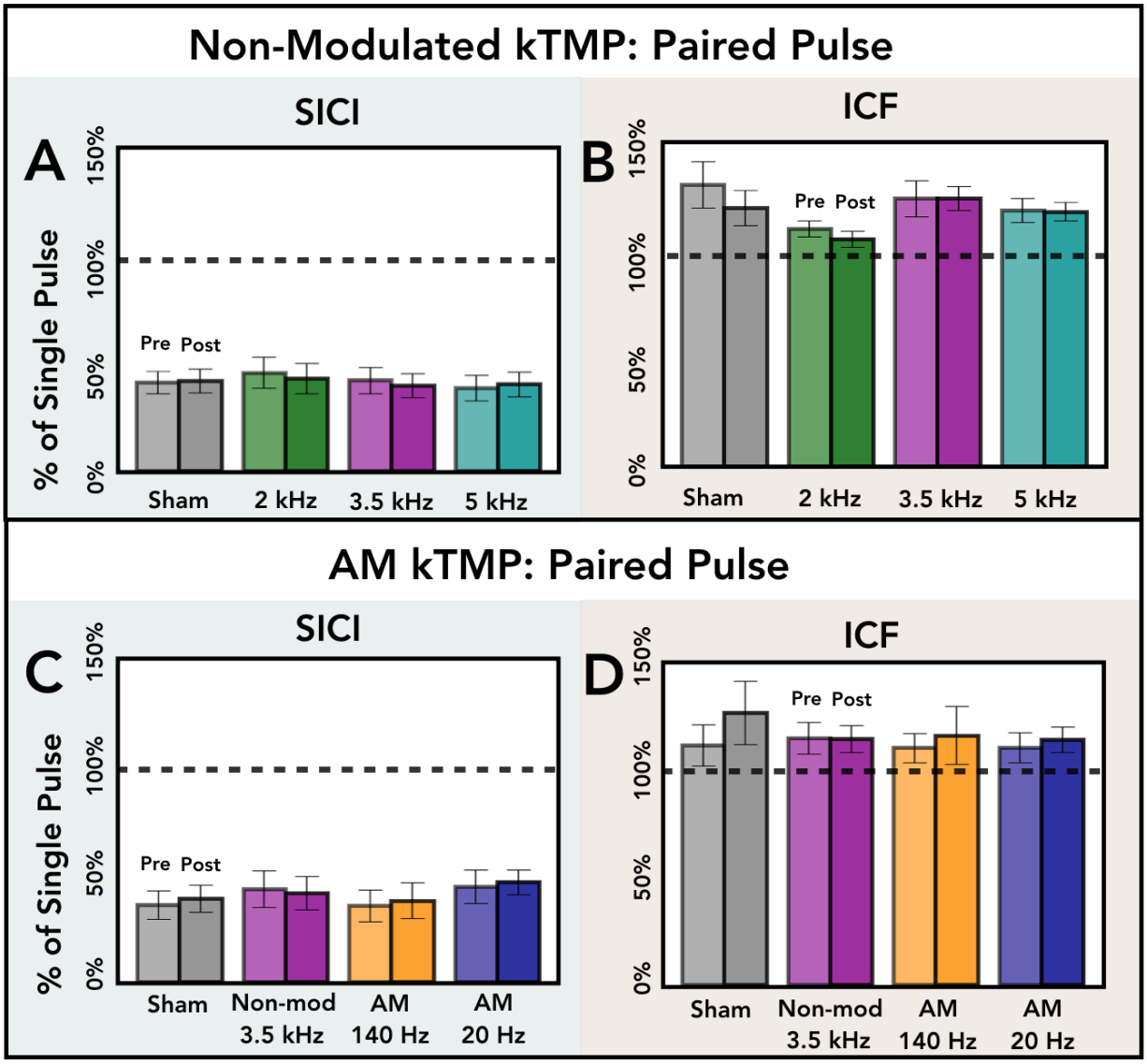

Figure 3.5. No effect of non-modulated- or AM-kTMP for paired pulse protocols. A. SICI protocol for non-modulated kTMP. A substantial inhibitory effect of our SICI protocol was found compared to single pulse, but non-modulated kTMP did not have an effect on the amount of inhibition elicited. B. ICF protocol for non-modulated kTMP. A faciliatory effect of our ICF protocol was found compared to single pulse, but non-modulated kTMP did not have an effect on the amount of faciliatory elicited. C. SICI protocol or AM-kTMP. In experiment 2 we again saw a substantial inhibitory effect for the SICI protocol compared to single pulse, but AM-kTMP did not have an effect on the amount of inhibition elicited. D. ICF protocol for AM-kTMP. Same as C except for the faciliatory protocol.

SICI: We first tested if our SICI protocol significantly inhibited MEP amplitude compared to single pulse. We found that trials with the SICI protocol had significantly reduced MEP amplitude compared to the single pulse protocol [t (60) = -16.576, p < .001; Fig 6C]. We then examined how

the SICI protocol was affected by non-modulated kTMP. This required an extra step such that after computing the ratio for the SICI protocol, we then found the percent change from pre to post kTMP. For the SICI protocol, a mixed-effect model revealed that there was no effect of stimulation frequency [χ^2 (3) = 1.614, p = 0.656], no effect of time post stimulation [χ^2 (2) = 0.503, p = 0.778] and no interaction between the two factors [χ^2 (6) = 5.028 p = 0.540; Fig 6C].

ICF: We first tested if our ICF protocol significantly increased MEP amplitude compared to single pulse. We found that trials with the ICF protocol had significantly greater MEP amplitude compared to the single pulse protocol [t (60) = 2.976, p = .004; Fig 6D]. We then examined how the ICF protocol was affected by non-modulated kTMP using the same method as SICI. For the ICF protocol, a mixed-effect model revealed that there was no effect of stimulation frequency [χ^2 (3) = 4.053, p = 0.256], no effect of time post stimulation [χ^2 (2) = 0.148, p = 0.929] and no interaction between the two factors [χ^2 (6) = 5.627, p = 0.466; Fig 6D].

3.6 Discussion

kTMP is a new method for subthreshold non-invasive brain stimulation with greater E-field amplitudes, compared to tES, and with the capability of mimic endogenous frequencies via amplitude-modulated waveforms. Non-modulated kTMP increased corticospinal excitability in a frequency specify manner, at 2 kHz and 3.5 kHz frequencies. In experiment 2 we replicated our finding that non-modulated kTMP at 3.5 kHz increases corticospinal excitability and also tested two amplitude-modulated kTMP conditions at 20 Hz and 140 Hz with a carrier frequency of 3.5 kHz. We found that both AM-kTMP conditions also increase corticospinal excitability relative to sham, and that the 20 Hz AM condition increased MEP amplitude above and beyond the non-modulated 3.5 kHz effect, suggesting that AM-kTMP may be more effective than non-modulated kTMP.

Results have shown a selective influence of kTMP on single pulse but not on intracortical excitability measured with Paired Pulse protocols. Single pulse MEP amplitude is a measure of cortico-spinal excitability and resemble excitability of intrinsic primary motor cortical neurons. Intracortical inhibition and facilitation, which resemble cortico-cortical excitability, depend on stimulation of motor cortical afferents (for a review on circuits involved in NIBS see Di Lazzaro et al, 2018). kTMP is a magnetic method and so the induced tangential current flows parallel to the brain surface activating elements that are aligned horizontally having synapses onto the corticospinal neurons, influencing I-waves. Our results seem indicate that the kTMP effect is predominant on the early, low threshold, volley I-waves (I1) responsible of MEPs change in Single Pulse protocols but not the late I-waves that originate from different sources of inputs to corticospinal cells. These reflect projections to corticospinal cells for I1-waves, and a more complex circuit composed of both excitatory and inhibitory neurons for the later I-waves.

Although changes in MEPs are the gold standard for evaluating NIBS methods, MEP-based measures are quite variable (Campana et al., 2019; Darling et al., 2006; Hashemirad et al., 2017). The variability likely has multiple sources, many of which we cannot control (e.g., internal

fluctuations in cortical excitability). One source arises from fluctuations in the placement and orientation of the TMS coil on the "hotspot", the location over motor cortex that reliably elicits MEPs. The magnitude of coil placement effects will vary across individuals given that the stimulation is applied at a fixed electrical current amplitude, without consideration of variables that influence the magnitude of the E-field at the level of the cortex. The magnitude of the cortical E-field is inversely related to the distance from the coil, which is placed against the scalp, and this distance exhibits considerable variation between individuals (Opitz et al. 2015). The intervening tissue is not homogenous, but composed of five primary layers: skin, two layers of cortical skull, trabecular skull, and CSF, each with their own conductive properties (Truong et al. 2012) and thickness, adding additional sources of individual variation. Similarly, given that a stimulation method disproportionately affects certain types of neurons, individual geometric variations in those neurons and/or their associated neurotransmitters would influence the efficacy of the procedure (Ridding and Ziemann 2010; Stagg et al. 2011).

We now turn to a mechanism for kTMP. There are some concerns in the electrophysiology literature about the effectiveness of kHz NIBS E-fields, given that neurons behave as low-pass filters. If the concern is that the membrane time constant, equal to the product of the membrane resistance and capacitance, is too large to allow high frequency (short time-scale) components of the NIBS electric field (the input) to influence the transmembrane potential (the output), passing only frequencies below cell-dependent cutoff frequencies. Furthermore, it is assumed that if the neuron cannot pass kHz frequencies then it is not possible for such frequencies to have effects upon neurons or neuronal networks. This assertion arises from modeling of the neuron as a passive electrical system – one in which the membrane resistance is a fixed value throughout the dynamical behavior of the system and can consequently be described with the mathematics of linear time-invariant (LTI) systems. However, the LTI model has very limited and well circumscribed applicability. The LTI passive neuron model holds to good approximation only when the transmembrane potential is near its resting value. If the transmembrane potential departs significantly from the resting value then the neuron must be modeled as an active electrical system which, by virtue of voltage dependent membrane resistance, is described by nonlinear models such as those developed by Hodgkin-Huxley (Hodgkin and Huxley 1952). Neudorfer et al., (2021) have recently published a detailed review showing robust empirical evidence supporting the use of sub- and suprathreshold kHz E-fields in NIBS research, indicating that the dominant effect of subthreshold kilohertz-frequency stimulation on neural tissue subthreshold is facilitation.
Here, we suggest three mechanisms by which subthreshold kHz E-fields, with and without amplitude modulation, may potentially influence neuronal behavior:

Effective Time Constant Dynamics. During subthreshold dynamics of the membrane potential the sodium ion membrane conductance (the primary determinant of subthreshold dynamics) can increase by two orders of magnitude(Hodgkin and Huxley 1952) as it nears threshold, thereby effectively decreasing the membrane time constant by the same factor for some interval of time. During such intervals, the effective time constant would permit short time-scale (high frequency) signals to influence the transmembrane potential. For example, the cutoff frequency for the passive membrane of pyramidal cells is approximately 20 Hz (Moradi Chameh et al. 2021). When near threshold the effective 3dB cutoff frequency would therefore be approximately 2000 Hz. The

passive membrane time constant varies significantly between different neurons and glial cells. Glial cells are regulators of neuronal intracellular calcium which plays an important role in ion channel conductance and is a potential regulator of plasticity effects.

Frequency Intermodulation. Nonlinear systems produce intermodulation of the input frequencies thereby producing output frequencies which are sums and differences of integer multiples of the input frequencies. If an amplitude modulated signal, such as the one used in this work, is created by the superposition of two kHz signals of difference Δf then intermodulation can produce actual frequency components at Δf (along with harmonics) which may be in the physiologic frequency range (0-200 Hz). Subthreshold intermodulation effects have been studied in the FitzHugh-Nagumo neuron (Si et al. 2009) (X demonstrating the significance of intermodulated components of the applied field.

Demodulation of Amplitude Modulated Signals. Under suitable conditions an amplitude modulated signal may be demodulated to produce the component frequencies of its modulation envelope. This may occur when a system displays a rectification step followed by a low-pass filter step. Some gap junctions (electrical synapses) of the mammalian brain are current rectifiers satisfying the first criteria for demodulation. If the post synaptic membrane is near resting state then it will act as a low-pass filter thereby completing the demodulation circuit. Note that when the post synaptic membrane is near resting state (membrane conductance low) that the gap junction will also provide greatest coupling between the pre- and post-synaptic membranes(Curti and O'Brien 2016). Any high frequency amplitude-modulated field which couples to a presynaptic transmembrane potential, according to previously mentioned conditions, may then be demodulated by the rectifying gap junction and low pass-filtering post synaptic neuron. In the case of the present work this demodulation would produce actual neuronal frequencies at the applied beat frequency. Those beat frequencies below the cutoff frequency of the post synaptic resting membrane would be favored. Since the pyramidal cutoff frequency is approximately 20 Hz for pyramidal neurons this may explain the predominance of the 20 Hz beat frequency over the 140 Hz beat frequency of this work and may suggest future experimental design. It should be noted that ubiquitous pyramidal cells of the neocortex, including the sensorimotor cortex, as well as glial cells are known to contain gap junctions.

References

Nyberg-Hansen, R., & Rinvik, E. (1963). Some comments on the pyramidal tract, with special reference to its individual variations in man. Acta Neurologica Scandinavica, 39(1), 1-30.

Bourbonnais, D., & Noven, S. V. (1989). Weakness in patients with hemiparesis. American Journal of Occupational Therapy, 43(5), 313-319.

Babiloni, C., Carducci, F., Cincotti, F., Rossini, P. M., Neuper, C., Pfurtscheller, G., & Babiloni, F. (1999). Human movement-related potentials vs desynchronization of EEG alpha rhythm: a high-resolution EEG study. Neuroimage, 10(6), 658-665.

Ghacibeh, G. A., Mirpuri, R., Drago, V., Jeong, Y., Heilman, K. M., & Triggs, W. J. (2007). Ipsilateral motor activation during unimanual and bimanual motor tasks. Clinical Neurophysiology, 118(2), 325-332.

Ganguly, K., Secundo, L., Ranade, G., Orsborn, A., Chang, E. F., Dimitrov, D. F., ... & Carmena, J. M. (2009). Cortical representation of ipsilateral arm movements in monkey and man. Journal of Neuroscience, 29(41), 12948-12956.

Ames, K. C., & Churchland, M. M. (2019). Motor cortex signals for each arm are mixed across hemispheres and neurons yet partitioned within the population response. Elife, 8, e46159.

Bundy, D. T., Szrama, N., Pahwa, M., & Leuthardt, E. C. (2018). Unilateral, 3D arm movement kinematics are encoded in ipsilateral human cortex. Journal of Neuroscience, 38(47), 10042-10056.

Wisneski, K. J., Anderson, N., Schalk, G., Smyth, M., Moran, D., & Leuthardt, E. C. (2008). Unique cortical physiology associated with ipsilateral hand movements and neuroprosthetic implications. Stroke, 39(12), 3351-3359.

Cisek, P., Crammond, D. J., & Kalaska, J. F. (2003). Neural activity in primary motor and dorsal premotor cortex in reaching tasks with the contralateral versus ipsilateral arm. Journal of Neurophysiology, 89(2), 922-942.

Steinberg, O., Donchin, O., Gribova, A., De Oliveira, S. C., Bergman, H., & Vaadia, E. (2002). Neuronal populations in primary motor cortex encode bimanual arm movements. European Journal of Neuroscience, 15(8), 1371-1380.

Willett, F. R., Deo, D. R., Avansino, D. T., Rezaii, P., Hochberg, L. R., Henderson, J. M., & Shenoy, K. V. (2020). Hand knob area of premotor cortex represents the whole body in a compositional way. Cell, 181(2), 396-409.

Heming, E. A., Cross, K. P., Takei, T., Cook, D. J., & Scott, S. H. (2019). Independent representations of ipsilateral and contralateral limbs in primary motor cortex. ELife, 8, e48190.

Downey, J. E., Quick, K. M., Schwed, N., Weiss, J. M., Wittenberg, G. F., Boninger, M. L., & Collinger, J. L. (2020). The motor cortex has independent representations for ipsilateral and contralateral arm movements but correlated representations for grasping. Cerebral Cortex, 30(10), 5400-5409.

Corballis, M. C., Badzakova-Trajkov, G., & Häberling, I. S. (2012). Right hand, left brain: genetic and evolutionary bases of cerebral asymmetries for language and manual action. Wiley Interdisciplinary Reviews: Cognitive Science, 3(1), 1-17.

Rothi, L. G., Ochipa, C., & Heilman, K. M. (1997). A cognitive neuropsychological model of limb praxis and apraxia. Apraxia: The neuropsychology of action, 29-49.

Schaefer, S. Y., Haaland, K. Y., & Sainburg, R. L. (2007). Ipsilesional motor deficits following stroke reflect hemispheric specializations for movement control. Brain, 130(8), 2146-2158.

Liepmann, H. (1908). Drei aufsätze aus dem apraxiegebiet (Vol. 2545). S. Karger.

De Renzi, E., & Lucchelli, F. (1988). Ideational apraxia. Brain, 111(5), 1173-1185.

Haaland, K. Y., Harrington, D. L., & Knight, R. T. (2000). Neural representations of skilled movement. Brain, 123(11), 2306-2313.

Chettouf, S., Rueda-Delgado, L. M., de Vries, R., Ritter, P., & Daffertshofer, A. (2020). Are unimanual movements bilateral? Neuroscience & Biobehavioral Reviews, 113, 39-50.

Verstynen, T., Diedrichsen, J., Albert, N., Aparicio, P., & Ivry, R. B. (2005). Ipsilateral motor cortex activity during unimanual hand movements relates to task complexity. Journal of Neurophysiology, 93(3), 1209-1222.

Verstynen, T., & Ivry, R. B. (2011). Network dynamics mediating ipsilateral motor cortex activity during unimanual actions. Journal of Cognitive Neuroscience, 23(9), 2468-2480.

Schäfer, K., Blankenburg, F., Kupers, R., Grüner, J. M., Law, I., Lauritzen, M., & Larsson, H. B. (2012). Negative BOLD signal changes in ipsilateral primary somatosensory cortex are associated with perfusion decreases and behavioral evidence for functional inhibition. Neuroimage, 59(4), 3119-3127.

Leszczyński, M., Barczak, A., Kajikawa, Y., Ulbert, I., Falchier, A. Y., Tal, I., ... & Schroeder, C. E. (2020). Dissociation of broadband high-frequency activity and neuronal firing in the neocortex. Science Advances, 6(33), eabb0977.

Muthukumaraswamy, S. D. (2010). Functional properties of human primary motor cortex gamma oscillations. Journal of Neurophysiology, 104(5), 2873-2885.

Kriegeskorte, N., & Douglas, P. K. (2019). Interpreting encoding and decoding models. Current Opinion in Neurobiology, 55, 167-179.

Weichert, F., Bachmann, D., Rudak, B., & Fisseler, D. (2013). Analysis of the accuracy and robustness of the leap motion controller. Sensors, 13(5), 6380-6393.

Suway, S. B., & Schwartz, A. B. (2019). Activity in Primary Motor Cortex Related to Visual Feedback. Cell Reports, 29(12), 3872-3884.

Stolk, A., Griffin, S., Van der Meij, R., Dewar, C., Saez, I., Lin, J. J., ... & Oostenveld, R. (2018). Integrated analysis of anatomical and electrophysiological human intracranial data. Nature Protocols, 13(7), 1699-1723.

Canolty, R. T., Edwards, E., Dalal, S. S., Soltani, M., Nagarajan, S. S., Kirsch, H. E., ... & Knight, R. T. (2006). High gamma power is phase-locked to theta oscillations in human neocortex. Science, 313(5793), 1626-1628.

Pei, X., Leuthardt, E. C., Gaona, C. M., Brunner, P., Wolpaw, J. R., & Schalk, G. (2011). Spatiotemporal dynamics of electrocorticographic high gamma activity during overt and covert word repetition. Neuroimage, 54(4), 2960-2972

Hoerl, A. E., & Kennard, R. W. (1970). Ridge regression: Biased estimation for nonorthogonal problems. Technometrics, 12(1), 55-67.

Anderson, M., & Braak, C. T. (2003). Permutation tests for multi-factorial analysis of variance. Journal of statistical computation and simulation, 73(2), 85-113.

Churchland, M. M., Cunningham, J. P., Kaufman, M. T., Foster, J. D., Nuyujukian, P., Ryu, S. I., & Shenoy, K. V. (2012). Neural population dynamics during reaching. Nature, 487(7405), 51-56.

Elsayed, G. F., Lara, A. H., Kaufman, M. T., Churchland, M. M., & Cunningham, J. P. (2016). Reorganization between preparatory and movement population responses in motor cortex. Nature Communications, 7(1), 1-15.

Schaffer, J. E., & Sainburg, R. L. (2021). Interlimb Responses to Perturbations of Bilateral Movements are Asymmetric. Journal of Motor Behavior, 53(2), 217-233.

Diedrichsen, J., Wiestler, T., & Krakauer, J. W. (2013). Two distinct ipsilateral cortical representations for individuated finger movements. Cerebral Cortex, 23(6), 1362-1377.

Przybylski, Ł., & Króliczak, G. (2017). Planning functional grasps of simple tools invokes the hand-independent praxis representation network: an fMRI study. Journal of the International Neuropsychological Society, 23(2), 108-120.

Buxbaum, L. J., Kyle, K. M., Tang, K., & Detre, J. A. (2006). Neural substrates of knowledge of hand postures for object grasping and functional object use: Evidence from fMRI. Brain Research, 1117(1), 175-185.

Xu J, Gannon PJ, Emmorey K, Smith JF, Braun A. Symbolic gestures and spoken language are processed by a common neural system. Proc Natl Acad Sci U S A 2009, 106:20665–20669.

Bohlhalter, S., Hattori, N., Wheaton, L., Fridman, E., Shamim, E. A., Garraux, G., & Hallett, M. (2009). Gesture subtype–dependent left lateralization of praxis planning: An event-related fMRI study. Cerebral Cortex, 19(6), 1256-1262.

Ochipa C, Rothi LJG, Heilman KM (1989): Ideational apraxia—A deficit in tool selection and use. Ann Neurol 25:190–193.

Vingerhoets, G., Acke, F., Alderweireldt, A. S., Nys, J., Vandemaele, P., & Achten, E. (2012). Cerebral lateralization of praxis in right-and left-handedness: Same pattern, different strength. Human Brain Mapping, 33(4), 763-777.

Vingerhoets, G., Alderweireldt, A. S., Vandemaele, P., Cai, Q., Van der Haegen, L., Brysbaert, M., & Achten, E. (2013). Praxis and language are linked: evidence from co-lateralization in individuals with atypical language dominance. Cortex, 49(1), 172-183.

Vingerhoets, G., Acke, F., Alderweireldt, A. S., Nys, J., Vandemaele, P., & Achten, E. (2012). Cerebral lateralization of praxis in right-and left-handedness: Same pattern, different strength. Human Brain Mapping, 33(4), 763-777.

Jäncke, L., Peters, M., Himmelbach, M., Nösselt, T., Shah, J., & Steinmetz, H. (2000). fMRI study of bimanual coordination. Neuropsychologia, 38(2), 164-174.

Toyokura, M., Muro, I., Komiya, T., & Obara, M. (1999). Relation of bimanual coordination to activation in the sensorimotor cortex and supplementary motor area: analysis using functional magnetic resonance imaging. Brain Research Bulletin, 48(2), 211-217.

Serrien, D. J., Cassidy, M. J., & Brown, P. (2003). The importance of the dominant hemisphere in the organization of bimanual movements. Human Brain Mapping, 18(4), 296-305.

Maki, Y., Wong, K. F. K., Sugiura, M., Ozaki, T., & Sadato, N. (2008). Asymmetric control mechanisms of bimanual coordination: an application of directed connectivity analysis to kinematic and functional MRI data. Neuroimage, 42(4), 1295-1304.

DeLong, M. R. (1979). Motor functions of the basal ganglia as revealed by studies of single cell activity in the behaving primates. Advances in neurology, 24, 131-140.

Alexander, G. E., DeLong, M. R., & Strick, P. L. (1986). Parallel organization of functionally segregated circuits linking basal ganglia and cortex. Annual review of neuroscience, 9(1), 357-381.

Alexander, G. E., & Crutcher, M. D. (1990). Functional architecture of basal ganglia circuits: neural substrates of parallel processing. Trends in neurosciences, 13(7), 266-271.

Parent, A., & Hazrati, L. N. (1995). Functional anatomy of the basal ganglia. I. The cortico-basal ganglia-thalamo-cortical loop. Brain research reviews, 20(1), 91-127.

Middleton, F. A., & Strick, P. L. (2000). Basal ganglia and cerebellar loops: motor and cognitive circuits. Brain research reviews, 31(2-3), 236-250.

Dauer, W., & Przedborski, S. (2003). Parkinson's disease: mechanisms and models. Neuron, 39(6), 889-909.

Kumar, R., Lozano, A. M., Kim, Y. J., Hutchison, W. D., Sime, E., Halket, E., & Lang, A. E. (1998). Double-blind evaluation of subthalamic nucleus deep brain stimulation in advanced Parkinson's disease. Neurology, 51(3), 850-855.

Kühn, A. A., Trottenberg, T., Kivi, A., Kupsch, A., Schneider, G. H., & Brown, P. (2005). The relationship between local field potential and neuronal discharge in the subthalamic nucleus of patients with Parkinson's disease. Experimental neurology, 194(1), 212-220.

Little, S., & Brown, P. (2014). The functional role of beta oscillations in Parkinson's disease. Parkinsonism & related disorders, 20, S44-S48.

Weinberger, M., Mahant, N., Hutchison, W. D., Lozano, A. M., Moro, E., Hodaie, M., ... & Dostrovsky, J. O. (2006). Beta oscillatory activity in the subthalamic nucleus and its relation to dopaminergic response in Parkinson's disease. Journal of neurophysiology, 96(6), 3248-3256.

Mallet, N., Pogosyan, A., Sharott, A., Csicsvari, J., Bolam, J. P., Brown, P., & Magill, P. J. (2008). Disrupted dopamine transmission and the emergence of exaggerated beta oscillations in subthalamic nucleus and cerebral cortex. Journal of Neuroscience, 28(18), 4795-4806.

De Hemptinne, C., Swann, N. C., Ostrem, J. L., Ryapolova-Webb, E. S., San Luciano, M., Galifianakis, N. B., & Starr, P. A. (2015). Therapeutic deep brain stimulation reduces cortical phase-amplitude coupling in Parkinson's disease. Nature neuroscience, 18(5), 779-786.

Mink, J. W. (1996). The basal ganglia: focused selection and inhibition of competing motor programs. Progress in neurobiology, 50(4), 381-425.

Yttri, E. A., & Dudman, J. T. (2016). Opponent and bidirectional control of movement velocity in the basal ganglia. Nature, 533(7603), 402-406.

Abosch A, Hutchison WD, Saint-Cyr JA, Dostrovsky JO, Lozano AM: Movement-related neurons of the subthalamic nucleus in patients with Parkinson disease. J Neurosurg 97:1167–1172, 2002.

Rodriguez-Oroz MC, Rodriguez M, Guridi J, Mewes K, Chockkman V, Vitek J, DeLong MR, Obeso JA: The subthalamic nucleus in Parkinson's disease: Somatotopic organization and physiological characteristics. Brain 124:1777– 1790, 2001.

Patil, P. G., Carmena, J. M., Nicolelis, M. A., & Turner, D. A. (2004). Ensemble recordings of human subcortical neurons as a source of motor control signals for a brain-machine interface. Neurosurgery, 55(1), 27-38.

Tan, H., Pogosyan, A., Ashkan, K., Green, A. L., Aziz, T., Foltynie, T., ... & Brown, P. (2016). Decoding gripping force based on local field potentials recorded from subthalamic nucleus in humans. Elife, 5, e19089.

Alegre, M., Alonso-Frech, F., Rodríguez-Oroz, M. C., Guridi, J., Zamarbide, I., Valencia, M., ... & Artieda, J. (2005). Movement-related changes in oscillatory activity in the human subthalamic nucleus: ipsilateral vs. contralateral movements. European Journal of Neuroscience, 22(9), 2315-2324.

Darvas, F., & Hebb, A. O. (2014). Task specific inter-hemispheric coupling in human subthalamic nuclei. Frontiers in human neuroscience, 8, 701.

Walker, H. C., Watts, R. L., Guthrie, S., Wang, D., & Guthrie, B. L. (2009). Bilateral effects of unilateral subthalamic deep brain stimulation on Parkinson's disease at 1 year. Neurosurgery, 65(2), 302-310.

Schalk, G., Kubanek, J., Miller, K. J., Anderson, N. R., Leuthardt, E. C., Ojemann, J. G., ... & Wolpaw, J. R. (2007). Decoding two-dimensional movement trajectories using electrocorticographic signals in humans. Journal of neural engineering, 4(3), 264.

Flint, R. D., Wright, Z. A., Scheid, M. R., & Slutzky, M. W. (2013). Long term, stable brain machine interface performance using local field potentials and multiunit spikes. Journal of neural engineering, 10(5), 056005.

De Hemptinne, C., Ryapolova-Webb, E. S., Air, E. L., Garcia, P. A., Miller, K. J., Ojemann, J. G., ... & Starr, P. A. (2013). Exaggerated phase–amplitude coupling in the primary motor cortex in Parkinson disease. Proceedings of the National Academy of Sciences, 110(12), 4780-4785.

Crowell, A. L., Ryapolova-Webb, E. S., Ostrem, J. L., Galifianakis, N. B., Shimamoto, S., Lim, D. A., & Starr, P. A. (2012). Oscillations in sensorimotor cortex in movement disorders: an electrocorticography study. Brain, 135(2), 615-630.

Flint, R. D., Ethier, C., Oby, E. R., Miller, L. E., & Slutzky, M. W. (2012). Local field potentials allow accurate decoding of muscle activity. Journal of neurophysiology, 108(1), 18-24.

Hoerl, A. E., & Kennard, R. W. (1970). Ridge regression: Biased estimation for nonorthogonal problems. Technometrics, 12(1), 55-67.

Lozano, A. M. et al. Deep brain stimulation: current challenges and future directions. Nat. Rev. Neurol. 15, 148–160 (2019).

Gilron, R., Little, S., Perrone, R., Wilt, R., de Hemptinne, C., Yaroshinsky, M. S., Racine, C. A., ... & Starr, P. A. (2021). Long-term wireless streaming of neural recordings for circuit discovery and adaptive stimulation in individuals with Parkinson's disease. Nature biotechnology, 1-8.

Starr, P. A. Totally implantable bidirectional neural prostheses: a flexible platform for innovation in neuromodulation. Front. Neurosci. 12, 619 (2018).

Bestmann, S., Ward, N., 2017. Are current flow models for transcranial electrical stimulation fit for purpose? Brain Stimulat. https://doi.org/10.1016/j.brs.2017.04.002

Bhadra, Narendra, Foldes, E., Vrabec, T., Kilgore, K., Bhadra, Niloy, 2018. Temporary persistence of conduction block after prolonged kilohertz frequency alternating current on rat sciatic nerve. J. Neural Eng. 15, 016012. https://doi.org/10.1088/1741-2552/aa89a4

Biabani, M., Aminitehrani, M., Zoghi, M., Farrell, M., Egan, G., Jaberzadeh, S., 2018a. The effects of transcranial direct current stimulation on short-interval intracortical inhibition and intracortical facilitation: a systematic review and meta-analysis. Rev. Neurosci. 29, 99–114. https://doi.org/10.1515/revneuro-2017-0023

Biabani, M., Farrell, M., Zoghi, M., Egan, G., Jaberzadeh, S., 2018b. The minimal number of TMS trials required for the reliable assessment of corticospinal excitability, short interval intracortical inhibition, and intracortical facilitation. Neurosci. Lett. 674, 94–100. https://doi.org/10.1016/j.neulet.2018.03.026

Bortoletto, M., Pellicciari, M.C., Rodella, C., Miniussi, C., 2015. The interaction with task-induced activity is more important than polarization: a tDCS study. Brain Stimulat. 8, 269–276. https://doi.org/10.1016/j.brs.2014.11.006

Cabral, M.E., Baltar, A., Borba, R., Galvão, S., Santos, L., Fregni, F., Monte-Silva, K., 2015. Transcranial direct current stimulation: before, during, or after motor training? Neuroreport 26, 618–622. https://doi.org/10.1097/WNR.0000000000000397

Campana, M., Papazova, I., Pross, B., Hasan, A., Strube, W., 2019. Motor-cortex excitability and response variability following paired-associative stimulation: a proof-of-concept study comparing individualized and fixed inter-stimulus intervals. Exp. Brain Res. 237, 1727–1734. https://doi.org/10.1007/s00221-019-05542-x

Cantarero, G., Spampinato, D., Reis, J., Ajagbe, L., Thompson, T., Kulkarni, K., Celnik, P., 2015. Cerebellar direct current stimulation enhances on-line motor skill acquisition through an effect on accuracy. J. Neurosci. Off. J. Soc. Neurosci. 35, 3285–3290. https://doi.org/10.1523/JNEUROSCI.2885-14.2015

Carroll, T.J., Riek, S., Carson, R.G., 2001. Reliability of the input-output properties of the cortico-spinal pathway obtained from transcranial magnetic and electrical stimulation. J. Neurosci. Methods 112, 193–202.

Cavaleri, R., Schabrun, S.M., Chipchase, L.S., 2017. The number of stimuli required to reliably assess corticomotor excitability and primary motor cortical representations using transcranial magnetic stimulation (TMS): a systematic review and meta-analysis. Syst. Rev. 6, 48. https://doi.org/10.1186/s13643-017-0440-8

Chaieb, L., Antal, A., Paulus, W., 2011. Transcranial alternating current stimulation in the low kHz range increases motor cortex excitability. Restor. Neurol. Neurosci. 29, 167–175. https://doi.org/10.3233/RNN-2011-0589

Chaieb, L., Antal, A., Pisoni, A., Saiote, C., Opitz, A., Ambrus, G.G., Focke, N., Paulus, W., 2014. Safety of 5 kHz tACS. Brain Stimulat. 7, 92–96. https://doi.org/10.1016/j.brs.2013.08.004

Chung, S.W., Hill, A.T., Rogasch, N.C., Hoy, K.E., Fitzgerald, P.B., 2016. Use of theta-burst stimulation in changing excitability of motor cortex: A systematic review and meta-analysis. Neurosci. Biobehav. Rev. 63, 43–64. https://doi.org/10.1016/j.neubiorev.2016.01.008

Conson, M., Errico, D., Mazzarella, E., Giordano, M., Grossi, D., Trojano, L., 2015. Transcranial Electrical Stimulation over Dorsolateral Prefrontal Cortex Modulates Processing of Social Cognitive and Affective Information. PloS One 10, e0126448. https://doi.org/10.1371/journal.pone.0126448

Darling, W.G., Wolf, S.L., Butler, A.J., 2006. Variability of motor potentials evoked by transcranial magnetic stimulation depends on muscle activation. Exp. Brain Res. Exp. Hirnforsch. Exp. Cerebrale 174, 376–385. https://doi.org/10.1007/s00221-006-0468-9

Dissanayaka, T., Zoghi, M., Farrell, M., Egan, G.F., Jaberzadeh, S., 2017. Does transcranial electrical stimulation enhance corticospinal excitability of the motor cortex in healthy individuals? A systematic review and meta-analysis. Eur. J. Neurosci. 46, 1968–1990. https://doi.org/10.1111/ejn.13640

Feurra, M., Bianco, G., Santarnecchi, E., Del Testa, M., Rossi, A., Rossi, S., 2011. Frequency-dependent tuning of the human motor system induced by transcranial oscillatory potentials. J. Neurosci. Off. J. Soc. Neurosci. 31, 12165–12170. https://doi.org/10.1523/JNEUROSCI.0978-11.2011

Feurra, M., Pasqualetti, P., Bianco, G., Santarnecchi, E., Rossi, A., Rossi, S., 2013. State-Dependent Effects of Transcranial Oscillatory Currents on the Motor System: What You Think Matters. J. Neurosci. 33, 17483–17489. https://doi.org/10.1523/JNEUROSCI.1414-13.2013

Fitzgerald, P.B., 2020. An update on the clinical use of repetitive transcranial magnetic stimulation in the treatment of depression. J. Affect. Disord. 276, 90–103. https://doi.org/10.1016/j.jad.2020.06.067

Flöel, A., Rösser, N., Michka, O., Knecht, S., Breitenstein, C., 2008. Noninvasive brain stimulation improves language learning. J. Cogn. Neurosci. 20, 1415–1422. https://doi.org/10.1162/jocn.2008.20098

Galea, J.M., Vazquez, A., Pasricha, N., de Xivry, J.-J.O., Celnik, P., 2011. Dissociating the roles of the cerebellum and motor cortex during adaptive learning: the motor cortex retains what the cerebellum learns. Cereb. Cortex N. Y. N 1991 21, 1761–1770. https://doi.org/10.1093/cercor/bhq246

Giglia, G., Brighina, F., Rizzo, S., Puma, A., Indovino, S., Maccora, S., Baschi, R., Cosentino, G., Fierro, B., 2014. Anodal transcranial direct current stimulation of the right dorsolateral prefrontal cortex enhances memory-guided responses in a visuospatial working memory task. Funct. Neurol. 29, 189–193.

Goldsworthy, M.R., Hordacre, B., Ridding, M.C., 2016. Minimum number of trials required for within- and between-session reliability of TMS measures of corticospinal excitability. Neuroscience 320, 205–209. https://doi.org/10.1016/j.neuroscience.2016.02.012

Grossman, N., Bono, D., Dedic, N., Kodandaramaiah, S.B., Rudenko, A., Suk, H.-J., Cassara, A.M., Neufeld, E., Kuster, N., Tsai, L.-H., Pascual-Leone, A., Boyden, E.S., 2017. Noninvasive Deep Brain Stimulation via Temporally Interfering Electric Fields. Cell 169, 1029-1041.e16. https://doi.org/10.1016/j.cell.2017.05.024

Hashemirad, F., Zoghi, M., Fitzgerald, P.B., Jaberzadeh, S., 2017. Reliability of Motor Evoked Potentials Induced by Transcranial Magnetic Stimulation: The Effects of Initial Motor Evoked Potentials Removal. Basic Clin. Neurosci. 8, 43–50. https://doi.org/10.15412/J.BCN.03080106

Heimrath, K., Breitling, C., Krauel, K., Heinze, H.-J., Zaehle, T., 2015. Modulation of pre-attentive spectro-temporal feature processing in the human auditory system by HD-tDCS. Eur. J. Neurosci. 41, 1580–1586. https://doi.org/10.1111/ejn.12908

Heise, K.-F., Kortzorg, N., Saturnino, G.B., Fujiyama, H., Cuypers, K., Thielscher, A., Swinnen, S.P., 2016. Evaluation of a Modified High-Definition Electrode Montage for Transcranial Alternating Current Stimulation (tACS) of Pre-Central Areas. Brain Stimulat. 9, 700–704. https://doi.org/10.1016/j.brs.2016.04.009

Horvath, J.C., Forte, J.D., Carter, O., 2015. Evidence that transcranial direct current stimulation (tDCS) generates little-to-no reliable neurophysiologic effect beyond MEP amplitude modulation in healthy human subjects: A systematic review. Neuropsychologia 66, 213–236. https://doi.org/10.1016/j.neuropsychologia.2014.11.021

Huang, Y., Liu, A.A., Lafon, B., Friedman, D., Dayan, M., Wang, X., Bikson, M., Doyle, W.K., Devinsky, O., Parra, L.C., 2018. Correction: Measurements and models of electric fields in thein vivohuman brain during transcranial electric stimulation. eLife 7. https://doi.org/10.7554/eLife.35178

Huang, Y.-Z., Edwards, M.J., Rounis, E., Bhatia, K.P., Rothwell, J.C., 2005. Theta burst stimulation of the human motor cortex. Neuron 45, 201–206. https://doi.org/10.1016/j.neuron.2004.12.033

Huang, Y.-Z., Lu, M.-K., Antal, A., Classen, J., Nitsche, M., Ziemann, U., Ridding, M., Hamada, M., Ugawa, Y., Jaberzadeh, S., Suppa, A., Paulus, W., Rothwell, J., 2017. Plasticity induced by non-invasive transcranial brain stimulation: A position paper. Clin. Neurophysiol. Off. J. Int. Fed. Clin. Neurophysiol. 128, 2318–2329. https://doi.org/10.1016/j.clinph.2017.09.007

Huang, Y.-Z., Rothwell, J.C., Edwards, M.J., Chen, R.-S., 2008. Effect of physiological activity on an NMDA-dependent form of cortical plasticity in human. Cereb. Cortex N. Y. N 1991 18, 563–570. https://doi.org/10.1093/cercor/bhm087

Iglesias, A.H., 2020. Transcranial Magnetic Stimulation as Treatment in Multiple Neurologic Conditions. Curr. Neurol. Neurosci. Rep. 20, 1. https://doi.org/10.1007/s11910-020-1021-0

Inukai, Y., Saito, K., Sasaki, R., Tsuiki, S., Miyaguchi, S., Kojima, S., Masaki, M., Otsuru, N., Onishi, H., 2016. Comparison of Three Non-Invasive Transcranial Electrical Stimulation Methods for Increasing Cortical Excitability. Front. Hum. Neurosci. 10, 668. https://doi.org/10.3389/fnhum.2016.00668

Javadi, A.-H., Glen, J.C., Halkiopoulos, S., Schulz, M., Spiers, H.J., 2017. Oscillatory Reinstatement Enhances Declarative Memory. J. Neurosci. Off. J. Soc. Neurosci. 37, 9939–9944. https://doi.org/10.1523/JNEUROSCI.0265-17.2017

Kamen, G., 2004. Reliability of motor-evoked potentials during resting and active contraction conditions. Med. Sci. Sports Exerc. 36, 1574–1579.

Lefaucheur, J.-P., Aleman, A., Baeken, C., Benninger, D.H., Brunelin, J., Di Lazzaro, V., Filipović, S.R., Grefkes, C., Hasan, A., Hummel, F.C., Jääskeläinen, S.K., Langguth, B., Leocani, L., Londero, A., Nardone, R., Nguyen, J.-P., Nyffeler, T., Oliveira-Maia, A.J., Oliviero, A., Padberg, F., Palm, U., Paulus, W., Poulet, E., Quartarone, A., Rachid, F., Rektorová, I., Rossi, S., Sahlsten, H., Schecklmann, M., Szekely, D., Ziemann, U., 2020. Evidence-based guidelines on the therapeutic use of repetitive transcranial magnetic stimulation (rTMS): An update (2014-2018). Clin.

Neurophysiol. Off. J. Int. Fed. Clin. Neurophysiol. 131, 474–528. https://doi.org/10.1016/j.clinph.2019.11.002

Malcolm, M.P., Triggs, W.J., Light, K.E., Shechtman, O., Khandekar, G., Gonzalez Rothi, L.J., 2006. Reliability of motor cortex transcranial magnetic stimulation in four muscle representations. Clin. Neurophysiol. Off. J. Int. Fed. Clin. Neurophysiol. 117, 1037–1046. https://doi.org/10.1016/j.clinph.2006.02.005

Meinzer, M., Lindenberg, R., Sieg, M.M., Nachtigall, L., Ulm, L., Flöel, A., 2014. Transcranial direct current stimulation of the primary motor cortex improves word-retrieval in older adults. Front. Aging Neurosci. 6, 253. https://doi.org/10.3389/fnagi.2014.00253

Meteyard, L., Holmes, N.P., 2018. TMS SMART - Scalp mapping of annoyance ratings and twitches caused by Transcranial Magnetic Stimulation. J. Neurosci. Methods 299, 34–44. https://doi.org/10.1016/j.jneumeth.2018.02.008

Najib, U., Horvath, J.C., Silvanto, J., Pascual-Leone, A., 2010. State-dependency effects on TMS: a look at motive phosphene behavior. J. Vis. Exp. JoVE. https://doi.org/10.3791/2273

Neudorfer, C., Chow, C., Boutet, A., Loh, A., Germann, J., Elias, G.J., Hutchison, W.D., Lozano, A.M., 2021. Kilohertz-frequency stimulation of the nervous system: a review of underlying mechanisms. Brain Stimul. Basic Transl. Clin. Res. Neuromodulation 0. https://doi.org/10.1016/j.brs.2021.03.008

Nevler, N., Ash, E.L., 2015. TMS as a Tool for Examining Cognitive Processing. Curr. Neurol. Neurosci. Rep. 15, 52. https://doi.org/10.1007/s11910-015-0575-8

Nitsche, M.A., Fricke, K., Henschke, U., Schlitterlau, A., Liebetanz, D., Lang, N., Henning, S., Tergau, F., Paulus, W., 2003. Pharmacological modulation of cortical excitability shifts induced by transcranial direct current stimulation in humans. J. Physiol. 553, 293–301. https://doi.org/10.1113/jphysiol.2003.049916

Nitsche, M.A., Paulus, W., 2001. Sustained excitability elevations induced by transcranial DC motor cortex stimulation in humans. Neurology 57, 1899–1901. https://doi.org/10.1212/WNL.57.10.1899

Nitsche, M.A., Paulus, W., 2000. Excitability changes induced in the human motor cortex by weak transcranial direct current stimulation. J. Physiol. 527 Pt 3, 633–639.
Opitz, A., Paulus, W., Will, S., Antunes, A., Thielscher, A., 2015. Determinants of the electric field during transcranial direct current stimulation. NeuroImage 109, 140–150. https://doi.org/10.1016/j.neuroimage.2015.01.033

Ovadia-Caro, S., Khalil, A.A., Sehm, B., Villringer, A., Nikulin, V.V., Nazarova, M., 2019. Predicting the Response to Non-invasive Brain Stimulation in Stroke. Front. Neurol. 10. https://doi.org/10.3389/fneur.2019.00302

Peterchev, A.V., Wagner, T.A., Miranda, P.C., Nitsche, M.A., Paulus, W., Lisanby, S.H., Pascual-Leone, A., Bikson, M., 2012. Fundamentals of transcranial electric and magnetic stimulation dose: definition, selection, and reporting practices. Brain Stimulat. 5, 435–453. https://doi.org/10.1016/j.brs.2011.10.001

Reis, J., Schambra, H.M., Cohen, L.G., Buch, E.R., Fritsch, B., Zarahn, E., Celnik, P.A., Krakauer, J.W., 2009. Noninvasive cortical stimulation enhances motor skill acquisition over multiple days through an effect on consolidation. Proc. Natl. Acad. Sci. 106, 1590–1595. https://doi.org/10.1073/pnas.0805413106

Richmond, L.L., Wolk, D., Chein, J., Olson, I.R., 2014. Transcranial direct current stimulation enhances verbal working memory training performance over time and near transfer outcomes. J. Cogn. Neurosci. 26, 2443–2454. https://doi.org/10.1162/jocn_a_00657
Ridding, M.C., Ziemann, U., 2010. Determinants of the induction of cortical plasticity by non-invasive brain stimulation in healthy subjects. J. Physiol. 588, 2291–2304. https://doi.org/10.1113/jphysiol.2010.190314

Rohan, M.L., Yamamoto, R.T., Ravichandran, C.T., Cayetano, K.R., Morales, O.G., Olson, D.P., Vitaliano, G., Paul, S.M., Cohen, B.M., 2014. Rapid mood-elevating effects of low field magnetic stimulation in depression. Biol. Psychiatry 76, 186–193. https://doi.org/10.1016/j.biopsych.2013.10.024
Roy, L.B., Sparing, R., Fink, G.R., Hesse, M.D., 2015. Modulation of attention functions by anodal tDCS on right PPC. Neuropsychologia 74, 96–107. https://doi.org/10.1016/j.neuropsychologia.2015.02.028

Rufener, K.S., Oechslin, M.S., Zaehle, T., Meyer, M., 2016. Transcranial Alternating Current Stimulation (tACS) differentially modulates speech perception in young and older adults. Brain Stimulat. 9, 560–565. https://doi.org/10.1016/j.brs.2016.04.002

Sheltraw, D., Inglis, B., in preparation. Considering the Ramifications of the Repetitive Transcranial Magnetic Stimulation Spectra.

Sheltraw, D., Inglis, B., Labruna, L., Ivry, R., 2021. Comparing the electric fields of Transcranial electric and magnetic perturbation. J. Neural Eng. https://doi.org/10.1088/1741-2552/abebee

Stagg, C.J., Bestmann, S., Constantinescu, A.O., Moreno, L.M., Allman, C., Mekle, R., Woolrich, M., Near, J., Johansen-Berg, H., Rothwell, J.C., 2011. Relationship between physiological measures of excitability and levels of glutamate and GABA in the human motor cortex. J. Physiol. 589, 5845–5855. https://doi.org/10.1113/jphysiol.2011.216978

Truong, D.Q., Magerowski, G., Pascual-Leone, A., Alonso-Alonso, M., Bikson, M., 2012. Finite Element study of skin and fat delineation in an obese subject for transcranial Direct Current Stimulation. Conf. Proc. Annu. Int. Conf. IEEE Eng. Med. Biol. Soc. IEEE Eng. Med. Biol. Soc. Annu. Conf. 2012, 6587–6590. https://doi.org/10.1109/EMBC.2012.6347504

Volkow, N.D., Tomasi, D., Wang, G.-J., Fowler, J.S., Telang, F., Wang, R., Alexoff, D., Logan, J., Wong, C., Pradhan, K., Caparelli, E.C., Ma, Y., Jayne, M., 2010. Effects of low-field magnetic stimulation on brain glucose metabolism. NeuroImage 51, 623–628. https://doi.org/10.1016/j.neuroimage.2010.02.015

Vöröslakos, M., Takeuchi, Y., Brinyiczki, K., Zombori, T., Oliva, A., Fernández-Ruiz, A., Kozák, G., Kincses, Z.T., Iványi, B., Buzsáki, G., Berényi, A., 2018. Direct effects of transcranial electric stimulation on brain circuits in rats and humans. Nat. Commun. 9, 483. https://doi.org/10.1038/s41467-018-02928-3

Wang, B., Shen, M.R., Deng, Z.-D., Smith, J.E., Tharayil, J.J., Gurrey, C.J., Gomez, L.J., Peterchev, A.V., 2018. Redesigning existing transcranial magnetic stimulation coils to reduce energy: application to low field magnetic stimulation. J. Neural Eng. https://doi.org/10.1088/1741-2552/aaa505

Wöstmann, M., Vosskuhl, J., Obleser, J., Herrmann, C.S., 2018. Opposite effects of lateralised transcranial alpha versus gamma stimulation on auditory spatial attention. Brain Stimulat. https://doi.org/10.1016/j.brs.2018.04.006